AD-A055 884 PHOTOMETRICS INC LEXINGTON MASS F/G 4/1

ASSESSMENT AND EVALUATION OF SIMULATION DATA.(U)

NOV 77 I L KOFSKY, D P VILLANUCCI, G DAVIDSON DNA001-77-C-0208

UNCLASSIFIED PHM-01-78 DNA-4303F NL

1 OF 2
ADA
055884

AD-E300 220

FOR FURTHER TRAN

DNA 4303F

SBIE

AD-E300 220

AD A055884

ASSESSMENT AND EVALUATION OF SIMULATION DATA.

HAES REPORT No. 69

PhotoMetrics, Inc.
442 Marrett Road
Lexington, Massachusetts 02173

PHM-01-78, DNA-HAES-69

DDC FILE COPY

15 Nov[redacted]77

135 p.

Final Report, [redacted] 1 Marc[redacted]—15 Oct[redacted]77,

CONTRACT No. DNA 001-77-C-0208

I. L. Kofsky,
D. P. Villanucci
G. Davidson

APPROVED FOR PUBLIC RELEASE;
DISTRIBUTION UNLIMITED.

THIS WORK SPONSORED BY THE DEFENSE NUCLEAR AGENCY
UNDER RDT&E RMSS CODE B322077462 I25AAXYX96003 H2590D.

X960

Prepared for

Director
DEFENSE NUCLEAR AGENCY
Washington, D. C. 20305

388 596

UNCLASSIFIED

SECURITY CLASSIFICATION OF THIS PAGE (When Data Entered)

REPORT DOCUMENTATION PAGE		READ INSTRUCTIONS BEFORE COMPLETING FORM
1. REPORT NUMBER DNA 4303F	2. GOVT ACCESSION NO.	3. RECIPIENT'S CATALOG NUMBER
4. TITLE (and Subtitle) ASSESSMENT AND EVALUATION OF SIMULATION DATA HAES Report No. 69		5. TYPE OF REPORT & PERIOD COVERED Final Report for Period 1 Mar 77—15 Oct 77
		6. PERFORMING ORG. REPORT NUMBER PhM-01-78
7. AUTHOR(s) I. L. Kofsky D. P. Villanucci G. Davidson		8. CONTRACT OR GRANT NUMBER(s) DNA 001-77-C-0208 New
9. PERFORMING ORGANIZATION NAME AND ADDRESS PhotoMetrics, Inc. 442 Marrett Road Lexington, Massachusetts 02173		10. PROGRAM ELEMENT, PROJECT, TASK AREA & WORK UNIT NUMBERS NWET Subtask I25AAXYX960-03
11. CONTROLLING OFFICE NAME AND ADDRESS Director Defense Nuclear Agency Washington, D.C. 20305		12. REPORT DATE 15 November 1977
		13. NUMBER OF PAGES 140
14. MONITORING AGENCY NAME & ADDRESS(if different from Controlling Office)		15. SECURITY CLASS (of this report) UNCLASSIFIED
		15a. DECLASSIFICATION/DOWNGRADING SCHEDULE

16. DISTRIBUTION STATEMENT (of this Report)

Approved for public release; distribution unlimited.

17. DISTRIBUTION STATEMENT (of the abstract entered in Block 20, if different from Report)

18. SUPPLEMENTARY NOTES

This work sponsored by the Defense Nuclear Agency under RDT&E RMSS Code B322077462 I25AAXYX96003 H2590D.

19. KEY WORDS (Continue on reverse side if necessary and identify by block number)

Nuclear-Effects Simulation
Photometry of Aurora
Excitation of Air
Infrared Radiation
Upper Atmosphere
Radiation Transport

microns

20. ABSTRACT (Continue on reverse side if necessary and identify by block number)

Radiance data from the charged particle-stimulated ionosphere in the wavelength band 4.2-4.3 μm (from ICECAP/HAES multi-instrumented rocket A18.219-1, 1974) are evaluated; the performance of two diagnostic photometer systems flown on sounding rockets is assessed; a procedure for determining pointing relative to prompt and past air excitation of a rocket-borne interferometric spectrometer (on IC630.02-1A (HIRIS II), 1976) is developed; and photometry and positioning data for 1976 aircraft flights at over

DD FORM 1 JAN 73 1473 EDITION OF 1 NOV 65 IS OBSOLETE

UNCLASSIFIED

SECURITY CLASSIFICATION OF THIS PAGE (When Data Entered)

C O2(++)

20. ABSTRACT (Continued)

auroral latitudes to measure spatial structure in infrared radiance are presented.

microns (approximately 5 - 15 deg)

The radiation flux near 4.3μm at low elevation angles, (~5°-15°) has both layering irregulatiries and a component associated with prompt energy deposition in the atmosphere. The altitude structure is interpreted as an effect of adding collisional transfer of N_2 vibrational energy excited by aurora-producing particles to the population of CO_2 by transport of thermal radiation. Aeronomic mechanisms that could be responsible for the near-prompt infrared mechanism are reviewed critically, and further measurements to select among these processes and to identify the radiating molecular species are suggested.

A photometer with wavelength response designed to simulate that of calibrated photographic cameras, such as were used to image the glows from past nuclear explosions, ~~is found to~~ perform ed essentially as expected. One intended to determine column intensity in the weak N^2D - ^4S doublet requires further modification. Zenith radiances from AFGL/DNA's NKC-135 aircraft in five auroral-emission features, two (or three) of which are applied in determining the altitudes at which energy is deposited, are presented for eight aircraft missions in which the spatial variations (and spectral distribution) of radiation near 2.8μm were measured by instruments coaligned with the multichannel photometer.

SUMMARY

The objective of the program reported here is to assess and evaluate in terms of nuclear explosion-induced sky backgrounds, optical/infrared radiation data from DNA-sponsored measurements on the disturbed auroral ionosphere. Six individual topics, involving observations of emission near 4.3μm and assessments of energy input that resulted in emissions at 2.8μm and in the spectral band 4-22μm, are considered.

Altitude profiles of radiation density in the 4.2-4.3μm band at low elevation angles when the ionosphere is bombarded by charged particles, which are unique to HAES-ICECAP rocket A18.219-1 (1974), are presented and partially evaluated in Section I. Substantial layering (altitude irregularity) of the radiant flux in the disturbed region is observed. Section II reviews potential sources of the largely-unexpected prompt fluorescence-associated component of the atmosphere's radiation in this wavelength band, and suggest further field investigations to determine its origin. The internal consistency of these 4.3μm radiance and instrument-pointing data is evaluated critically.

Section III assesses the performance of a photometer designed to measure in the wavelength band over which photographic cameras using panchromatic film are sensitive. This Film Response Photometer provides a link between the infrared radiant intensities resulting from excitation by naturally-occurring energetic charged particles and those from particles and photons output by nuclear explosions. A similar evaluation of a dual channel differential photometer intended to measure column-concentrations of the $NO^{\ddagger}$ precursor species N^2D is in Section IV. The former instrument is found to behave about as expected, and the latter requires modification if it is to perform effectively.

Procedures for determining pointing of the high resolution infrared (4-22μm) spectrometer HIRIS II on rocket IC630.02-1A (01 Apr 76) against the dynamically-excited auroral ionosphere are presented in Section V. Section VI, with Appendixes I and II, lists auroral characterization and aircraft positioning data for the eight ICECAP 1976 missions of NKC-135 A/C 55-3120 in which spatial variations of the upper atmosphere's radiance at wavelengths near 2.8μm were measured.

PREFACE

The High Altitude Effects Simulation (HAES) Program sponsored by the Defense Nuclear Agency since the early 1970 time period, comprises several groupings of separate, but interrelated technical activities, e.g., ICECAP (Infrared Chemistry Experiments – Coordinated Auroral Program). Each of the latter have the common objective of providing information ascertained as essential for the development and validation of predictive computer codes designed for use with high priority DoD radar, communications, and optical defensive systems.

Since the inception of the HAES Program, significant achievements and results have been described in reports published by DNA, participating service laboratories, and supportive organizations. In order to provide greater visibility for such information and enhance its timely applications, significant reports published since early calendar 1974 shall be identified with an assigned HAES serial number and the appropriate activity acronym (e.g., ICECAP) as part of the title. A complete and current bibliography of all HAES reports issued prior to and subsequent to HAES Report No. 1 dated 5 February 1974 entitled, "Rocket Launch of an SWIR Spectrometer into an Aurora (ICECAP 72)," AFCRL Environmental Research Paper No. 466, is maintained and available on request at DASIAC, DoD Nuclear Information and Analysis Center, 816 State Street, Santa Barbara, California 93102, Telephone: (805) 965-0551.

This report, which is the final report on Contract DNA001-77-C-0208 and No. 69 in the HAES series, covers PhotoMetrics' activities in accessing and evaluating field data on infrared backgrounds in the period 01 Mar - 15 Oct 1977. It makes frequent reference to procedures developed for accessing data from sounding rockets and flights of instrumented aircraft at high latitudes, preliminary results, and comparison material on ICECAP investigations other than those reported here, contained in our previous HAES reports 4, 27, and 59 (Ref's 1, 2, and 3).

In addition it applies information recently derived from simulations of the effects of nuclear explosions in exciting atmospheric radiations that was presented at the HAES Infrared Data Review held in Falmouth, MA 13 - 15 Jun 77 (Ref 4). Considered in the report are data from the following HAES-ICECAP sources –

Multi-instrumented rocket A18.205-1, 27 Mar 73

Multi-instrumented rocket A18.219-1, 25 Feb 74

Multi-instrumented rocket IC519.07-1B, 22 Mar 75

Interferometric spectrometer-carrying rocket IC630.02-1A(HIRIS II), 01 Apr 76

USAF NKC-135A 55-3120 (Air Force Geophysics Laboratory's IR-Optical Flying Laboratory) aircraft missions between 22 Feb and 28 Mar 76, performed under program heading ICECAP 76.

This work was under the direction of I. L. Kofsky, to whom questions about it should be addressed. D.A. Gentile contributed to the photoreproduction and artwork, and Mrs. C.A. Rice was responsible for typing the manuscript. Supporting information was provided by many of the staff of the Air Force Geophysics Laboratory's OPR branch, in particular J. Kennealy and P. Doyle, and by T.C. Degges of Visidyne, Inc. The flight logs in Appendix II were prepared by J. Reed of Visidyne. The authors gratefully acknowledge the support and encouragement of A.T. Stair, Jr., and J.C. Ulwick of AFGL and of C.A. Blank of the Defense Nuclear Agency.

TABLE OF CONTENTS

TABLE OF CONTENTS (continued)

LIST OF ILLUSTRATIONS

LIST OF ILLUSTRATIONS (continued)

LIST OF ILLUSTRATIONS (continued)

LIST OF ILLUSTRATIONS (continued)

LIST OF TABLES

SECTION I

4.3μm RADIATION PROFILES AT LOW ELEVATION ANGLES

INTRODUCTION

This Section presents and provides a preliminary interpretation of altitude profiles of radiance of the auroral particle-excited ionosphere in the 4.21 - 4.305μm full-width-to-half-maximum-response (FWHM) wavelength band, measured at elevation angles $\sim 5^{o}$ - 15^{o} by the sidelooking filter radiometer on ICECAP multi-instrumented rocket A18.219-1 (launched from Poker Research Range on 25 Feb 74). The data from this rocket probe constitute the only available coherent set characterizing the disturbed atmosphere's "4.3μm" radiance distribution at these low elevation angles and long radiating path lengths.

Spectral response of the radiometer and the spectrum of the optically-grey-to-thick (001-000) band of CO_2, which dominates the signal (refer to the discussion in Ref 5), are in Fig 18 of Section II. The radiometer's field of view is about 6^{o} circular (its angular sensitivity is that plotted in the left-hand diagram of Fig 20 of Ref 3). Rocket spin rate is 2.0 revolutions/sec. A major adjustment in the angles at which the instruments point within the radiating volume is derived in the following subsections, and other corrections that were applied to the 4.3μm data are described in the text. The effect of this change in elevation angles on interpretation of data from the 2.42 - 4.311μm (FWHM) sidelooking radiometer on the same rocket is briefly noted.

A preliminary review of some of these A18.219-1 data, with one comparison of altitude profiles measured on upleg and downleg (where the radiance levels are substantially higher), appears in Ref 3, p 104 ff. An evaluation of the increases in the sidelooking 4.3μm-band radiometer signals closely associated with auroral excitation, which do not impact significantly the radiance profiles presented in this Section, is the subject of Section II of this report.

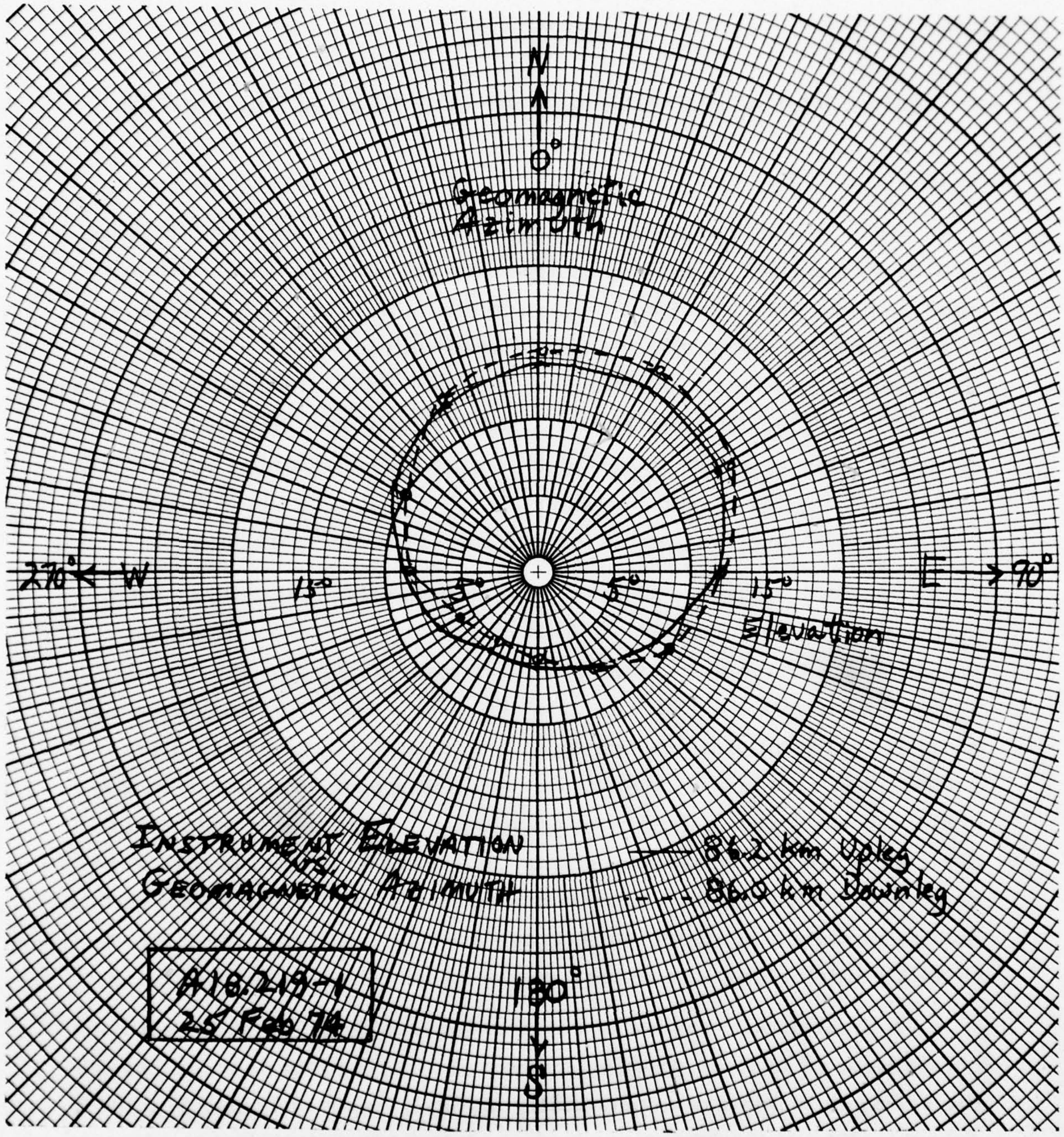

Figure 1. Elevation-azimuth plot for the side-looking photometers and radiometers after stabilization of A18.219-1.

INSTRUMENT ELEVATION AND AZIMUTH – GENERAL

We establish first the directions in which the set of sidelooking radiometers and photometers on A18.219-1- was pointing. The original data on rocket orientation, as noted in our previous report (Ref 3), were inconsistent with the expected projection on the instruments' fields of view of the auroral arc's known geometry. A 60° offset in the readings from the rocket's gyro system was tentatively identified by the rocket housekeeping group, which places geomagnetic N at 89° on the geographic-azimuth scales (as for example in Fig 34 of Ref 3). Our preliminary reduction of A18.219-1 data assumed that the elevation angles reported by the rocket group needed no such correction. While errors in the instruments' elevation angle have only secondary effect on our findings about aurora-associated emission near 2.8μm (Sections I and II of Ref 3), accurate pointing is needed to understand the spatial distribution of excitation of the incoming charged particles, ranges to and thus altitudes of emitting regions, 2.8μm-band backgrounds at the lower rocket altitudes, and particularly, the dependence on elevation angle of the disturbed atmosphere's radiance in the 4.3μm-filter band. (Elevation-azimuth is henceforth abbreviated as $e\ell$-az.)

Eℓ-az data in the aspect report (Ref 6), however, indicate that any phase shift applied to the azimuth scale must be applied also to the elevation scale. Specifically, the information on zenith angle of the rocket's long axis and its azimuth with respect to true N, whose accuracy is not in question, fixes the azimuths of maximum and minimum elevation of the sidelooking instruments. As an example, near 85 km on upleg the tilt of the rocket axis from vertical is $5\frac{1}{2}^{\circ}$ at geographic azimuth 231°, and therefore the instruments (which point 80° from the spinning rocket's axis) will have a minimum $e\ell$ of $4\frac{1}{2}^{\circ}$ where their az is 231°, and a maximum of $e\ell$ of $15\frac{1}{2}^{\circ}$ near 51° az; refer to Fig 1. The telemetered $e\ell$-az data show that both scales must be shifted together to maintain these minimum and maximum elevations at the expected azimuth angles. A corrected version of Ref 3's Fig 33

(Fig 1) shows the instruments' pointing after stabilization is achieved, for the 90^{o} azimuth shift that we determine here. Shifting the $e\ell$-az scales together results in an almost complete reversal of the high and low elevation angles.

CORRECTION OF EL-AZ

We applied three procedures for determining quantitatively the offset in the elevation-azimuth scales, results from which were in very good agreement.

Our first efforts were directed toward comparing visible-radiance distributions resulting from the geometry of the rocket and arc to those from the 1973 multi rocket probe (A18. 205-1). Launch azimuths of the two rockets were nearly the same and zenith angles of their long axes were within $2\frac{1}{2}^{o}$ after stabilization, and an arc lay to the N on upleg of each trajectory. Therefore the sidelooking A18. 219-1 instruments on upleg pointed at the arc at elevation angles not substantially different from those of A18. 205-1 (compare, for example, Fig 1 with Fig 23 of Ref 2), although since the ranges to the excited air volumes are not the same the intercept altitudes of the fields of view would be expected to differ.

In the 1973 measurements the azimuth angles east and west of the geomagnetic meridian at which the arc limb enhancements maximized differ from one another by only 10^{o} to 15^{o}(even after the rocket had penetrated the arc); typical angles were 73^{o}E and 63^{o}W (see Fig 2 of Ref 3). In the 1974 measurements, on the other hand, this azimuth difference is $\sim 50^{o}$ even after a 60^{o} shift was applied to the azimuth scales (see Fig 34 of Ref 3). That is to say, from A18. 219-1 the angular positions of the van Rhijn-like enhancements are offset relative to magnetic N. The argument that the maxima should be symmetric about the meridian does not locate the meridian with good resolution, since the azimuth angles at which the limb brightnesses peak depend on the arc's E-W alignment and excitation uniformity as well as on

the elevation angles at which the instruments view the emitting volume. Considering the apparent E-W uniformity of the arc on rocket upleg, however, it does indicate that the azimuth must be shifted by more than 60° to make the data consistent with the known viewing geometry. (An 85° shift would restore symmetry to the limb peak azimuths.)

A <u>second</u>, potentially more accurate method of assessing the offset is to fit the elevation angle dependence of the $4.3\mu m$ atmospheric radiance to that expected from a simplified layer-thickness model, such as we adopted in evaluating the 1973 multi's $5.3\mu m$ radiometer data (Fig 21 of Ref 3). The rocket spin-correlated cyclical radiance variation observed at $5.3\mu m$ (Fig 23 of Ref 3) is a result of a convolution of the radiometer's (broad) field of view with the altitude profile of earth limb radiance. A plot of this background intensity against the (path length-proportional) cosecant of the radiometer axis' elevation angle (Fig 21 Ref 3) showed that at a fixed rocket altitude, the $5.3\mu m$ signal increases about linearly with effective path length through the atmosphere.

Although the atmosphere is not optically thin to radiation in the $4.3\mu m$ band at the lower rocket altitudes and elevation angles, roughly-similar cyclical background variations correlated with the path lengths might be expected. (A simple manifestation of this effect is that the maximum radiance, in the absence of any azimuthal dependences induced by localized dosing that increases "anisotropically" the vibrational temperature of the CO_2 molecules responsible for most of the $4.3\mu m$ radiation, would be located at the minimum elevation angle.) The $e\ell$-az scans from 111 and $102\frac{1}{2}$ km (Fig 2) illustrate such van Rhijn-like cyclical radiance distributions, with greater fractional modulation at the higher rocket altitude where fewer of the rotational lines from distant CO_2 molecules in the field of view are reabsorbed. (The ratio (peak - trough)/(peak + trough) is a factor 2 higher at the higher altitude.)

To implement this approach, we plotted the radiances from $e\ell$-az scans at three rocket altitudes on downleg against the cosecant of the

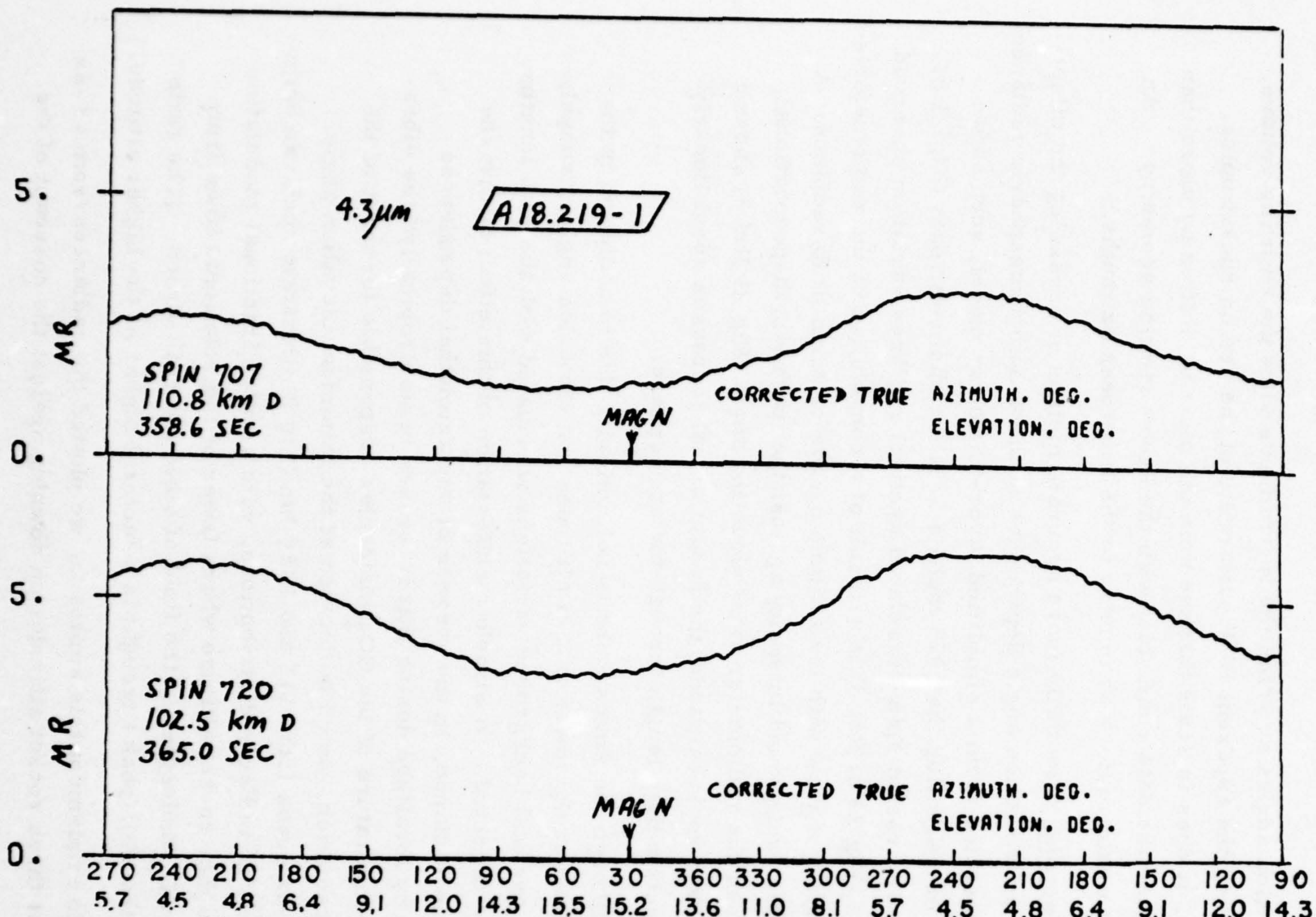

Figure 2. 4.3μm radiometer azimuth-elevation spin cycles near 110 and 102 km on downleg of A18.219-1, showing the van Rhijn-like, cyclically-varying radiance.

radiometer axis' elevation angle, *for shifts* between 0° and 120° in the azimuth scale (Fig's 3a-c). The plots fail to close because of the increase in the atmosphere's radiance over the ~0.65 km altitude decrease during the 1/2-sec spin cycle; this increase is 6% near 103 km, for example. An azimuth shift of $87^{\circ} \pm 5^{\circ}$ best reproduces the expected dependence on elevation angle (recall that we have assumed no azimuthal dependence).

The 4.3μm radiance varies about linearly with atmospheric path length at the higher instrument elevation angles and rocket altitudes in Fig 3; conversely, at 103 km the curve "bows over" as more rotational lines become optically thick. This behavior is in qualitative agreement with the known transport of CO_2 radiation near 4.3μm in this altitude range (Ref 5). It is further shown in a summary of plots for rocket altitudes between 98 and 116 km (Fig 4), which apply an 85° offset in the azimuth-dependent change in elevation angles. As the altitude of observation decreases the path length dependence becomes less linear, and the onset of the "bow" moves to higher elevation angles.

A third, and most compelling, piece of evidence about the instrument pointing is provided by a narrow (~5° FWHM) feature which appears in $e\ell$-az scans of both channels of the N^2D differential photometer (Section IV) during most of the upleg and downleg segments of A18.219-1's trajectory. We have determined that the excess signal, which is located near 295° azimuth on the uncorrected plots, is caused by the -1.6 magnitude star Sirius (α Canus Majoris) passing through the 5° field of view of the photometer. The general appearance of its field-convolved angular distribution of radiance is shown in Fig 29 of Section IV. Both the celestial coordinates of and irradiance from Sirius verify this identification, as we show from an assessment of the photometer data from a region of downleg near 190 km rocket altitude, where the auroral signal is low.

Narrative text continues on page 22.

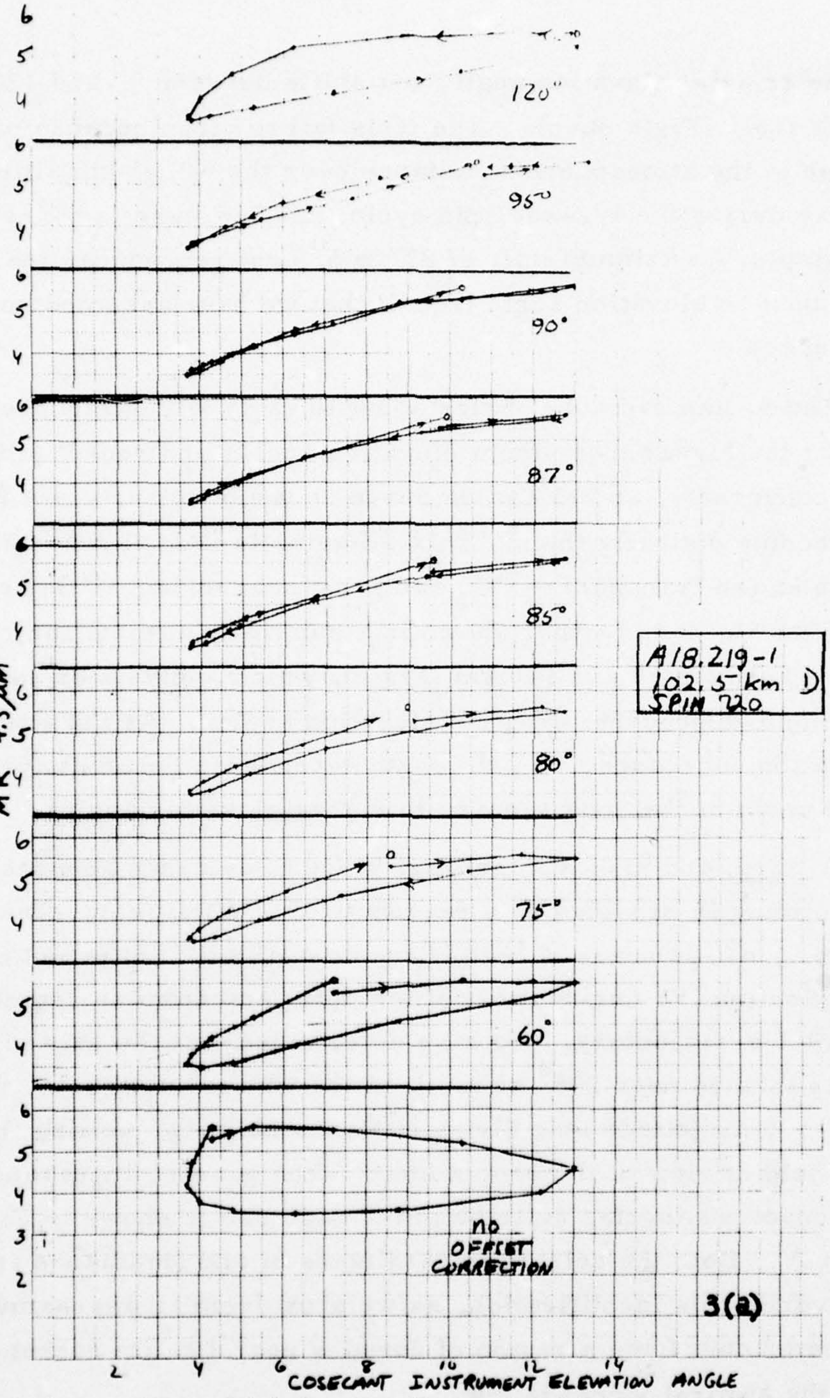

Figure 3a-c. Plots of 4.3µm radiance against cosec of elevation angle of the radiometer's axis as a function of shift in the elevation-azimuth scales, for rocket altitudes between 116 and 103 km, A18.219-1 downleg.

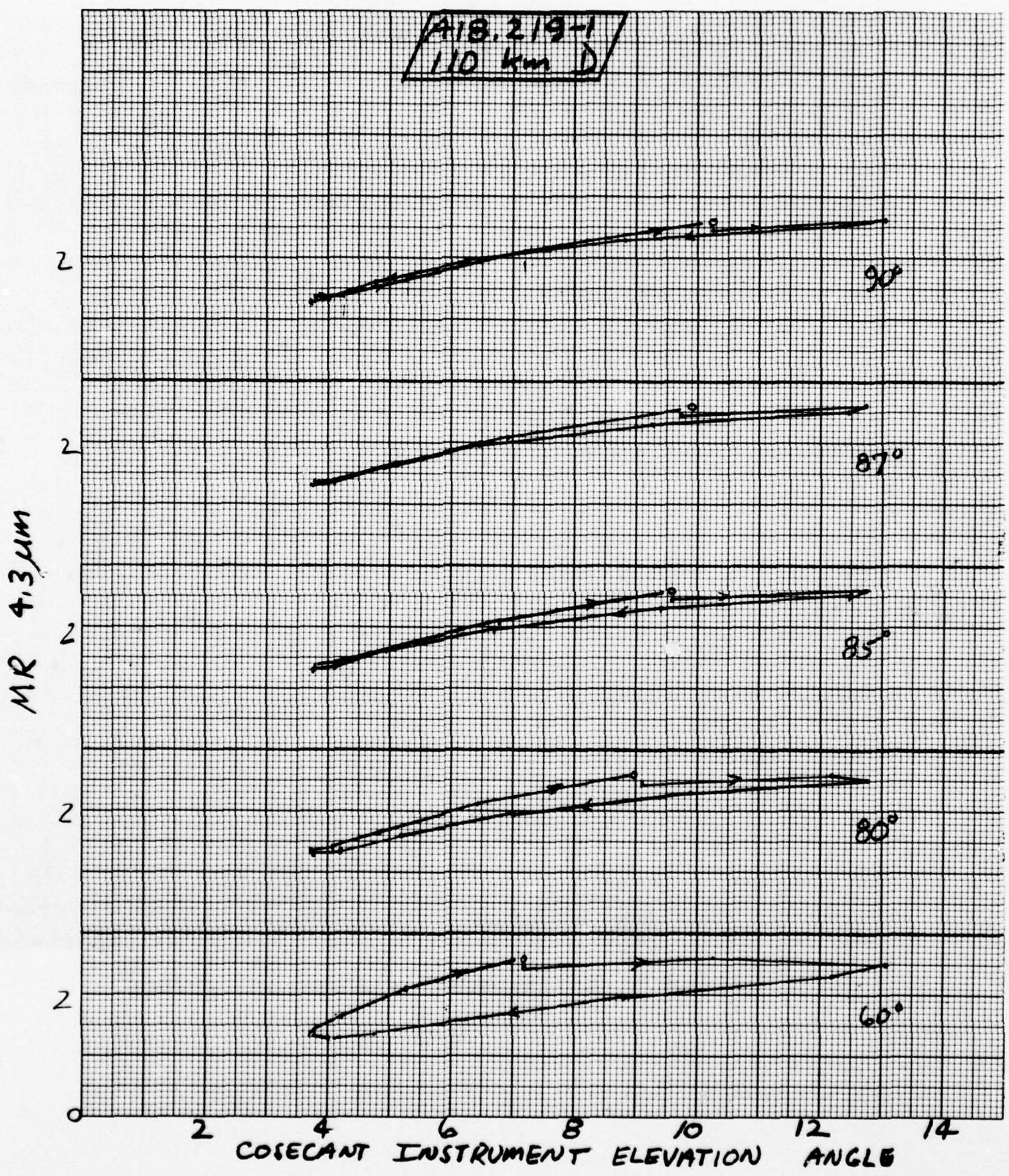
A18.219-1
110 km D
MR 4.3 µm
2
2
2
2
2
0
90°
87°
85°
80°
60°
2
4
6
8
10
12
14
COSECANT INSTRUMENT ELEVATION ANGLE

3(b)

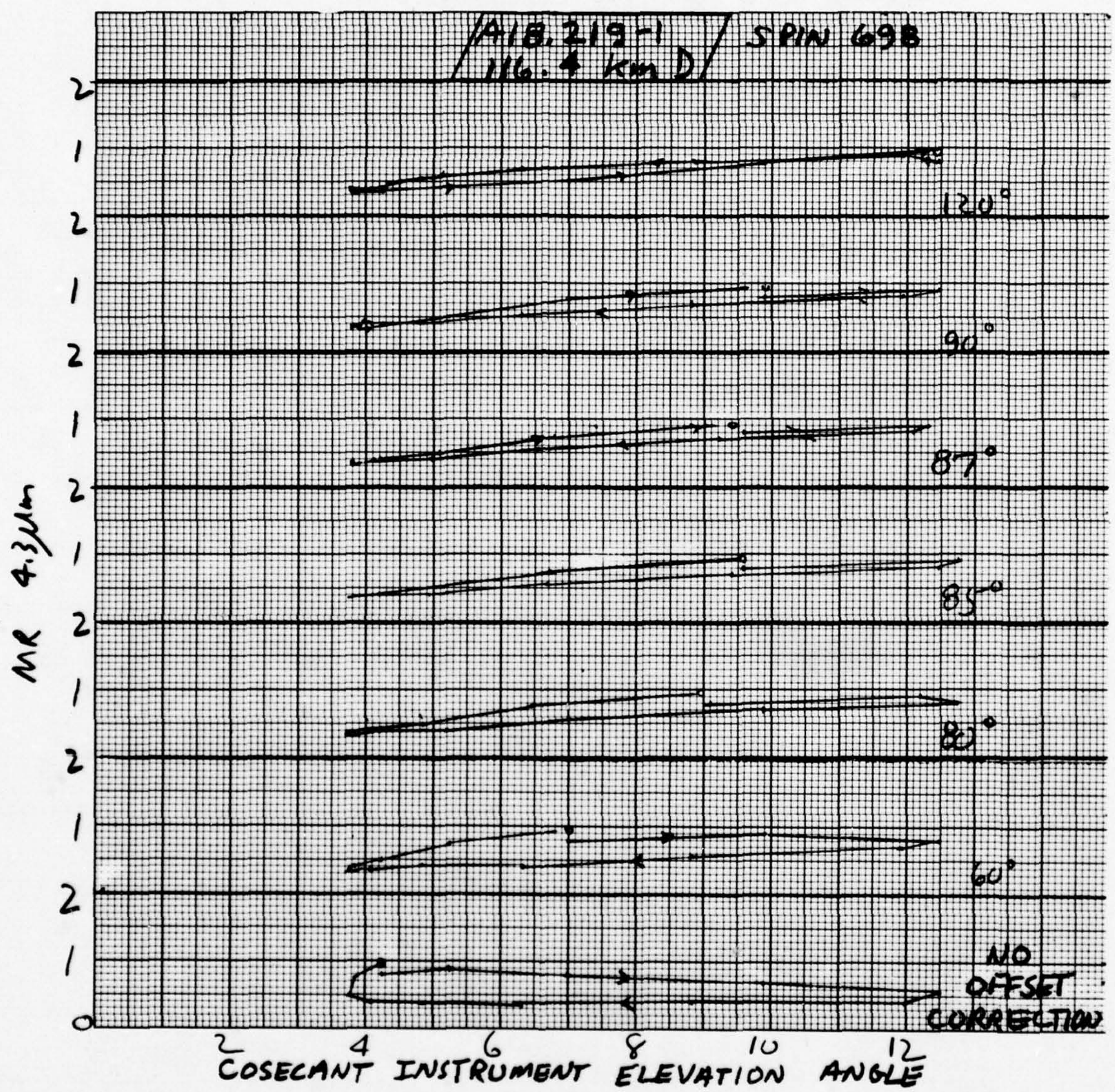
A18.219-1 / SPIN 698
116.4 km D
MR 4.3μm
120°
90°
87°
85°
80°
60°
NO OFFSET CORRECTION
COSECANT INSTRUMENT ELEVATION ANGLE

3(c)

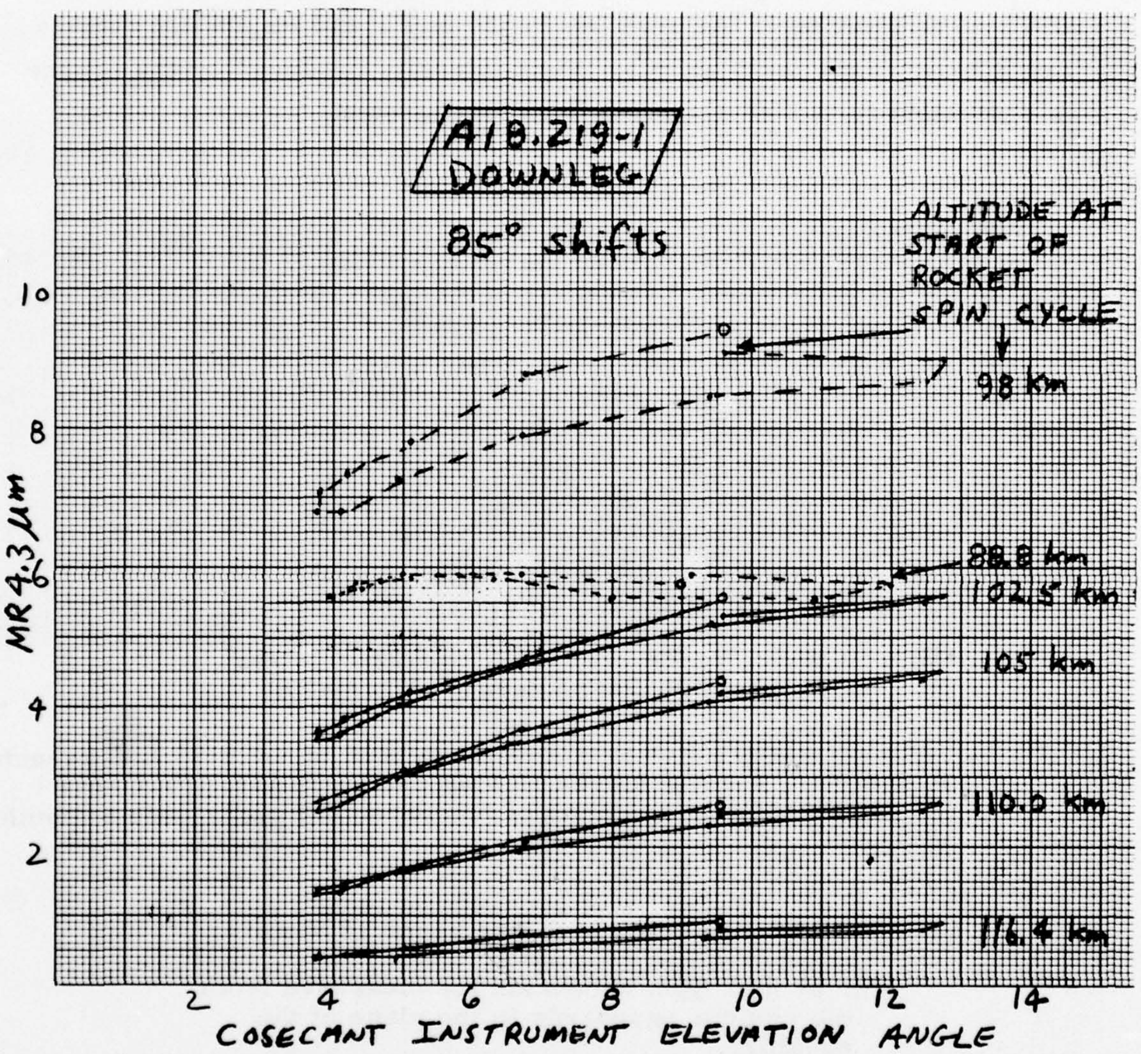

Figure 4. Summary of plots of 4.3μm radiance against cosec of elevation angle of the radiometer's axis applying an 85° shift in elevation-azimuth scales, A18.219-1 downleg. The data presentation is complementary to that in Fig's 3a-c, as it shows the elevation angle dependence of radiance for rocket altitudes between 116 and 98 km (the spread in the plot for 88.8 km is due to the azimuth-dependent enhancement, Section II).

An average of ten spins from the wider band channel of the photometer is shown in Fig 5 for (uncorrected) geographic azimuths near 295°. The position of the peak is at $295\frac{1}{2} \pm \frac{1}{2}^{\circ}$, and its FWHM above a 150 R background is $5^{\circ} \pm \frac{1}{2}^{\circ}$. Peak intensity produced by the source is equivalent to 0.2 kR above the local background.

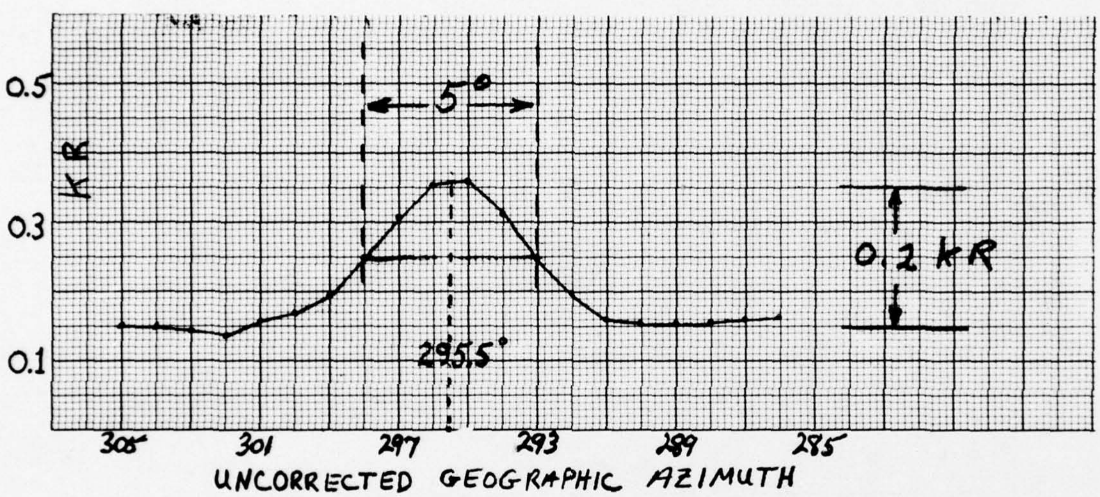

Figure 5. Radiance distribution in wideband channel of the 5199 Å differential photometer, averaged over 10 spin cycles of A18.219-1 near 190 km altitude in the range of (uncorrected) geographic azimuths 305°-286°.

The celestial coordinates of Sirius epoch 1974 were:

6 hr 44 min right ascension (as measured from the equinox eastwards in the plane of the equator,

$-16^{\circ} 40' 46''$ declination (measured perpendicular to the equator, positive to the N).

We calculated the hour angle and declination of Sirius relative to the rocket's position at 190 km downleg (144° longitude, 66° N latitude at 0742:50 UT). These coordinates, converted to geographic azimuth and elevation angle above local horizontal at the rocket's altitude, are:

204.9° geographic azimuth, 5.1° elevation.

Thus the correction in geographic azimuth is $204.9^{o} - 295.5^{o} = -90.6^{o}$ from that indicated in the housekeeping data, that is, all original azimuths are moved eastward by 1/4 revolution. The elevation at the narrow peak, when both azimuth and elevation scales are shifted together (as is required on the basis of the rocket-axis aspect data discussed earlier) is 5.3^{o} at the corrected azimuth of 205^{o}. This is in satisfactory agreement with the elevation of Sirius, particularly when it is considered that the star does not necessarily pass exactly across a diameter of the radiometer's circular field.

The response of the wider channel of the 5199 Å photometer to a point source producing the spectral irradiance of Sirius results in an equivalent radiance output of 0.19 kR; compare the approximately 0.2 kR in Fig 5. Since the weak air fluorescence-chemiluminescence averaged over the wider band near 5200 Å produces an irradiance at the photocathode only comparable to that from Sirius, the star is readily detectable in this photometer's signal. It is also detectable, with lower signal/background, in the ℓ-az scans of the narrow-band channel of the differential photometer. On the other hand no indication of this feature appears in either the 3914 Å or 5577 Å photometer data, since its equivalent radiance at these wavelengths would be only about 0.1 - 0.2 kR; the narrow source would be unresolvable over the typically 10 to 40 kR auroral levels near the same azimuth.

The net result of this investigation is that the first-reported azimuth and elevation scales must be shifted together by $90^{o} \pm 1^{o}$ in azimuth. Thus we have located geomagnetic N at 119^{o} ($90^{o} + 29^{o}$) on the original geographic azimuth scales for assessing the CO_2 radiance data. Since the radiometer/photometer elevations change only slowly with azimuth (Fig 1), small errors in this azimuth shift have only second-order effect on calculations of ranges to or altitudes of emitting regions. For example a 5^{o} error in azimuth at either the maximum or minimum instrument elevation angles of $15\frac{1}{2}^{o}$ and $4\frac{1}{2}^{o}$ results in an error of only 0.1^{o} in elevation; near 135^{o} geographic azimuth, where

the elevation angle is changing most rapidly, an uncertainty of 5° of azimuth produces the maximum elevation error of about 0.5°. Thus the plots in Fig 4 are complementary to the altitude profiles in Fig 6 for the series of azimuths-elevations, in that they represent the dependence of 4.3μm radiance on elevation angle at a series of altitudes above the radiance peak.

EFFECT OF THE ELEVATION ANGLE CORRECTION ON INTERPRETATION OF 2.8μm RADIANCE DISTRIBUTIONS

The large shift in instrument elevation angles makes the data from the sidelooking 2.8μm radiometer self-consistent at downleg rocket altitudes below 86 km. With the corrected elevations, the 2.42 - 3.11 FWHM background radiances fit a van Rhijn-like enhancement, contrary to our previous assessment (p 98 of Ref 3). Although the measured increases are too high to be explained fully by OH $\Delta v = 1$-band radiation, they could be caused by either leakage of thermal radiation originating from still lower altitudes – a chronic problem with the infrared radiometers – or by the earth-limb features observed from AFGL/DNA's Sept 77 "Spire" spectrometer-carrying rocket IC733.03-1 (which included strong emission near 2.4μm, Ref 7). Thus enhanced limb radiation overlying the features associated with auroral particle-excited air fluorescence, which becomes self-consistent when the instrument's pointing angles are corrected, provides an attractive alternative interpretation of the apparent decorrelation of sidelooking 2.8μm signal from this fluorescence below 86 km (as shown in Fig 49b of Ref 3). (Previous assessments have considered the effect to be caused by a "cloud" of engine exhaust coming into the sidelooking instrument fields as the rocket starts to tip over; this putative cloud has major impact on the interpretation of zenith radiance near 2.8μm, p404 of Ref 4.)

RADIATION PROFILES

Altitude profiles of the atmosphere's radiance in the 4.21 - 4.305μm wavelength band, plotted at 30° azimuth intervals between 130 and 82 km on downleg of A18.219-1's trajectory, are in Fig's 6a-ℓ. The pointing angles, which refer to the radiometer's optic axis, apply the 90° azimuth shift and accompanying elevation shift derived above. The angular field of the instrument is shown in Fig 20 of Ref 3, and its spectral sensitivity in Fig 18 of this report. 4.3μm-band radiances measured by the rocket's near vertical-viewing fixed-filter and wavelength-sweeping (circular variable filter) radiometers (Ref 4, p427 and Ref 8) are shown for comparison in Fig 7. We interpret the low elevation-angle radiance distributions here only to the extent necessary to verify the accuracy of the data from the side-viewing 4.3μm radiometer.

Above 130 km on downleg the signal lies in what appears to be instrument noise. Below 85 km the radiometer's elevation angle at a given azimuth changes rapidly as the rocket's long axis moves through the vertical and then tilts downward, as shown on p433 and p500 of Ref 4. On upleg the data exhibit narrow noise spikes of the type in Fig's 30a and 31a of Ref 3 that disappear by 92 km, after which there remains some excess radiance at geomagnetic azimuths between 240° and 30° (that is, in the northwest quadrant from the rocket ± 30°). Near 110 km this small excess evolves rapidly into an off-scale peak centered at 285° with skirts of 60° azimuthal extent, of the type in Fig 27b of Ref 3, evidence of which persists to ~160 km. As the radiance excess between 92 and 110 km is inconsistent with an increase from van Rhijn effect, it is probably related to the artifact that produces the strong signal over sensibly the same azimuth-angle range at higher altitudes. To provide a partial comparison between upleg and downleg 4.3μm-band profiles, we have plotted the upleg radiances from the uncontaminated azimuths 120° and 210° in Fig's 6f and i. (A more informative comparison can be made by applying the other radiance data from between 30° and 240° azimuth, correcting the 240°→ 30° data set, and filtering the narrow noise spikes present below 92 km altitude.)

Narrative text continues on page 33.

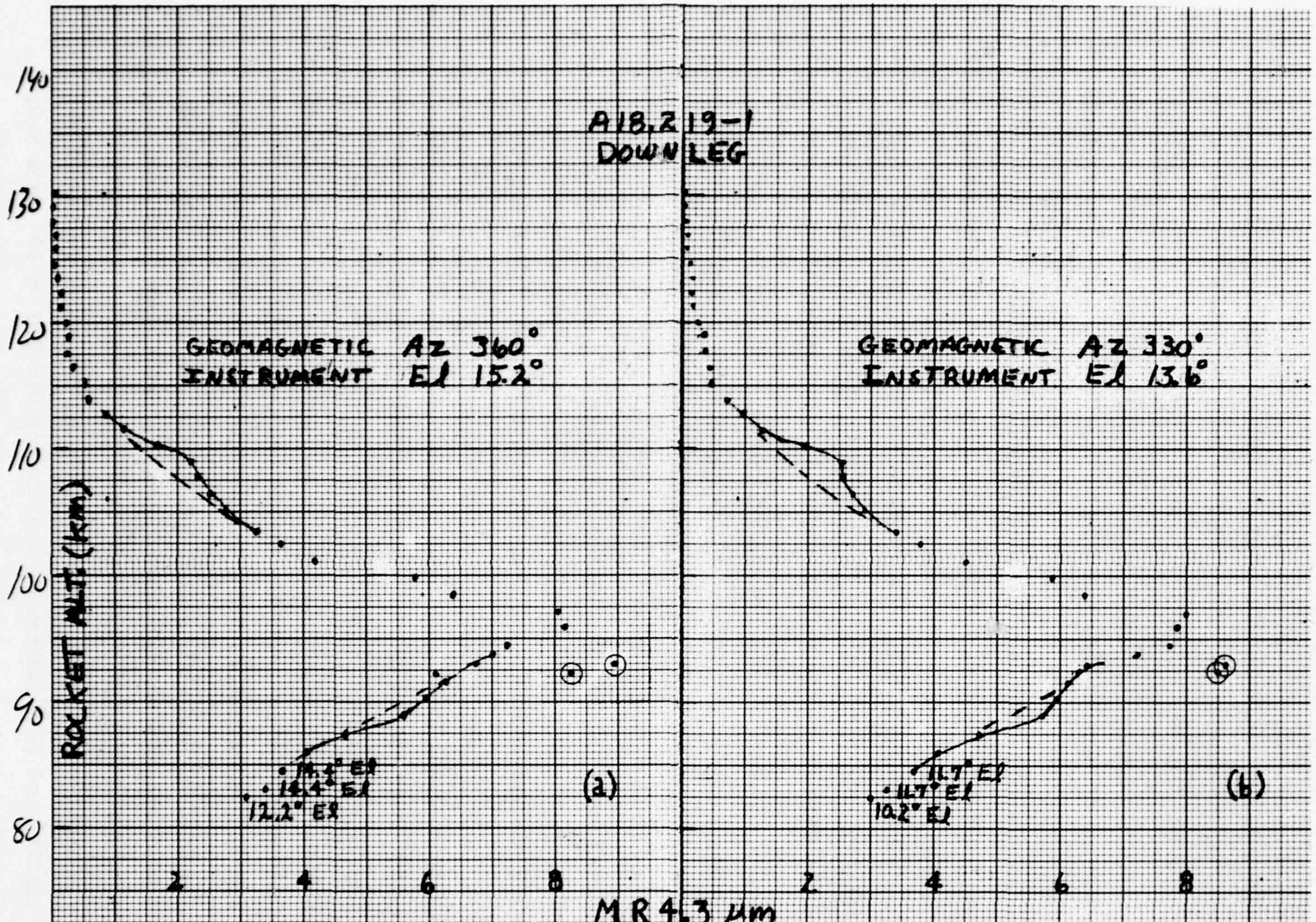

Figure 6a-l. Altitude profiles of 4.3μm radiance measured at 30° azimuth intervals by the side-looking radiometer on downleg of A18.219-1. The numbers next to the points below 85 km are the instrument's elevation angle as the rocket begins to destabilize. Comparison upleg data are included for 120° and 210° geomagnetic, near $5\frac{1}{2}°$ and 9° elevation angle. The circled points have been corrected as described in the text.

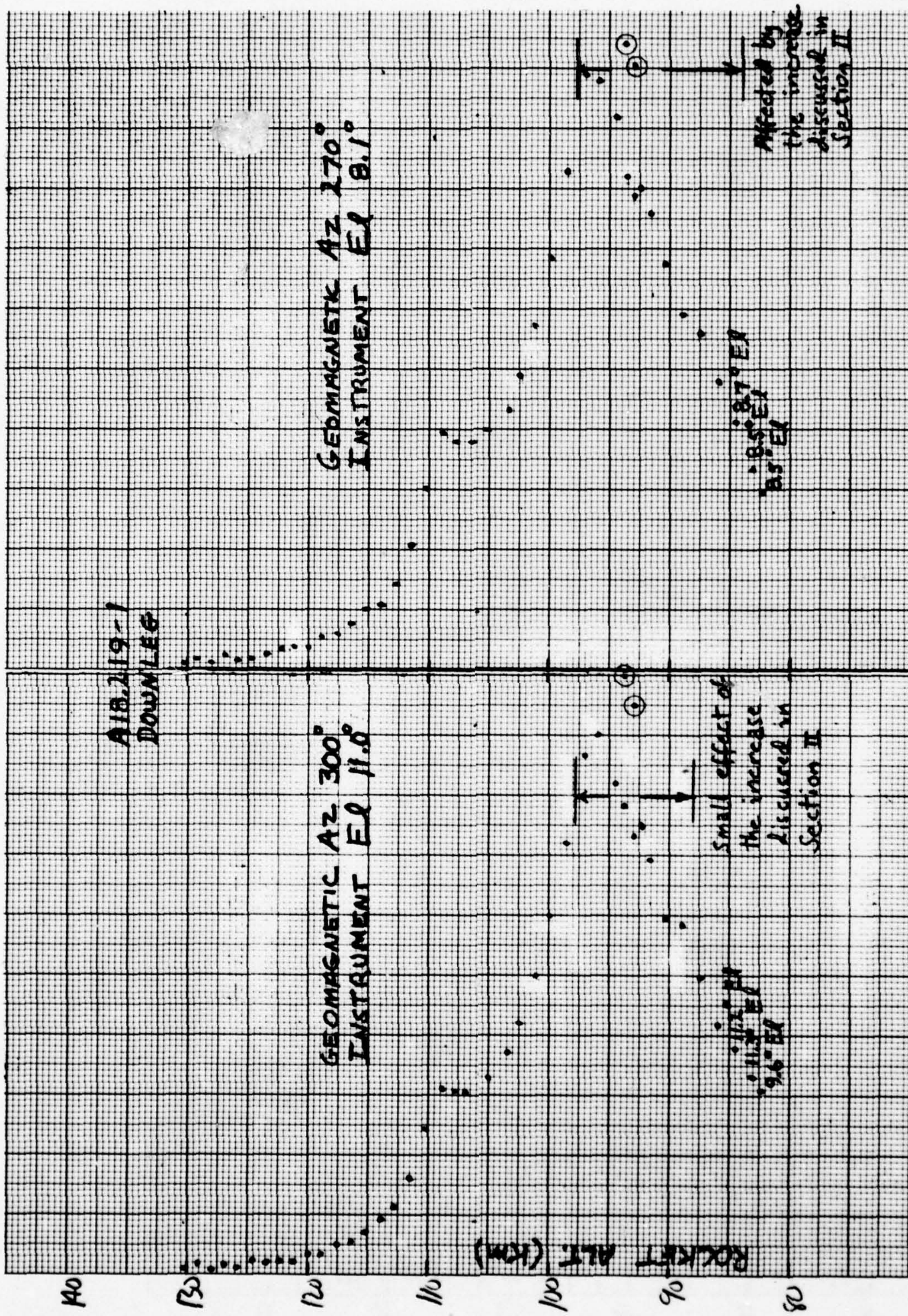

A18.219-1
DOWNLEG
GEOMAGNETIC Az 300°
INSTRUMENT El 11.0°
Small effect of the increase discussed in Section II
GEOMAGNETIC Az 270°
INSTRUMENT El 8.1°
Affected by the increase discussed in Section II
ROCKET ALT (KM)
140
130
120
110
100
90
80
2
4
6
8
10
6(c)
6(d)
MR 4.3 μm

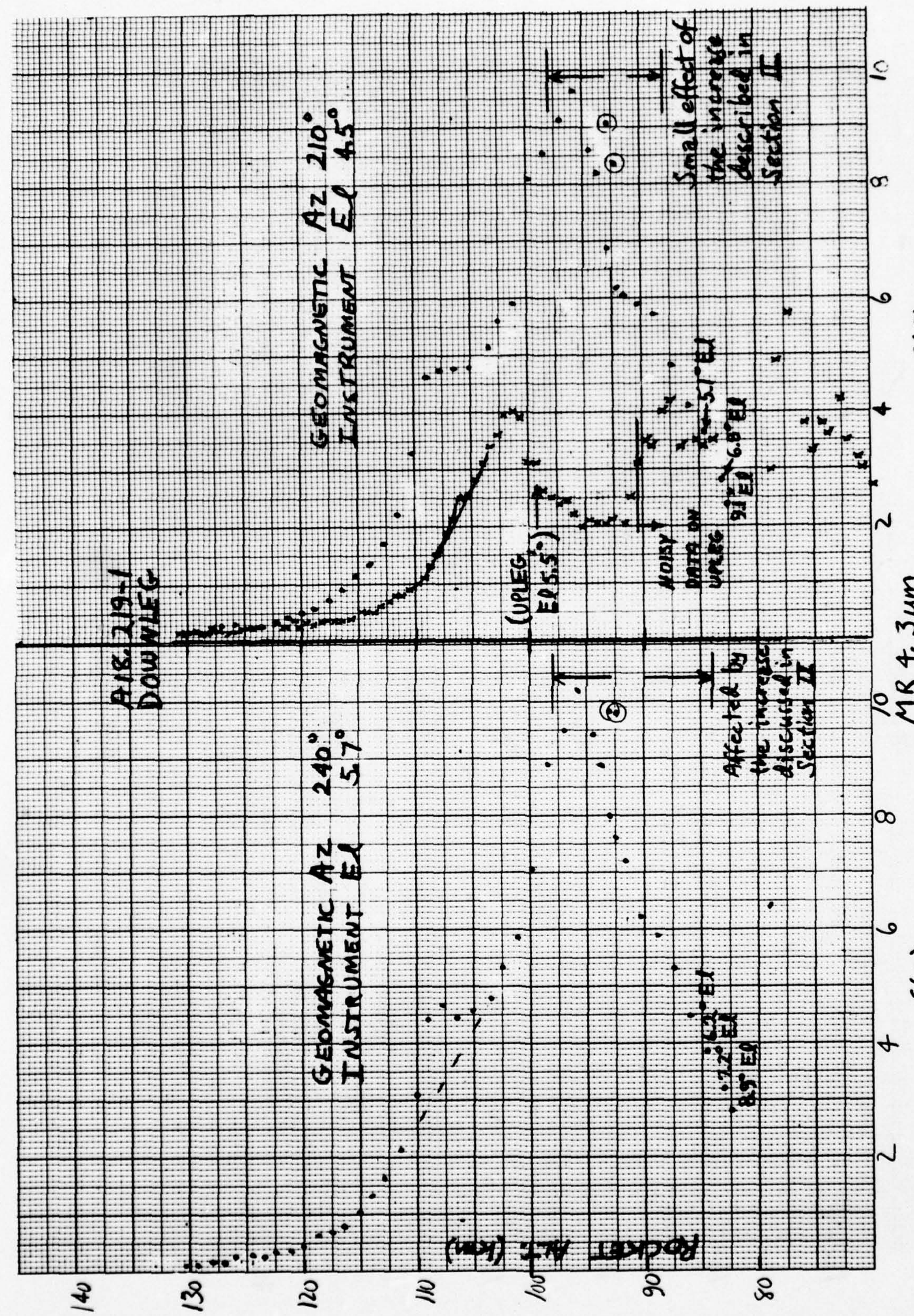
A18.219-1
DOWNLEG
GEOMAGNETIC Az 210°
INSTRUMENT El 4.5°
GEOMAGNETIC Az 240°
INSTRUMENT El 5.7°
(UPLEG El 5.5°)
NOISY DATA ON UPLEG
Small effect of the increase described in Section II
Affected by the increase discussed in Section II
ROCKET ALT (km)
MR 4.3 μm
6(e)
6(f)
140
130
120
110
100
90
80

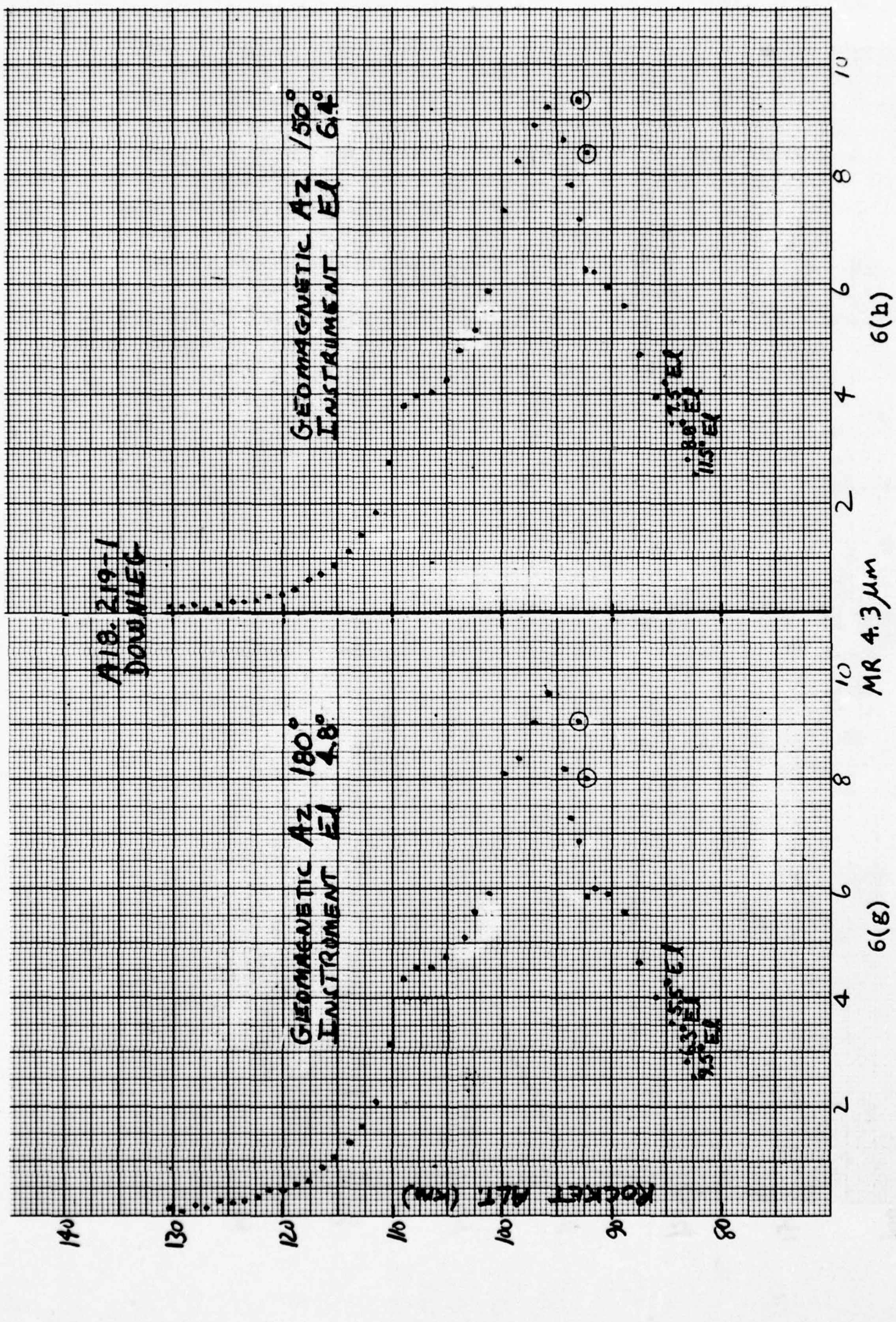
A18.219-1
DOWNLEG
GEOMAGNETIC Az 180°
INSTRUMENT El 4.8°
GEOMAGNETIC Az 150°
INSTRUMENT El 6.4°
ROCKET ALT. (KM)
MR 4.3 μm
6(g)
6(h)
140
130
120
110
100
90
80
2
4
6
8
10

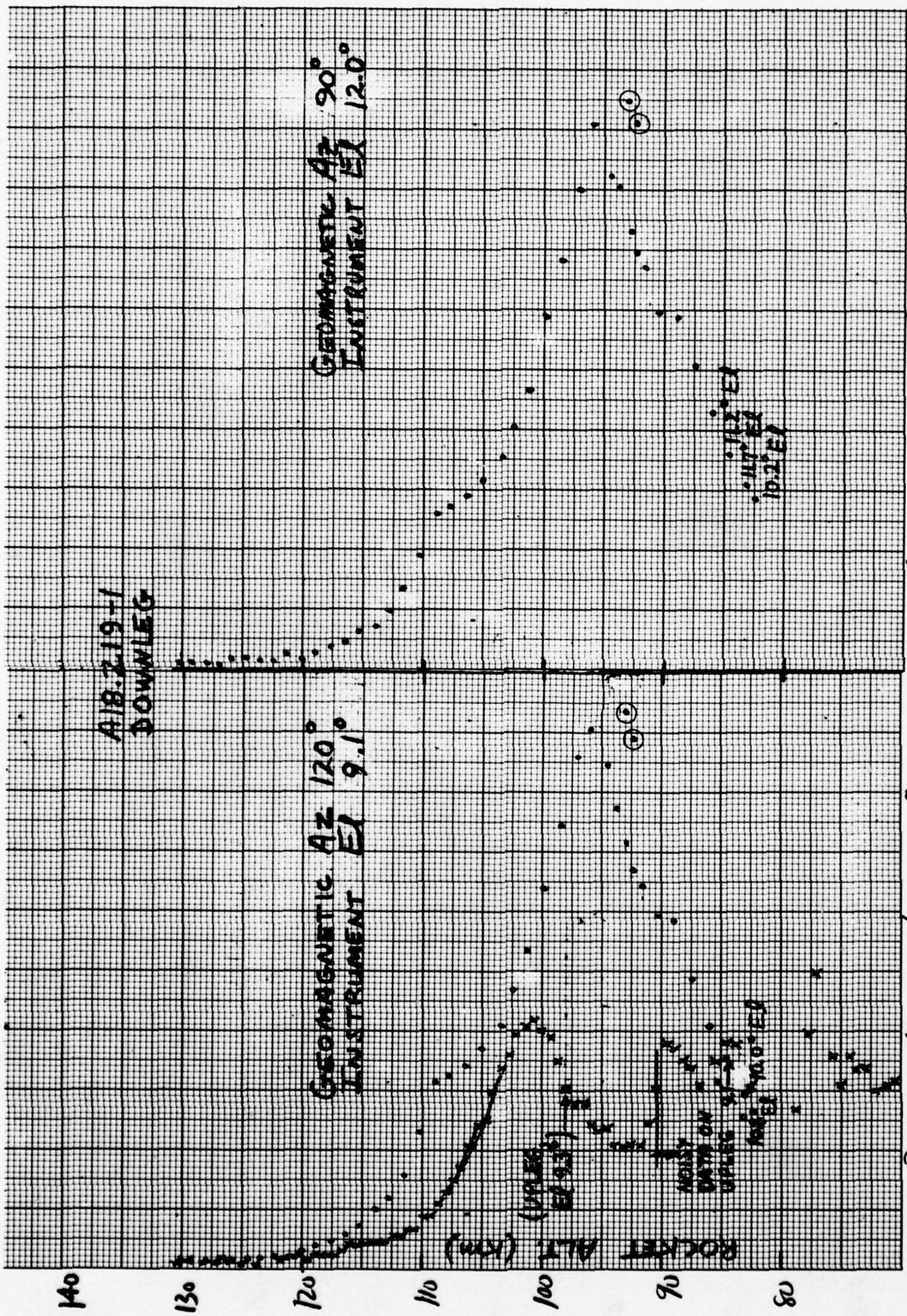
A18.219-1
DOWNLEG
GEOMAGNETIC Az 120°
INSTRUMENT El 9.1°
GEOMAGNETIC Az 90°
INSTRUMENT El 12.0°
ROCKET ALT. (km)
NOISY DATA ON UPLEG
MR 4.3μm
6(1)
6(j)
140
130
120
110
100
90
80
2
4
6
8
10

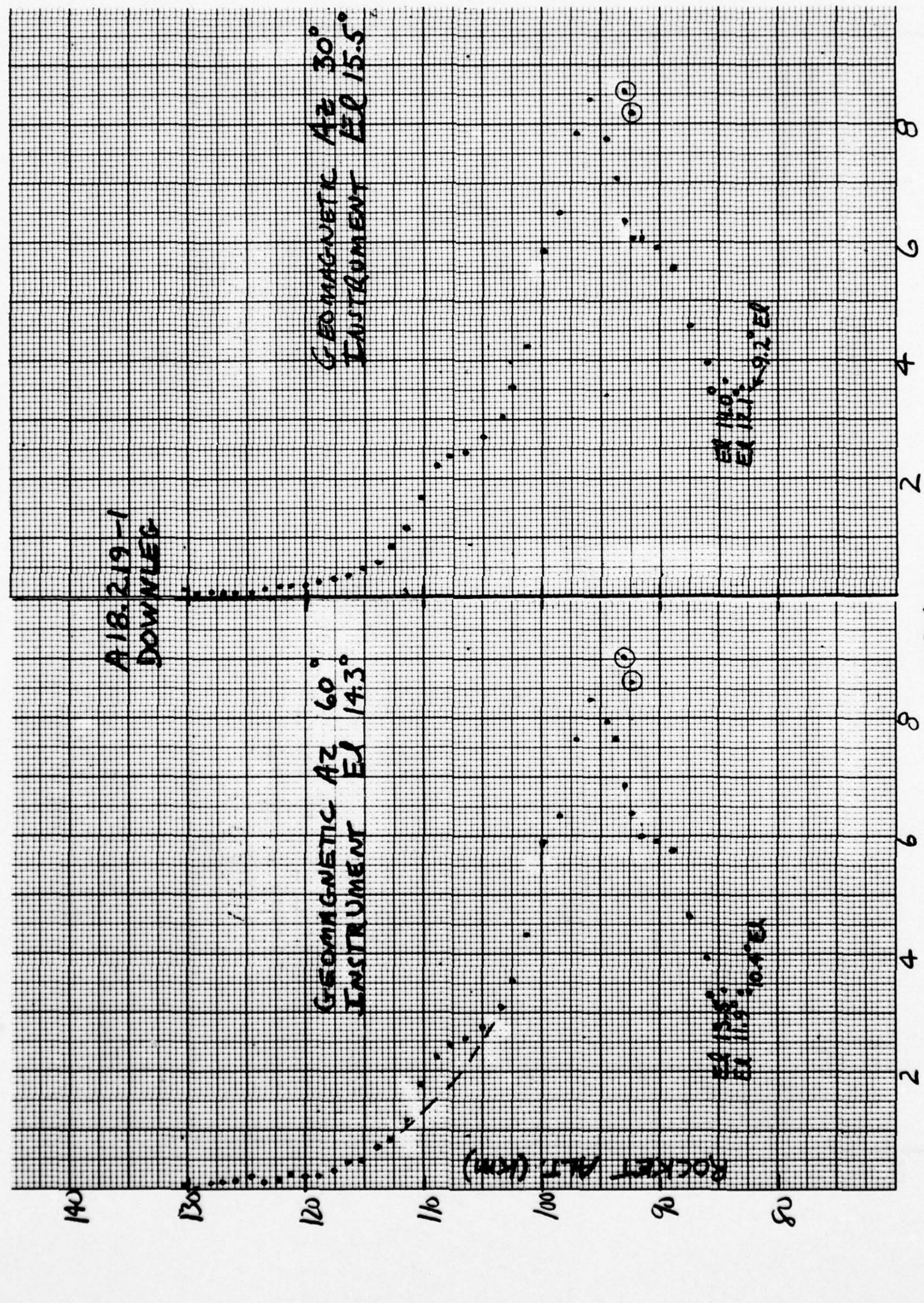
A18.219-1
DOWNLEG
GEOMAGNETIC Az 60°
INSTRUMENT El 14.3°
GEOMAGNETIC Az 30°
INSTRUMENT El 15.5°
ROCKET ALT (KM)
140
130
120
110
100
90
80
2
4
6
8
6(k)
6(l)
MR 4.3 μm

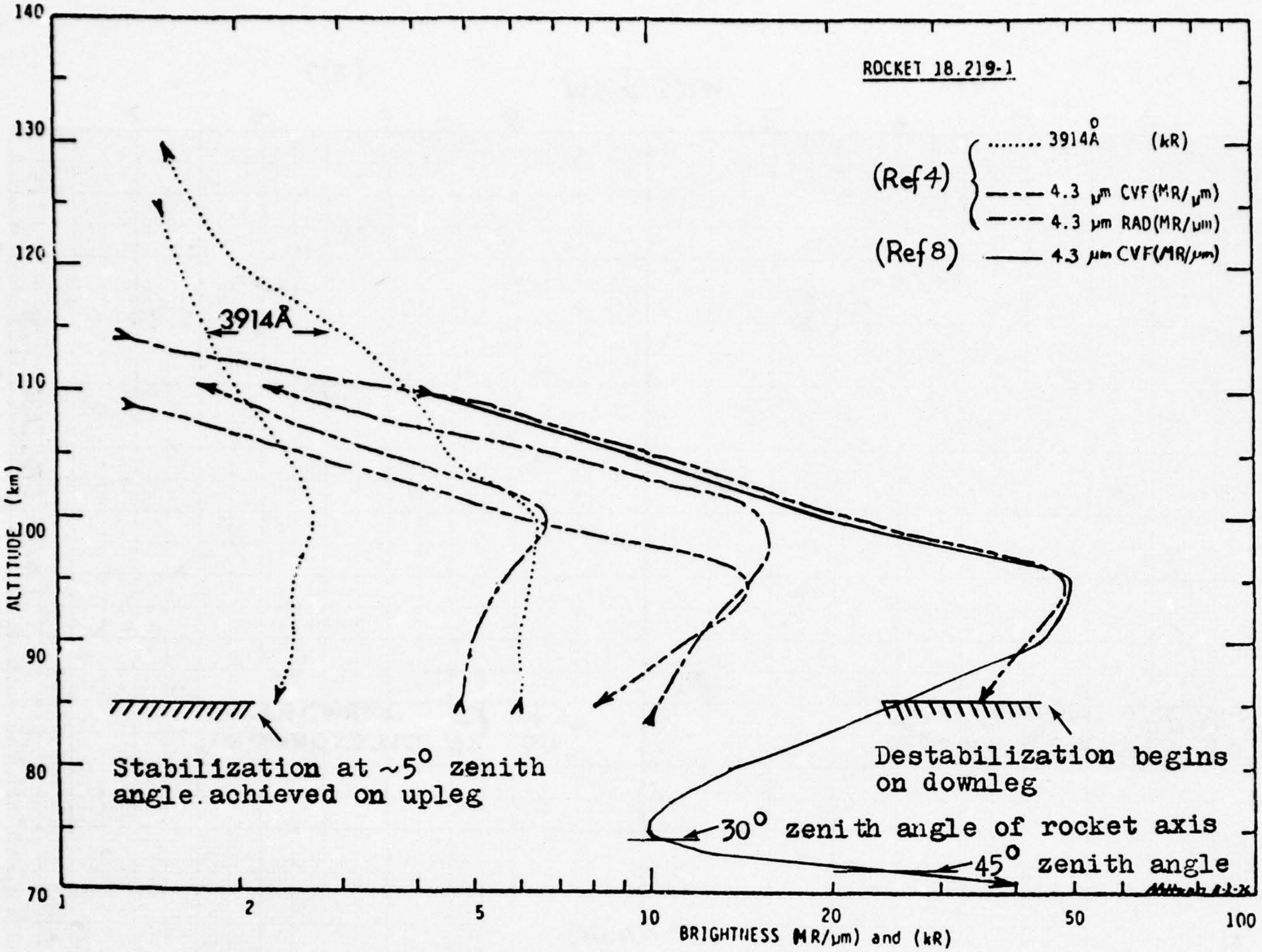

Figure 7. Near-zenith altitude profiles of 4.3μm and 3914 Å radiance measured by the axial-pointing instruments on upleg and downleg of A18.219-1.

Our earlier characterization of the auroral ionosphere for the 25 Feb 1974 flight (Appendix VII of Ref 2, and Section II of Ref 3; refer in particular to the all-sky views from PKR and FYU, Fig 55 of Ref 3) shows a complex system of arcs, with particle precipitation both south and north of the rocket during the downleg data period of Fig 6 (342-380 sec). The northward vector component of the rocket's velocity was about $\frac{1}{4}$ km/sec, and its trajectory lay very close to the 13^{o}-inclined geomagnetic field lines. The most intense arc (in the projection from PKR), whose field lines recrossed the rocket when it was at 180 km on downleg, had a phase velocity of ~1 km/sec N; when the rocket was at 100 km (360 sec) the S "edge" of this brightest auroral region lay ~75 km N of the radiometer. A second broad arc had intensified further to the N by this time (Fig 42 of Ref 3). The arc to the S of the rocket was weak along the PKR-FYU meridian and bright towards the W, as is described in more detail in Section II where the immediate and earlier dosing of the atmosphere is further reviewed. A semi-quantitative plot from the meridian scanning photometer (p417 of Ref 4) depicts with moderate resolution the predosing of the air in the vicinity of the rocket. As both Fig 6f-i and 7 show, the 4.3μm levels near peak radiance are at least a factor 2 higher on downleg than on upleg (a matter discussed in the presentation starting on p304 of Ref 4).

The restricted range of altitudes and azimuths in which fluorescence-related increases in 4.3μm-band radiance (whose implications are discussed in Section II) are observed, is indicated in Fig 6. The data from the sidelooking 4.3μm radiometer otherwise show no obvious correlation with the instantaneous energy deposition by charged particles that produce the optical aurora, example profiles of which are in Fig 8. 4.3μm-band profiles for the lowest, second highest, and one intermediate elevation angle in Fig 8 indicate that the altitude at which radiance is a maximum decreases by about 1 km between 15^{o} and 5^{o} $e\ell$ in the predosed auroral atmosphere. Over this range of elevation angles the column concentration of CO_2 molecules in the radiometer's

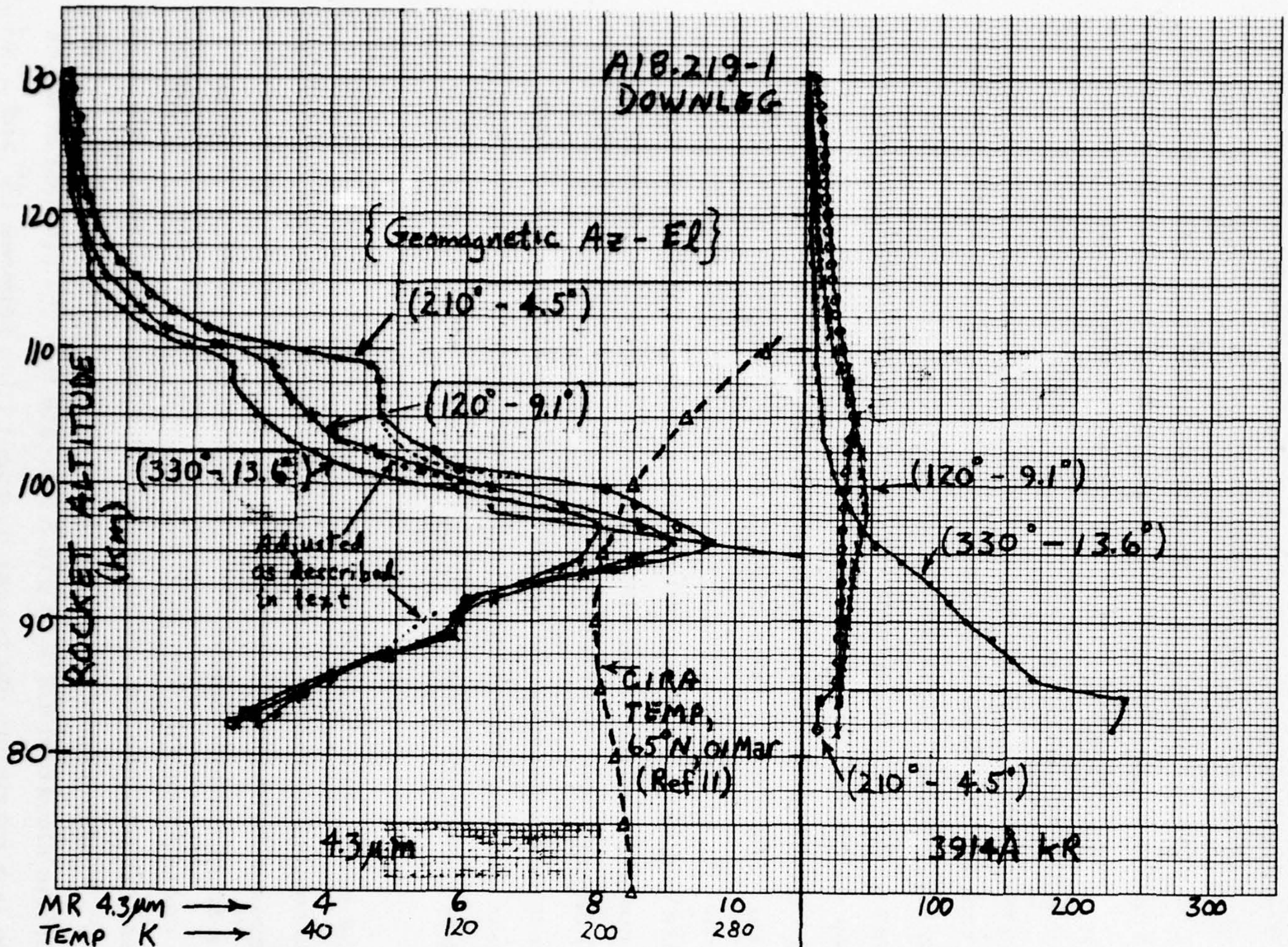

Figure 8. Altitude profiles of 4.3μm and 3914 Å radiance at three azimuths-elevations, A18.219-1 downleg. The dotted 4.3μm profiles near $5\frac{1}{2}$ MR apply the adjustment described in the text.

field of view changes by about a factor $2\frac{1}{2}$, applying "density" profile model F in Ref 9. The downleg altitude profiles in Fig 6 and 8 also show two subsidiary layers at all azimuths-elevations, which are discussed in the next subsection.

The two data points near $92\frac{1}{2}$ km (circled on Fig 6) lie $\sim 2\frac{1}{2}$ MR above the interpolated profiles at all azimuths. The radiance increase (Fig 9) starts at 371.88 sec and persists for closely two rocket spin cycles (1.03 sec) before decreasing to near its previous level over the same azimuth range as its increase, $\sim 11^{\circ}$ (0.015 sec). An increase of substantially greater absolute magnitude appears simultaneously in the data from the 2.8μm segment of A18.219-1's dual radiometer. Since similar level shifts are present in the telemetry from both radiometers at fixed intervals throughout the flight, we ascribe them to a calibration signal additively superposed on that produced by the scene radiances. Specifically, these 1 sec-duration step increases occur regularly at 34.3 sec intervals beginning at 97.48 sec, and average 2 MR above the local 4.3μm radiance. (Radiometers and photometers on earlier multi-instrumented rockets were document as fitted with internal light-emitting diodes which were periodically activated to provide an inflight measure of relative system responsivity, p 37 of Ref 10; the excess signals from A18.219-1 are in all probability due to this source.) Taking into account the height of the step increase in Fig 9 and the next az-ℓ scan (Spin 734), we have reduced the 4.3μm altitude profile readings by 2.2 MR between 371.88 and 372.91 sec (93 and 92 km in Fig 6).

A18.219-1's 4.3μm filter radiometer was a refurbishment of the 5.3μm radiometer recovered from the 1973 multi payload (A18.205-1). The response characteristic for the latter instrument had a sharp change in slope near 2.71 telemetry volts (Ref 10). The data printout lists both received TM voltages and the 4.3μm radiances they are assigned by computer in the ground-reconstruction process. It shows that the 1974 version's break point was at 2.78 TM volts, 5.9 MR,

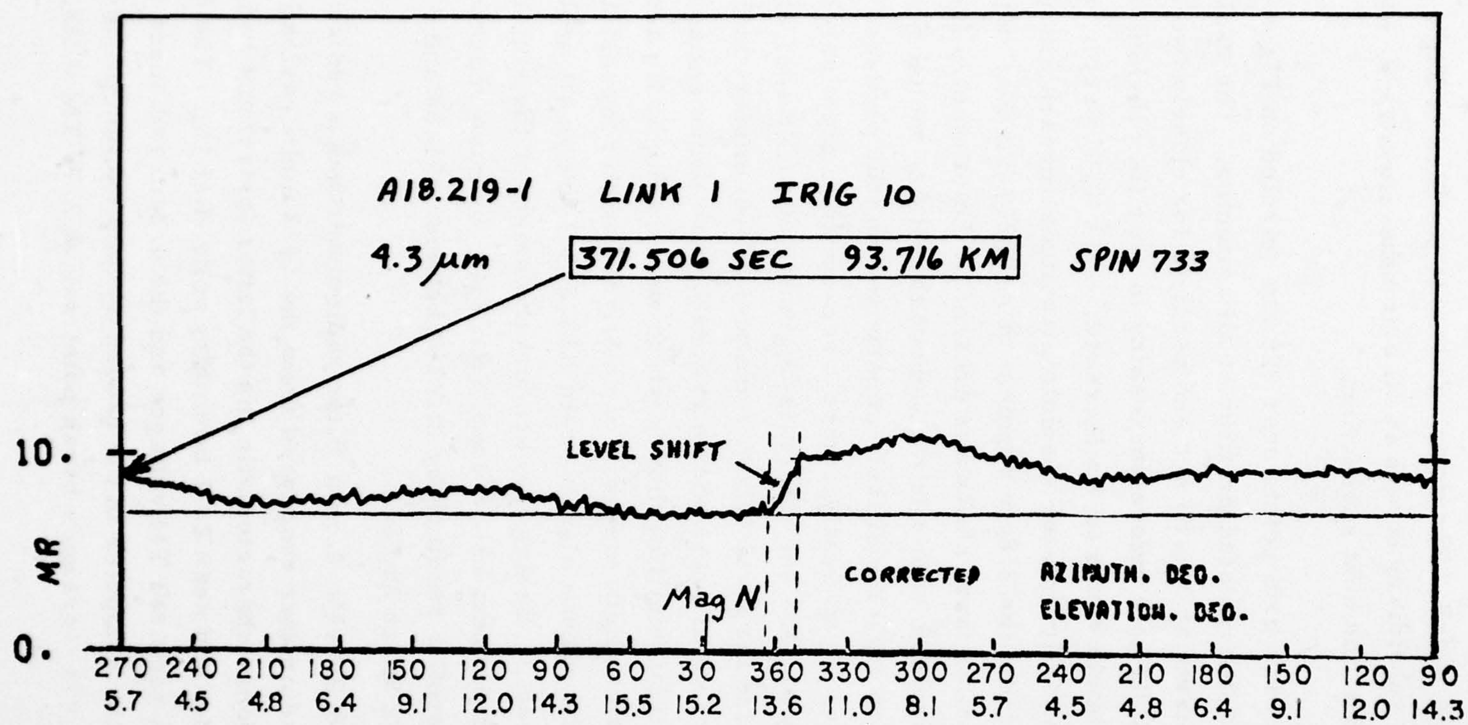

Figure 9. 4.3μm az-el radiance distribution on downleg spin cycle 733 of A18.219-1, showing the sharp discontinuity starting at 371.88 sec.

above which the slope of the characteristic decreases by a factor 9 (Fig 10). The radiometer's input-output response characteristic - scene radiance (converted to amplified photocurrent) to this same TM voltage - appears to lie above that used in the reconstruction below the break point (at least), as is evidenced by the presence of sections of radiance lying very close to 5.9 MR. The seven circles in Fig 10 were located by interpolating in Spin 723 ($100\frac{1}{2}$ km) between radiances transferred above the minimum of the low-sensitivity segment of the characteristic and those below the maximum of the high-sensitivity segment, which reproduce as "flat" over two $\sim 80^{\circ}$-azimuth ranges. (That is, we faired together 4.3μm radiances between 4-5 and 6-9 MR regions, whose reproduction is self-consistent; and plotted the interpolated radiances against TM voltage.) The effect of this imperfection in the instrument's data transfer characteristic is to reduce 5-6 MR radiances by $\sim\frac{1}{2}$ MR (see Fig 10). Self-consistency of the reconstructed 4.3μm-band data in other radiance ranges, to which this interpolation-correction procedure cannot be applied, does not of course imply that no further systematic error is present.

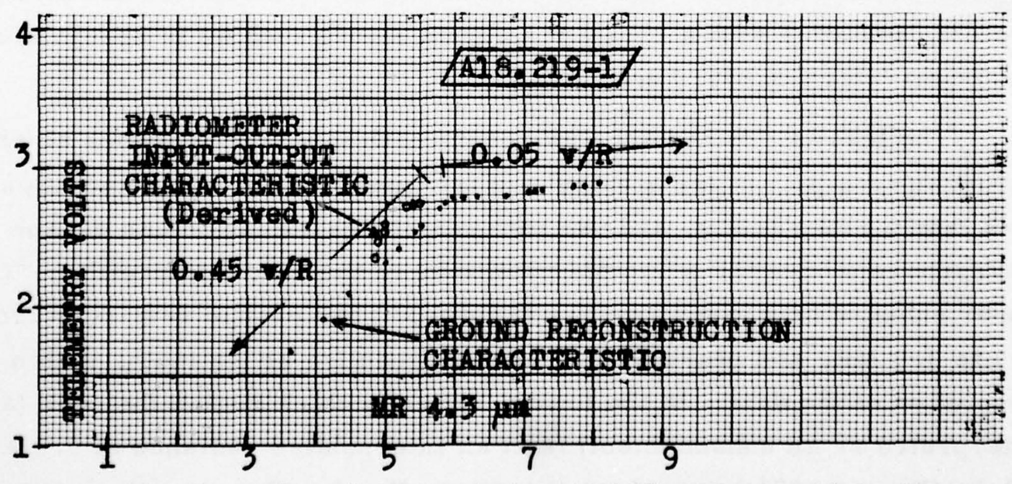

Figure 10. Transfer characteristics of A18.219-1's sidelooking 4.3μm radiometer as determined from the data printout in the time period 365.4 to 368.5 sec, and interpolated from Spin 723 where the radiances lie on both sides of the break point.

LAYERING OF THE RADIANCE PROFILES

The altitude profiles indicate layering of the radiation density both above and below the main peak near 96 km. If these irregularities are interpreted as enhancements, the upper one maximizes at $109 \pm \frac{1}{2}$ km at all azimuths, and the less well-resolved lower subsidiary peak at $88\frac{1}{2} \pm \frac{1}{2}$ km. This radiance structure is not correlated with prompt air fluorescence in the radiometer's field of view, as the representative comparison profiles in Fig 8 show.

Fig 11 is a plot of the upper layer's "excess" 4.3μm radiances above a manually interpolated baseline (dashed lines in Fig 6a for example) as a function of pointing azimuth. The enhancement is discernible above the small fluctuations in radiance in the altitude range at least 111 to 106 km at all azimuth angles. It is highest toward the SW (near 210°) where the elevation angle reaches its minimum and the interpolated sky radiance is a maximum. In Fig 12 are plotted profiles of the <u>fractional</u> increase above this interpolated intensity. The variability of these fractional changes indicates that they are probably not due to a slow change in sensitivity of the radiometer system; for example, at the peak the fraction varies between 0.35 and 0.65. In addition the increases are not consistent with a constant additive signal such as is observed at 92-93 km (starting 371.9 sec, Fig 7).

The layering of radiant flux occurs both in altitude regions at which the mean free path of the atmosphere for (most) 4.3μm CO_2 radiation is less than a scale height, and where much of this radiation can escape the atmosphere (above the principal maximum in the radiance profile). The upper enhancement layer appears at interpolated-profile radiances from 1.5 to 3.0 MR, and peaks at the same altitude for all azimuths within the resolution of the data. In the lower, optically thick region the peak (again interpreted as an enhancement) is at an interpolated radiance of $5.2 \pm \sim 0.2$ MR, near $88\frac{1}{2}$ km rocket altitude at all azimuths-elevations (as best as can be determined).

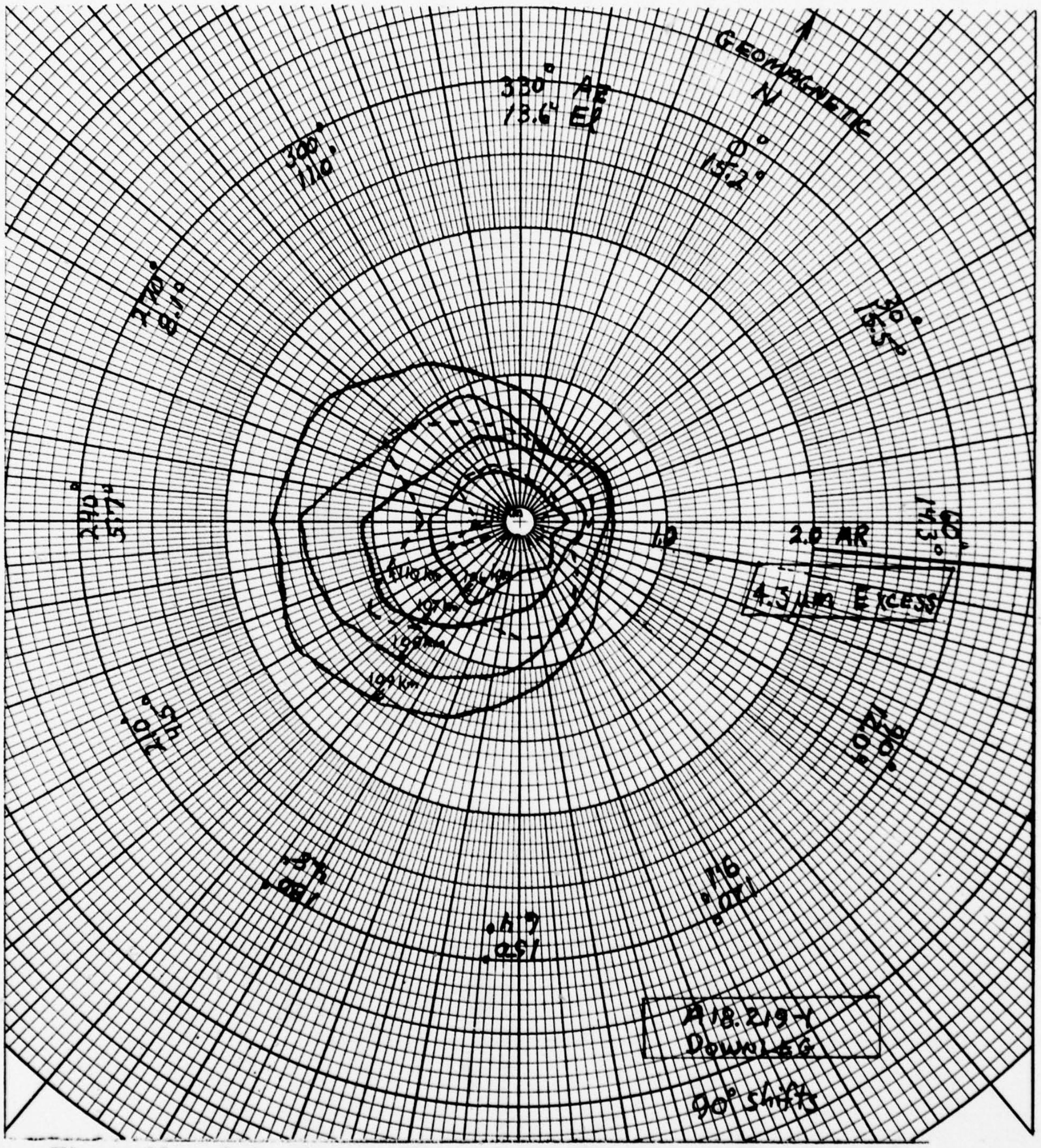

Figure 11. Azimuth dependence of excess 4.3μm signal above an interpolated altitude profile between 106 and 111 km rocket altitude (see text), A18.219-1 downleg.

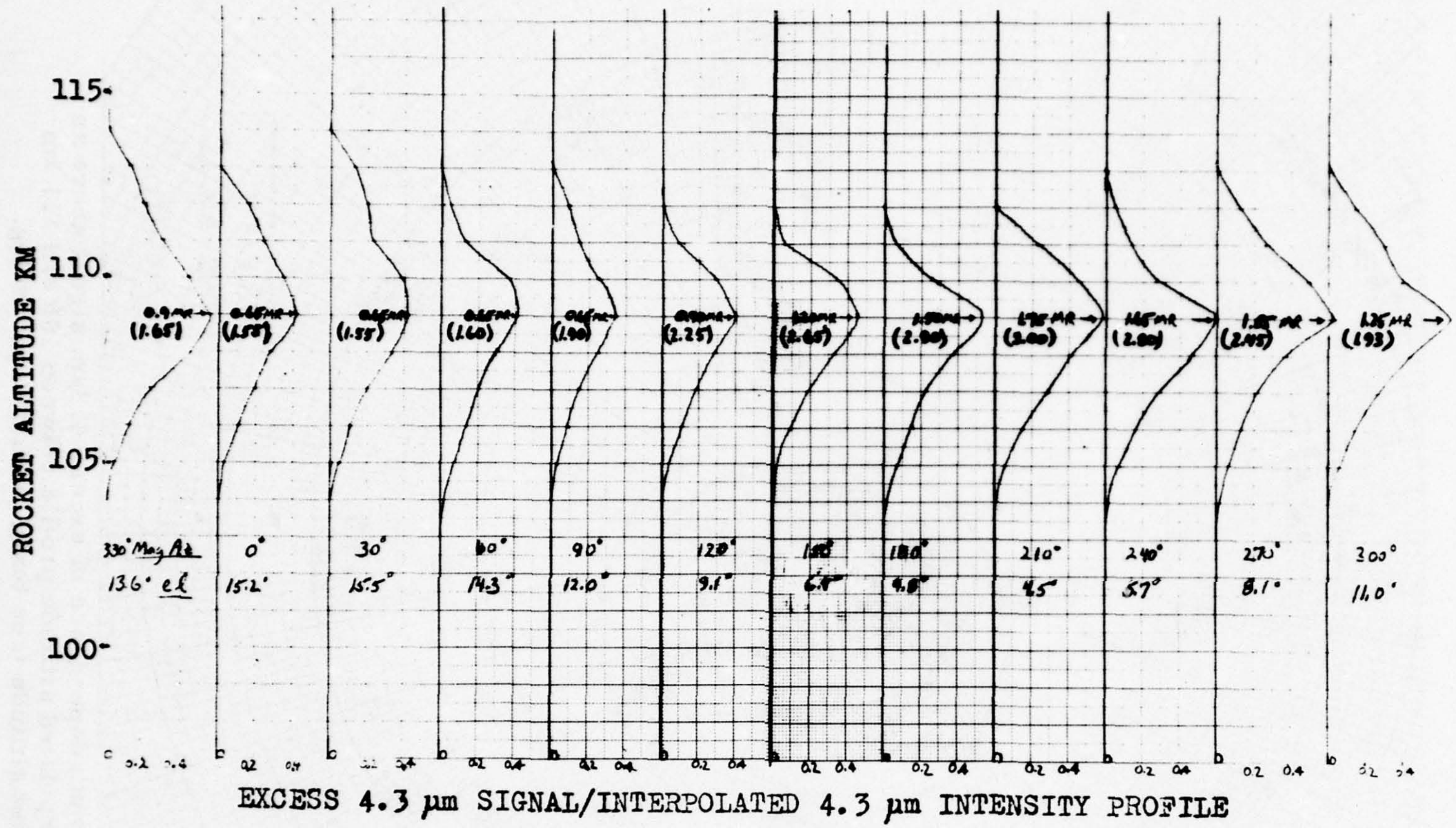

Figure 12. Altitude profiles of the fractional increase above an interpolated 4.3µm intensity profile near 109 km rocket altitude, A18.219-1 downleg. The numbers in parentheses are the baseline intensities at the peaks.

THIS PAGE IS BEST QUALITY PRACTICABLE
FROM COPY FURNISHED TO DDC

The upleg altitude profiles (Fig's 6f, i) give some hint of a high altitude (~106 km) layering similar to that observed in the downleg profiles. Estimated peak excess above an interpolated radiance profile is 0.3 MR above $2\frac{1}{4}$ MR, a ratio substantially less than those in the more heavily predosed air volumes shown in Fig 12. We are at present investigating the upleg 4.3μm-radiance data at other azimuths for further evidence of irregularities.

The extent to which this layering of radiation density could be an effect of error in transfer-telemetry of data from the rocket radiometer can be in part determined from the characteristics in Fig 10. The warp in the altitude profiles above the principal peak near 96 km lies at levels too far below the break point to be ascribed to this source. The lower layer might be interpreted as a local maximum lying below the break point, or a minimum above it; see in particular Fig 8. Thus the departure from smoothness of the profile below 96 km could be caused either by the aforementioned $\sim\frac{1}{2}$ MR offset in the instrument's transfer characteristic below 5.9 MR, or by a defect in reproduction of radiances between ~6 and 9 MR.

Profiles to which are applied the interpolation-derived "correction" between ~5-6 MR from Fig 10 are included as dotted lines in Fig 8. Such an adjustment in effect removes the lower layering while deepening the profile irregularity above the main 4.3μm radiance maximum. The argument that the lower layer is an artifact is strengthened by the observation that the inflection in the profile always occurs in the same radiance range near the break point. However this radiance is in any case virtually constant with elevation angle near 89 km because the atmosphere has become optically thick to radiation in the 4.3μm filter band. (Refer to the plot in Fig 4; the "spread" at 88.8 km starting altitude is caused by the fluorescence-related signal discussed in Section II.)

Viewing in the zenith from above the main peak, the irregularity in radiation flux would have a lower signal/background ratio or "contrast." This could explain why it has not been detected in previous rocket experiments (and why it does not show clearly, if at all, in the data from the near zenith-viewing filter radiometer and circular variable filter spectrometer on A18.219-1, Fig 7). We have included for reference the kinetic temperature profile for the late winter sub-polar atmosphere (from Table 18a of Ref 11); the vibrational temperature of the CO_2 molecules is known to be out of equilibrium with this local temperature at altitudes where aurora-producing particles deposit their energy. The upper layering may be an effect of adding two sources of pumping of the upper state(s) of 4.2 - 4.3μm CO_2 emission, auroral-collisional (through $N_2^{\ddagger}$ and reabsorption of photons, Ref 5) and by absorption of principally-thermal atmospheric radiation. The lower amplitude of any irregularity in the more weakly-predosed upleg region is supportive of this hypothesis.

SECTION II

CORRELATED 4.3μm FEATURE NEAR GEOMAGNETIC WEST

NEAR-PROMPT 4.3μm EMISSION

Elevation-azimuth scans in the 4.3μm band on downleg of A18.219-1 show a weak feature at $\sim 290^{\circ}$ geographic azimuth that correlates with a narrow peak seen by the visible aurora-monitoring 3914 Å and 5577 Å photometers. This largely-unexpected excess emission, which was given preliminary notice in Ref 3 (p 102ff), is further evaluated and interpreted in this Section.

The feature initially appears on the 4.3μm signal as a small enhancement detectable in scans below approximately 102 km rocket altitude. Figure 13 shows the data from the spin starting at 102 km from the 4.3μm radiometer, along with the radiances measured at 2.8μm, 5577 Å, and 3914 Å. Figure 14 is a detail of the region near 290° (260° geomagnetic) at 4.3μm and 3914 Å, along with plots of the angular responses of the two instruments. This feature at 4.3μm is <u>not</u> associated with the change in the radiometer's transfer characteristic at radiant intensities near 5.9 MR (explained in Section I).

Figure 15 compares the 4.3μm radiance distributions at several downleg altitudes down to 92.3 km with the 3914 Å distributions. The peak at 4.3μm aligns very closely with that at 3914 Å. However, the 4.3μm peak at the lower altitudes – not discussed in our preliminary review – has broadened considerably.

CORRELATION WITH ALL-SKY AND MERIDIAN SCANNING PHOTOMETER DATA

The excess emission appears near 260° geomagnetic azimuth, or 10° south of geomagnetic west. The strong, narrow enhancement in the 3914 Å data can be explained qualitatively from the all-sky camera photographs taken from Fort Yukon and Ester Dome (Fig 16 and Ref 3, p110) in combination with the meridian-plane radiance distribution measured by the scanning photometer at Poker Flat.

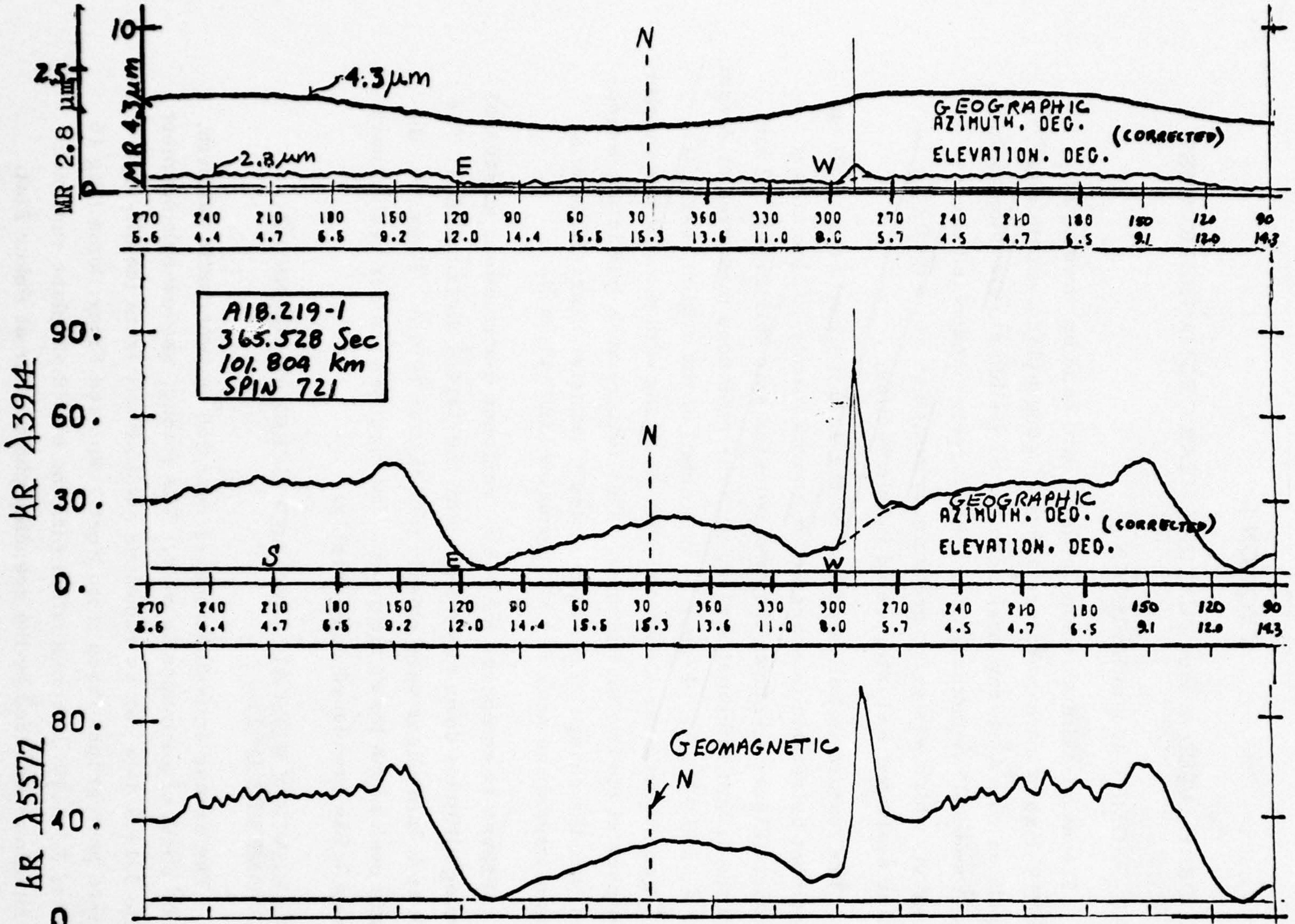

Figure 13. A comparison between 3914 Å, 5577 Å, 2.8μm, and 4.3μm for Spin 721 on downleg of A18.219-1. The scales have been corrected in elevation and azimuth for a 90° shift (Section I).

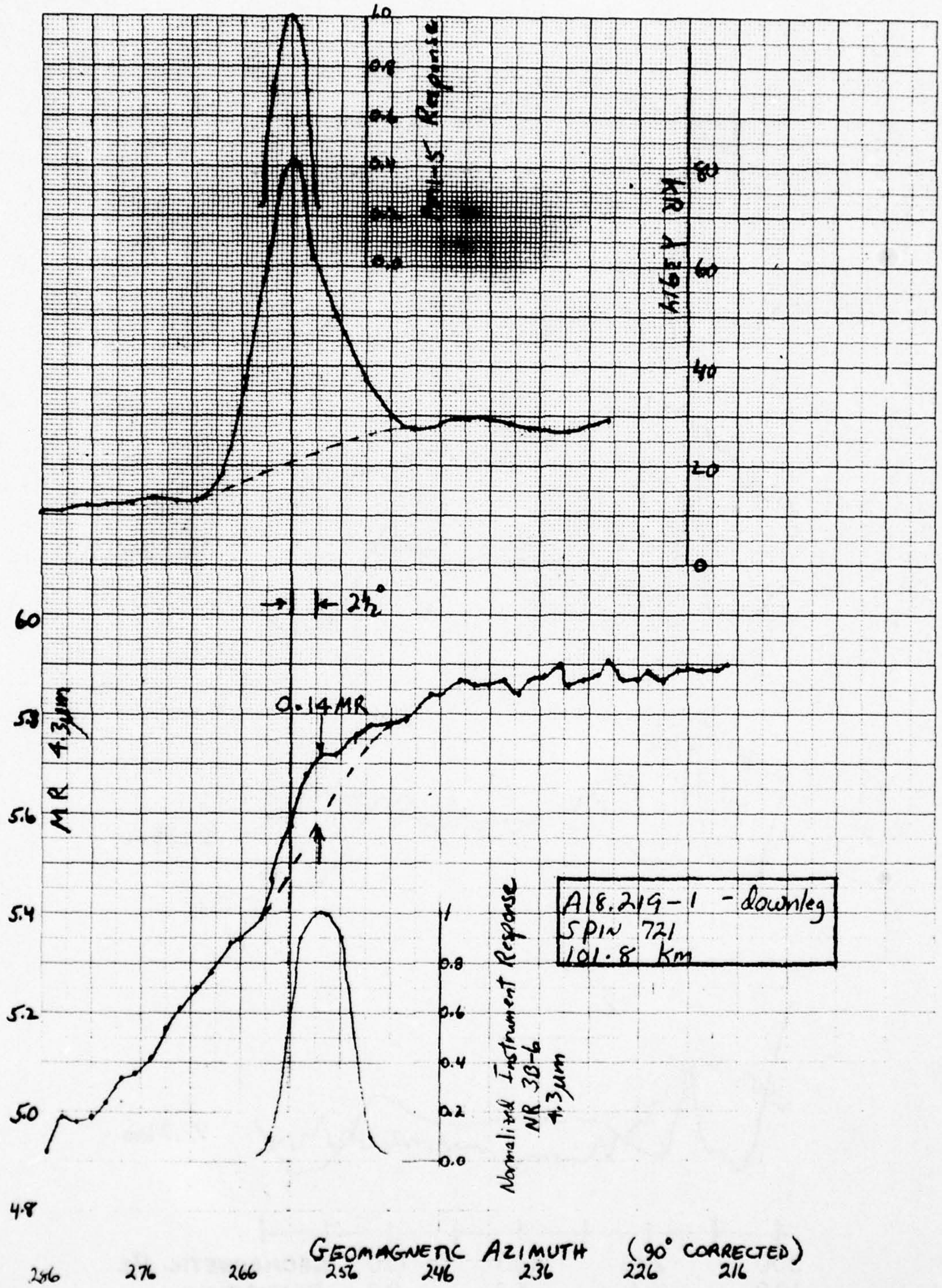

Figure 14. Detail of region near 260° geomagnetic azimuth for Spin 721 on downleg of A18.219-1 showing the correlation between 3914 Å and the 4.3μm "bump." Also shown are the angular response functions of the two instruments.

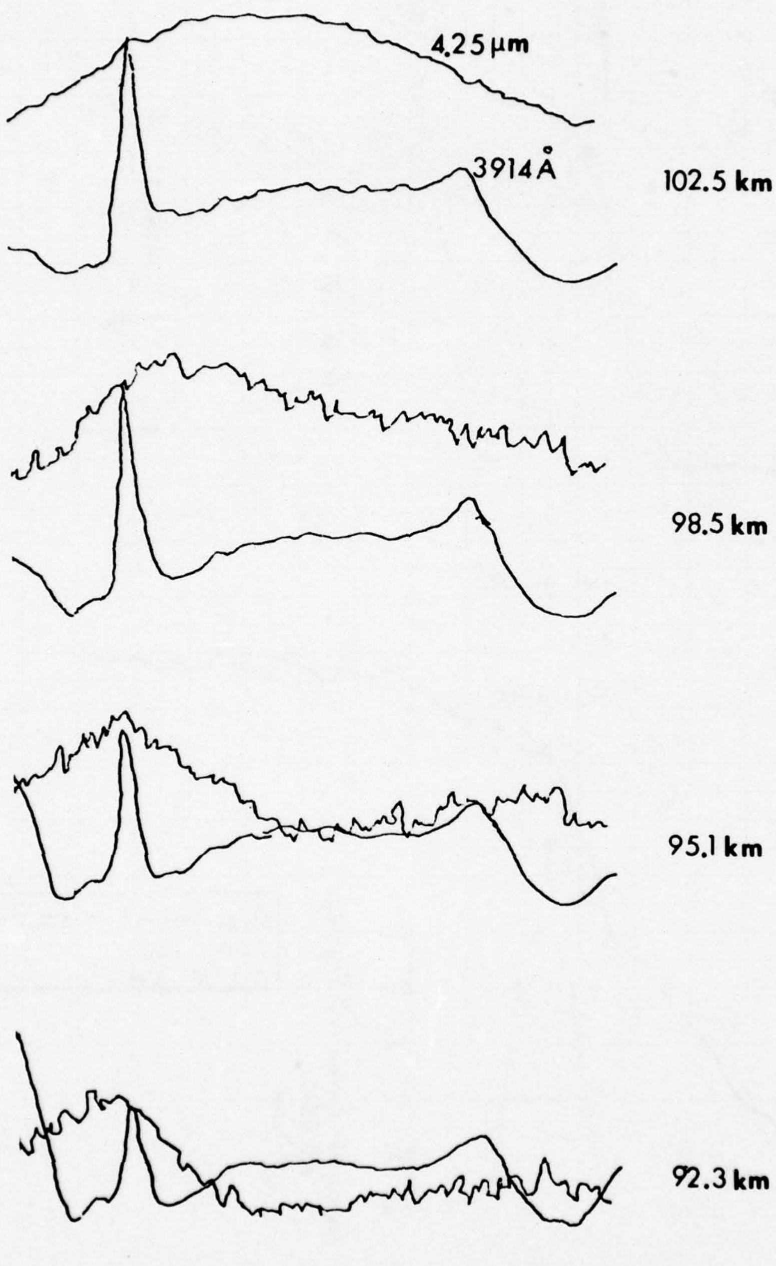

Figure 15. Comparison between 3914 Å and 4.3μm radiances for the region near 260° geomagnetic azimuth at various altitudes on downleg of A18.219-1.

When the rocket was at 100 km altitude (360 sec after launch) on downleg, it is 40° north of the zenith as viewed from Poker Flat and about 45° south of the zenith as viewed from Fort Yukon. The Poker Flat meridian scanning photometer (Fig 16) shows an intense region with three peaks running from about 45° north of its zenith to 85° north, with the peaks centered at 60°, 70°, and 80° north. There is also a weak arc (as viewed by the MSP) which is centered at 30° north of the zenith. These features are consistent with the all-sky views. The position of the rocket is also shown in the all-sky photograph at about 75 km south of the center of the first of three northern arcs and about 30 km north of the center of the arc to the south of it. Looking again at Fig 13, when the geomagnetic azimuth of the rocket photometers is to the north, the photometer elevation is approximately 15°, while when it is to the south the elevation is 5°. Projecting the look angles into the near-vertical planes containing the two arcs under discussion yields intercepts at 118 km altitude for the first arc to the north and 102 km altitude in the arc to the south when the rocket is at 100 km altitude downleg). The projection into the two additional arcs to the north is at much higher altitudes. This explains why the visible radiances toward the south appear much more intense than those to the north in Fig 13, since the intercept of the photometer field on the near-vertical plane to the north is well above the altitude of peak emission rates. Similar azimuthal scans taken at lower altitudes show the intensity to the north rising rapidly as the photometer intersection moves closer to the altitude of peak emission, while the intensity to the south decreases slowly as it moves below the altitude of peak emission.

The sharp feature at the western edge of the southern scan (260° geomagnetic) in the 3914 Å and 5577 Å channels of Fig 13 is explained primarily by the usual east-west enhancement seen as fields line up with the direction of the arc to the south. This enhancement is higher to the west due to the bright region which is observable in the all-sky photograph (Fig 16) to the southwest, and also because the elevation

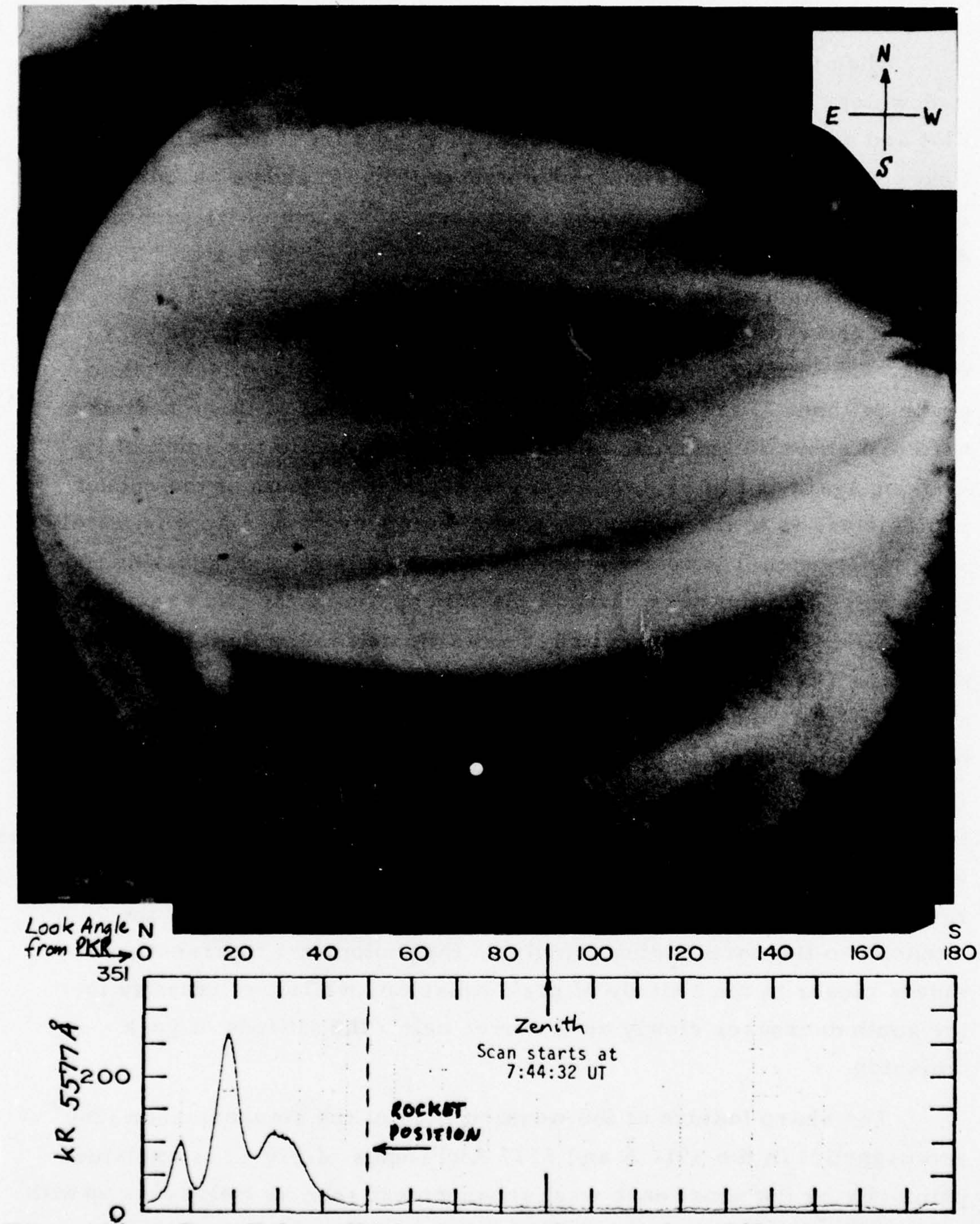

Figure 16. Fort Yukon all-sky camera photograph at 368 seconds after launch of A18. 219-1 with the position of the rocket (●) indicated. Also shown is the Poker Flat meridian scanning photometer data at 362 seconds, with the rocket position noted (scan from Ref 3's Reference 11).

angle is lower to the west. The general east-west characteristic enhancement agrees with enhancements seen in earlier flights (Ref 3, Fig 15) of sidelooking narrow-angle photometers.

CORRELATION WITH 5199 Å PHOTOMETER DATA

Fig 17 shows a scan from the wider 5199 Å channel taken at 118 km downleg compared with a scan from the 4.3μm channel taken at 94 km. It can be seen that the broadened emission feature in the 4.3μm channel centered around geomagnetic west correlates in angle extremely well with a broad feature on the 5199 Å channel at the higher altitude. The 3914 Å and 5577 Å radiances do not demonstrate this broad feature. The intensity observed in the narrow (10 Å) 5199 Å channel near 118 km is approximately 0.17 kR above background. Since the 3914 Å channel shows little change over much of the feature at this altitude, we can assume that the excess above background is primarily due to N^2D emission, as discussed in Section IV. This is consistent with the apparent higher altitude production of N^2D, since 3914 Å would be seen to peak at much lower altitude. Indeed, 3914 Å does show a slight indication of a broad feature in this angular region at the lower altitude, upon which the sharp feature is superimposed.

DISCUSSION OF SOURCES OF 4.3μm EMISSIONS

The bulk of the signal observed in the 4.3μm channel is almost certainly due to radiation by CO_2 excited by resonance transfer from vibrationally excited nitrogen, as discussed in Section I. However, the enhancement at 260° azimuth above the smoothly varying background at the higher altitudes (102 km) is quite sharply defined in azimuth, having an angular spread comparable to the angular response of the photometer. This would indicate, at least for the region viewed at a rocket altitude of 102 km, that the reaction causing the observed radiation must be realtively "prompt" in order to maintain its strong correlation with the 3914 Å fluorescence emission.

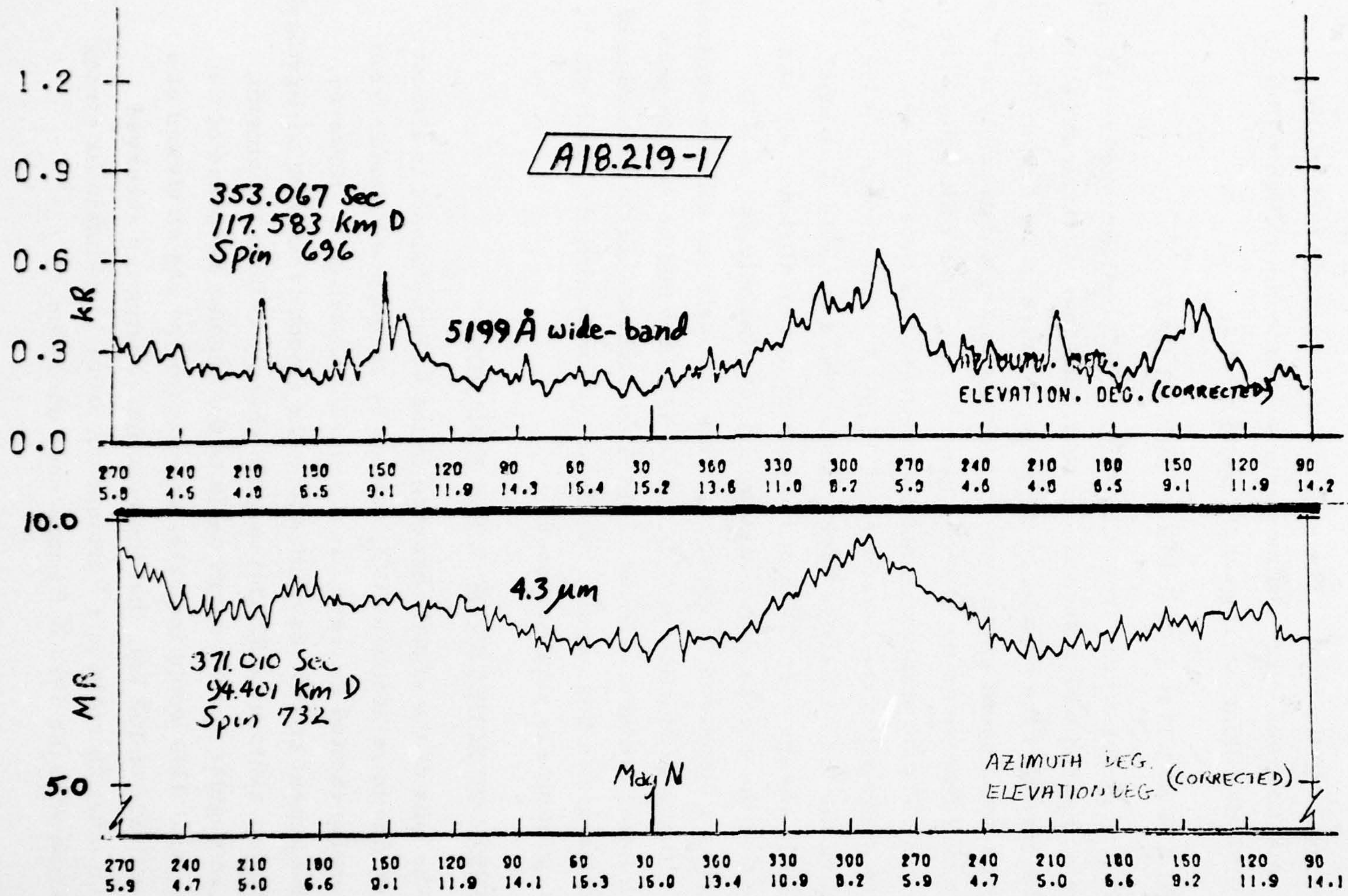

Figure 17. Comparison between the 5199 Å channel at 118 km and the 4.3μm channel at 94 km on downleg of A18.219-1.

The broadened feature at the lower altitudes in the 4.3μm channel may perhaps be explained as due to rather lengthy predosing by exciting particles that have the apparent angular extent exhibited by the higher altitude N^2D as seen in the 5200 Å channel. This predosing, perhaps with some diffusive broadening, would start the reaction chain that leads to the 4.3μm emission feature which peaks near 94 km rocket altitude.

There are at least three potential candidate reactions to explain the prompt sharp 4.3μm feature at the higher altitude. These are (Ref 3) radiation from excited NO^+, radiation from the excited isotopic molecule $N^{14}N^{15}$, and direct production of excited CO_2 by electrons. Fig 18 illustrates the emission spectra related to these various possible contributors. The figure also shows the passband of the radiometer. It can be seen that there is some sensitivity to all three emissions, with the lowest sensitivity to the equally populated model of NO^+ and to the $N^{14}N^{15}$ (1, 0) band radiation.

From Fig 14, the signal seen in the 4.3μm channel at 260° geomagnetic west has an excess of approximately 140 kR over the expected level assuming an effect due to elevation angle only. It is possible to make some estimates for the efficiency for producing 4.3μm radiation through each of the three production channels indicated by making certain simplifying assumptions.

If we assume the prompt feature is due to radiation from NO^+, by referring to Fig 18 we can calculate the detection efficiency by examining the overlap of the instrument spectral response with the NO^+ spectral characteristics. The instrument function overlaps about 40% of the spectral energy of the NO^+ emission if the (1, 0) model is used and only about 15% of the emission if the (v = 0 - 10) equal population model is used. Applying these factors yields corrected values of 0.35 MR and 0.95 MR respectively for the two models. The intensity in the 3914 Å peak at this time is approximately 70 kR. This yields approximately 5 photons at 4.3μm per 3914 Å photon, assuming the (1, 0) model and approximately 14 photons per 3914 Å photon assuming

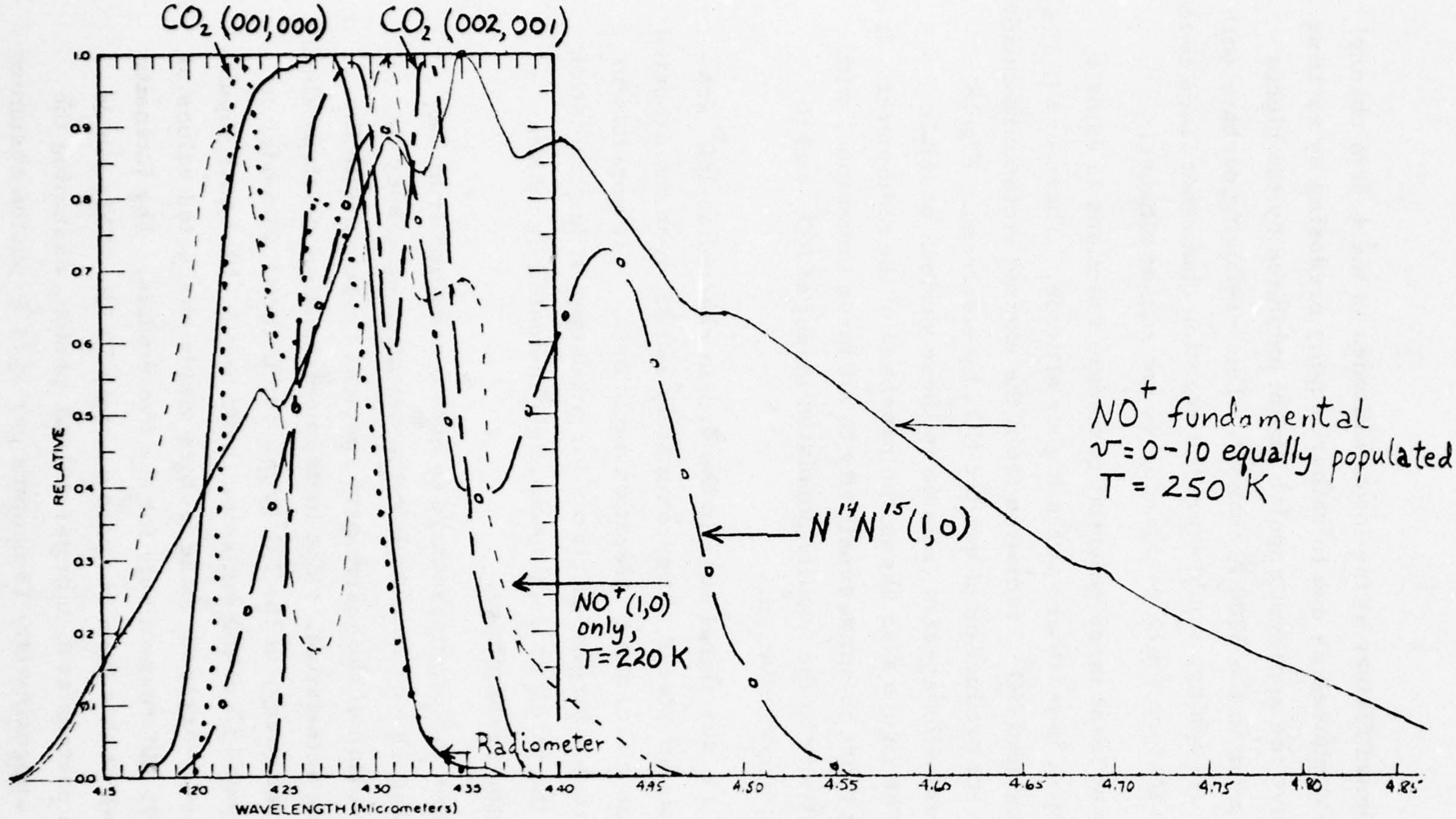

Figure 18. Emission spectra calculated and approximated for the fundamental of NO^+ with equal populations of v = 0 - 10 and NO^+ (1, 0) only, CO_2 for the (001, 000) and (002, 001) transitions, and the $N^{14}N^{15}$ (1, 0) transition. Also shown is the spectral response characteristic of A18. 219-1's Sidelooking "4. 3μm" radiometer.

the (v = 10) equal population model. This yields effective fluorescent-chemiluminescent efficiencies of about 0.2% and 0.5% respectively (quenching is believed to be a factor at auroral particle-deposition altitudes), using a ~0.4% 3914 Å fluorescent efficiency (Section V of Ref 3).

If we assume that the observed prompt component is due to radiation in the (1, 0) band of $N^{14}N^{15}$, the convolution of the instrument response with the vibration-rotation spectrum yields a detection efficiency of approximately 30%. This, in turn, gives an $N^{14}N^{15}$ fluorescence(-vibraluminescence or -chemiluminescence) efficiency of approximately 0.25% for the volume viewed from 102 km rocket altitude under the auroral dosing conditions of A18.219-1 downleg. (Refer to pp 105-106 of Ref 3 for futher discussion of the $N^{14}N^{15}$ molecule's radiative properties.) We will forego a discussion of a prompt CO_2 component because of its uncertain mode of production.

CONCLUSION

The salient points of this discussion of the particle excitation-correlated 4.3μm features are the indication of a prompt component in several scans below 102 km and the very distinct correlation of a broadened feature at lower (94 km) rocket altitude, whose shape and relationship to 3914 Å-fluorescence are shown in Fig 15, with a similar broad feature in the 5199 Å photometer channels at higher (118 km) rocket altitude. This would appear to couple the N^2D production with whatever mechanism(s) produce the lower altitude 4.3μm feature. A more exhaustive assessment of the predosing west of the radiometer, with improved estimates of the range to the field lines and thus the altitude above the descending rocket, would better define the source of this 4.3μm radiation. The procedure for determining the spatial distribution of predosing is that described for the HIRIS spectrometer, in Section V (in addition, altitudes near the meridian can be determined from spectroscopic ratios, as noted in Section VI).

Future rocket investigations should include instruments - narrow-wavelength radiometers and/or spectrometers - to obtain high resolution spectral information between $4\mu m$ and $5\mu m$ in low-elevation angle scans (refer to Fig 18). Such instruments would in principle reach useful fluorescence-associated signal/CO_2 background ratios over broader azimuth ranges in the auroral particle-excited ionosphere. It would be cost-effective to point radiometers at several elevation angles from the same sounding rocket, better to assess the altitude distribution, and thus the quenching, of this component of the "$4.3\mu m$" emission. Because of the apparent connection to $[N^2D]$,a 5199 Å differential photometer should be among those aligned with the infrared spectro-radiometers' field. In addition directly-quantitative all-sky photography would improve measurment of the off-meridian predosing.

SECTION III

FILM RESPONSE PHOTOMETER, IC519.07-1B

FUNCTION

A photoelectric photometer designed (by AFGL/OPR staff) to have wavelength response matching that of calibrated photographic cameras that recorded the spatial radiance distributions of the persistent sky-glows excited by the Fishbowl (1962) high-altitude nuclear explosions, was coaligned with the sidelooking radiometers and photometers on ICECAP "multi" rocket IC519.07-1B. The purpose of this film response photometer (henceforth referred to as FRP) is to link the infrared emissions from auroral particle-stimulated air measured from the rocket to this existing body of optical photometry data, so as to allow the infrared sky backgrounds excited by nuclear particles to be scaled to the known visible backgrounds. An FRP,viewing in the zenith, will also be used in the forthcoming HAES-program measurements from an aircraft of the spatial and spectral distribution of radiation near 2.8μm from the auroral ionosphere. The purpose of this preliminary review of the sidelooking FRP data from the rocket flight is to evaluate and verify the performance of this "transferring" instrument in terms of the radiances measured by visible aurora-sensitive photometers that viewed the same volumes of particle-excited air.

INSTRUMENT CHARACTERISTICS

Fig 19 shows the relative spectral sensitivity of the FRP as realized and the design-goal characteristic for a combination of film and lens typical of that used in Fishbowl Project 8A.1 and 8A.2's cameras. The film is Eastman Kodak Tri-X Pan, and the lens is representative of the fast, short focus types effective for late-time photography of afterglows that cover wide angles of sky (for example the Nikkor 55mm f/1.2 as used with full-frame 35mm format). Since no correction was attempted for the wavelength dependence of Rayleigh

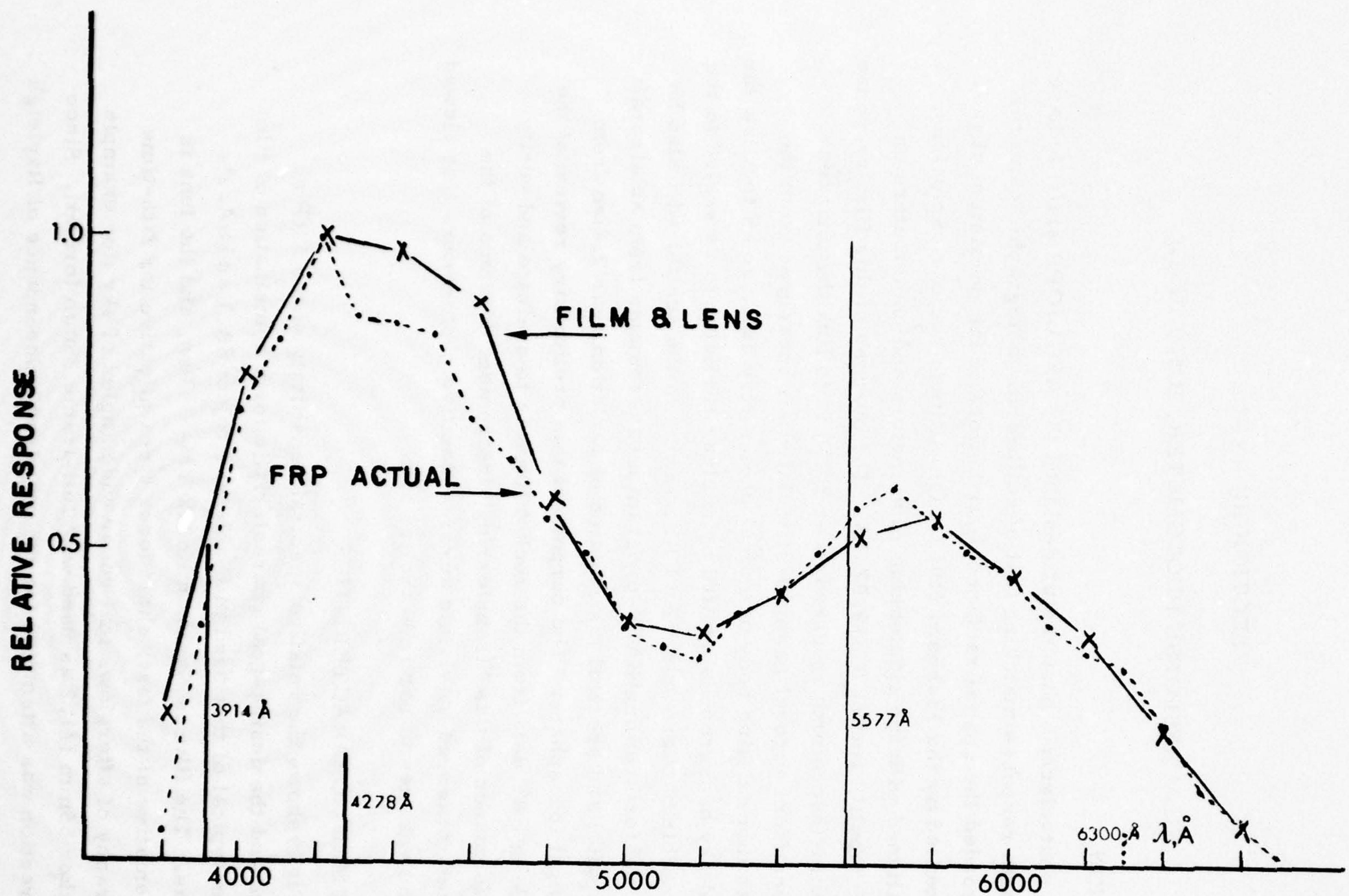

Figure 19. Relative photon response of the Film Response Photometer compared to that of Eastman Kodak Tri-X Pan film used with a fast wide-angle lens (see text). The vertical bars represent typical relative column intensities (as viewed from below) of the major auroral features in the FRP's wavelength range.

and Mie scattering of bomblight by the intervening lower atmosphere, which is in any case variable with elevation angle and meteorological conditions, The FRP's results apply best to the photography from KC-135 aircraft flying at ~35 kft. From this altitude the effects of outscattering are important only for narrow-angle radiating sources lying at low elevation angles.

The ordinate in Fig 19 is the relative output current from the photometer per unit monochromatic scene radiance (in photon units, for example Rayleighs per Å) at the wavelengths indicated on the abscissa. This characterization differs somewhat from that applied to photographic film, whose spectral sensitivity is expressed as the inverse of the monochromatic fluence that produces a given optical density after standard development, $(\mathrm{erg/cm^2}$ for D = 0.1 above fog, or for some fixed total density$)^{-1}$. There are, in addition, further differences between the response of the logarithmically-integrating photographic film and that of its simulating photoelectric detector.

ANTICIPATED RESPONSE OF THE FRP

Fig 19 also shows the approximate relative intensities of the brightest auroral features in the FRP's spectral range, viewing the excited volume from below. The OI green line is emitted from somewhat higher altitudes, and the strongly-quenched OI red doublet originates at considerably higher altitude than the N_2 and N_2^+ fluorescence bands; this effect is the basis for assessing the energy distribution of the incoming charged particles (Ref 12). Very roughly speaking, the column emission in the photographic-visible excited by auroral electrons having the typical characteristic energy 2-10 keV is about half in OI 5577 Å chemiluminescence-fluorescence photons and one quarter in impact-excited N_2^+ 3914 Å First Negative band photons, with all the other spectral features contributing the remaining one-quarter of the quanta over this wavelength range. The 5577 Å radiation lags the instantaneous energy deposition by ~ 1/2 sec, the actual time

dependence of emission varying in a complex way with altitude and time integral of ionization rate. In addition there is a weak persistent chemiluminescent continuum from the NO + O reaction, which results from predosing rather than the immediate local particle bombardment (Section IV).

This partial auroral spectrum leads to the expectation that the FRP's signal when the rocket is below most of the excited region would by and large follow that from the 5577 Å and 3914 Å photometers, in particular under intense auroral bombardment and at low zenith angles (for which the path length through the continuum-emitting layer is not excessively long). The correlation with 5577 Å emission would be better at higher rocket altitudes, and the 6300 - 6364 Å doublet provides an increasingly important contribution at very high rocket altitudes and large fluxes of soft electrons. We apply this rough model of the FRP's response to average aurora in our review of its performance.

ROCKET TRAJECTORY AND ORIENTATION

The location of the relatively diffuse auroral emission viewed by the rocket instruments is shown on the plot of the trajectory of IC519.07-1B (launched 0748:10, 12 Mar 75), Fig 20. A stable arc system formed near the PKR zenith before launch, and its central field line (indicated by + in Fig 20) remained south of the rocket during the measurement period; see the All-sky camera views in Fig 57 of Ref 3. The rocket was attitude-stabilized to only a few degrees, as the plot of the sidelooking instruments' altitude dependence of elevation angle shows (right side of Fig 22), so that in the magnetic meridian (for example) elevation varied between -0.5° and $+3.9^{\circ}$ over the flight. Therefore the altitude at which the fields-of-view of the FRP and its coaligned photometers and radiometers intercept the excited volume at a given look azimuth varies cyclically with the rocket's altitude. The rocket's spin rate was 1.4 rev's/sec, and the plane of its trajectory lay very close to the geometric meridian.

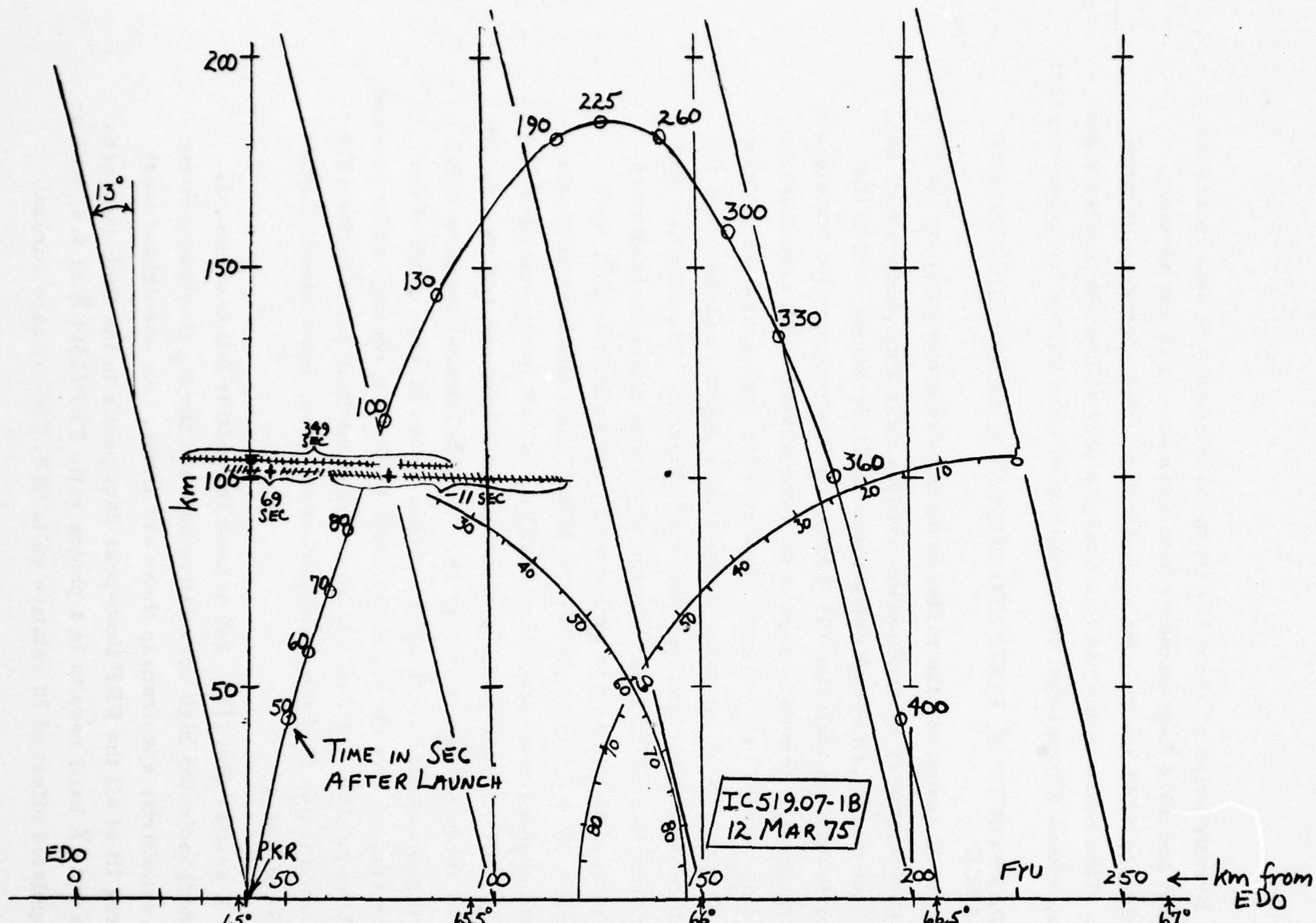

Figure 20. Trajectory of IC519. 07-1B with estimated location of the "center" (marked +) and north-south extent of the diffuse auroral arc. See also All-sky views in Fig 57 of Ref 3.

Erratic noise of about 100 Hz mean frequency is superposed on the FRP and 3914 Å-photometer data after about 115 km on upleg, extending to ~140 km on downleg and reappearing sporadically thereafter. This noise hampered this analysis only at low photometer signal levels, where it precluded determination of zero offsets due to dark current.

COMPARISON TO N_2^+ FIRST NEGATIVE (0,0) BAND FLUORESCENT RADIANCE

Fig 21 compares the radiance distributions measured by the FRP (high gain telemetry record) and the 3914 Å sidelooking photometer, over a 540° azimuth scan at one upleg rocket altitude below most of the aurorally-excited emission (93.4 km). In this presentation the signals from the two photometers appear well correlated, with even features extending only ~10° in azimuth reproduced in both scans; on the other hand the peak-to-valley ratio of the 3914 Å signal is higher, and the structure in the east limb is somewhat different. The familiar limb peaks from van Rhijn-type increase of column emission length are present at elevation angles as low as 3° and as high as 20°, with maximum 3914 Å brightness above 80 km (the altitude at which the rocket becomes near-stabilized) reaching 141 kR (west limb) and 76 kR (east limb). Altitude profiles of maximum brightness and its azimuth angle at these peaks are in Fig 22. Both brightness maxima move toward geomagnetic south as the rocket moves farther north of the diffuse arc, as was observed from the 1973 multi rocket, which crossed a stable arc (Fig 3 of Ref 3); in contrast the limb peaks of the 1974 arc, when it lies N of the multi rocket on upleg, move closer together (Fig 37 of Ref 3).

A scatter plot (Fig 23) of peak intensities (all backgrounds included) indicates high correlation between the N_2^+ fluorescence and FRP-sensitivity spectrum in these arc limbs. An unweighted least squares fit of all the FRP limb-peak data points to the limb radiances in the 3914 Å band results in a photon ratio FRP/3914 Å of 4.4, with an extrapolated offset of 78 relative units (RU) FRP at zero auroral

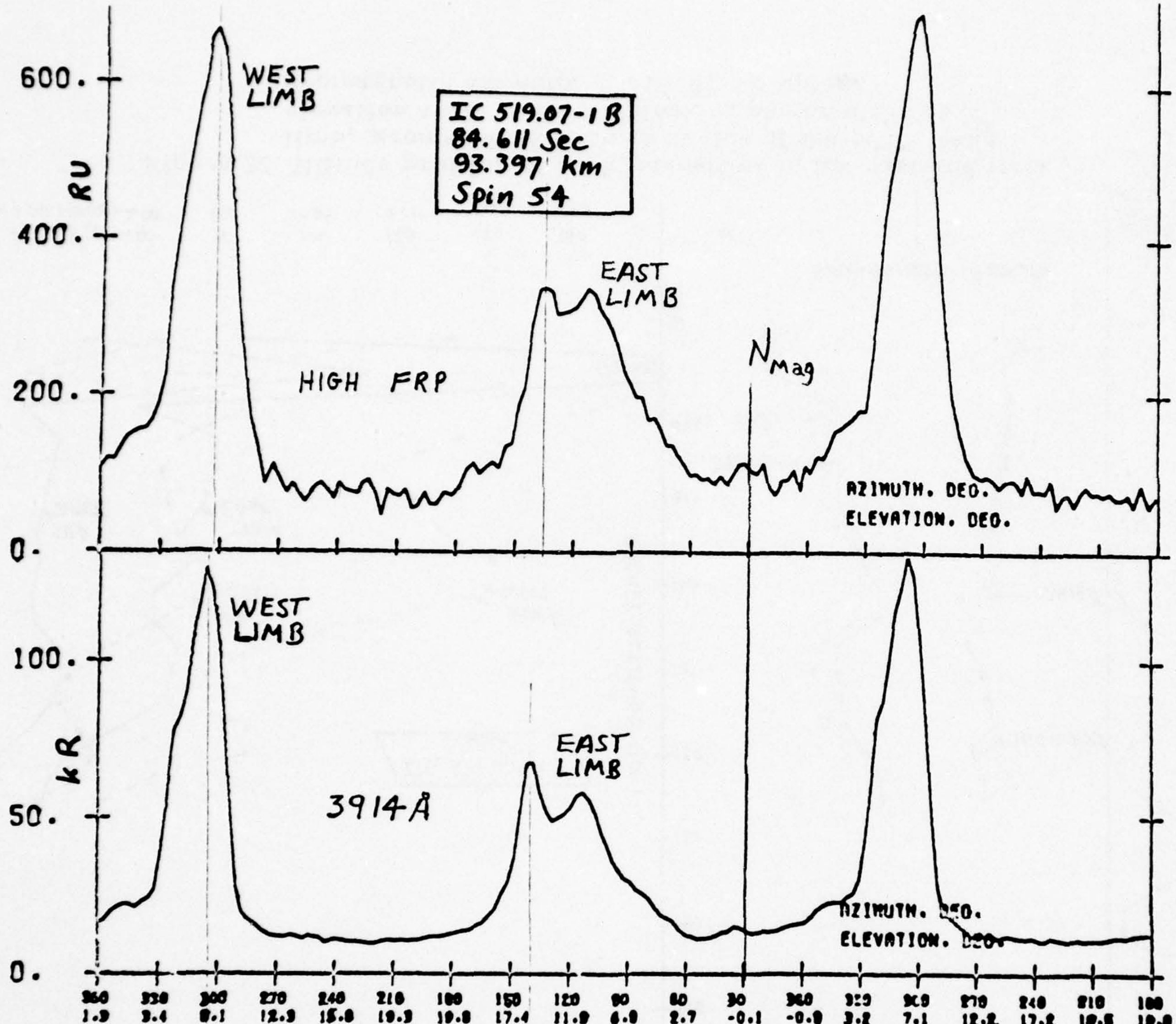

Figure 21. Representative 3914 Å and FRP elevation-azimuth scans from upleg of IC519.07-1B, showing qualitative correlation of the two radiance distributions.

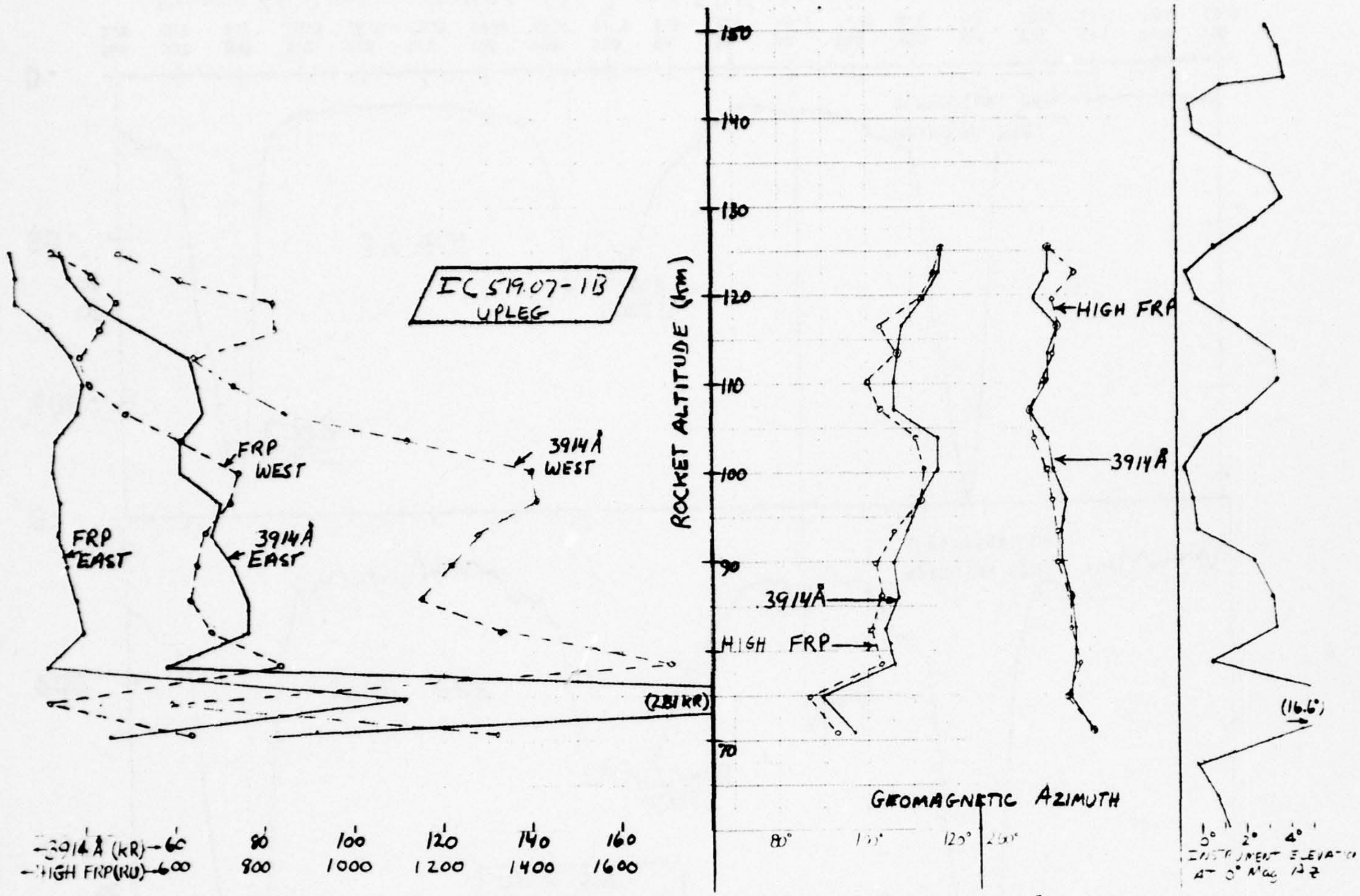

Figure 22. Altitude profiles of peak intensities in the east and west limb, geomagnetic azimuth angles of the peaks and elevation angle of the sidelooking photometers at 0^{o} geomagnetic azimuth, IC519.07-1B upleg.

bombardment, or -18 kR 3914 Å at 0 RU FRP. (This offset is a quantitative expression of the peak-to-valley ratio difference noted in the previous paragraph.) Taking the FRP's bandwidth as 1500 Å (see Fig 19); the mean continuum nightglow intensity as 1 Rayleigh/Å over its sensitivity range (which is conservative for high latitudes, where [NO] can be enhanced); and a mean van Rhijn gain factor of 6 for the elevation angles at which the data are taken, we find that the continuum makes a contribution of 9 kR-equivalent to this latter offset. While this figure does not quantitatively explain the zero-offset, it does suggest that the airglow continuum is at least partially responsible for it.

Since the data taken when the rocket was below 100 km altitude (which correspond to higher intercept altitude on the arc) constitute the majority of the readings and lie at generally higher radiances, they dominate placement of the least-squares fit line. We therefore also treat separately the higher-altitude data (not underlined in Fig 23), since 1) the relative contribution to the FRP signal from 5577 Å photons decreases more steeply below 100 km (Ref 12) and 2) the contribution from the nightglow continuum should decrease very rapidly above 100 km. For these data points the slope is 5.0 (RU/kR 3914 Å) and the FRP = 0 intercept -11 kR. This higher slope is expected on the basis of the decreasing relative excitation of N_2^+ fluorescence previously noted. The smaller intercept value is at least in part due to the great reduction in NO + O continuum radiance when the sensor is above 100 km.

Fig 24 is a scatter plot of FRP-3914 Å intensities over three complete 360° spin cycles, at the representative rocket altitudes 97, 110, and 139 km. Samples were taken at 10° azimuth intervals, and where the data were noisy they were averaged over about 5° in azimuth. The unweighted least squares fit of FRP to 3914 Å radiance more closely approaches the origin than the fits in Fig's 23 and 26, the offset being -5 kR taking all data points. The slope using all data points is 5.2, significantly higher than that derived from all the isolated auroral limb radiances (see the comparison line on Fig 24). As expected this slope is

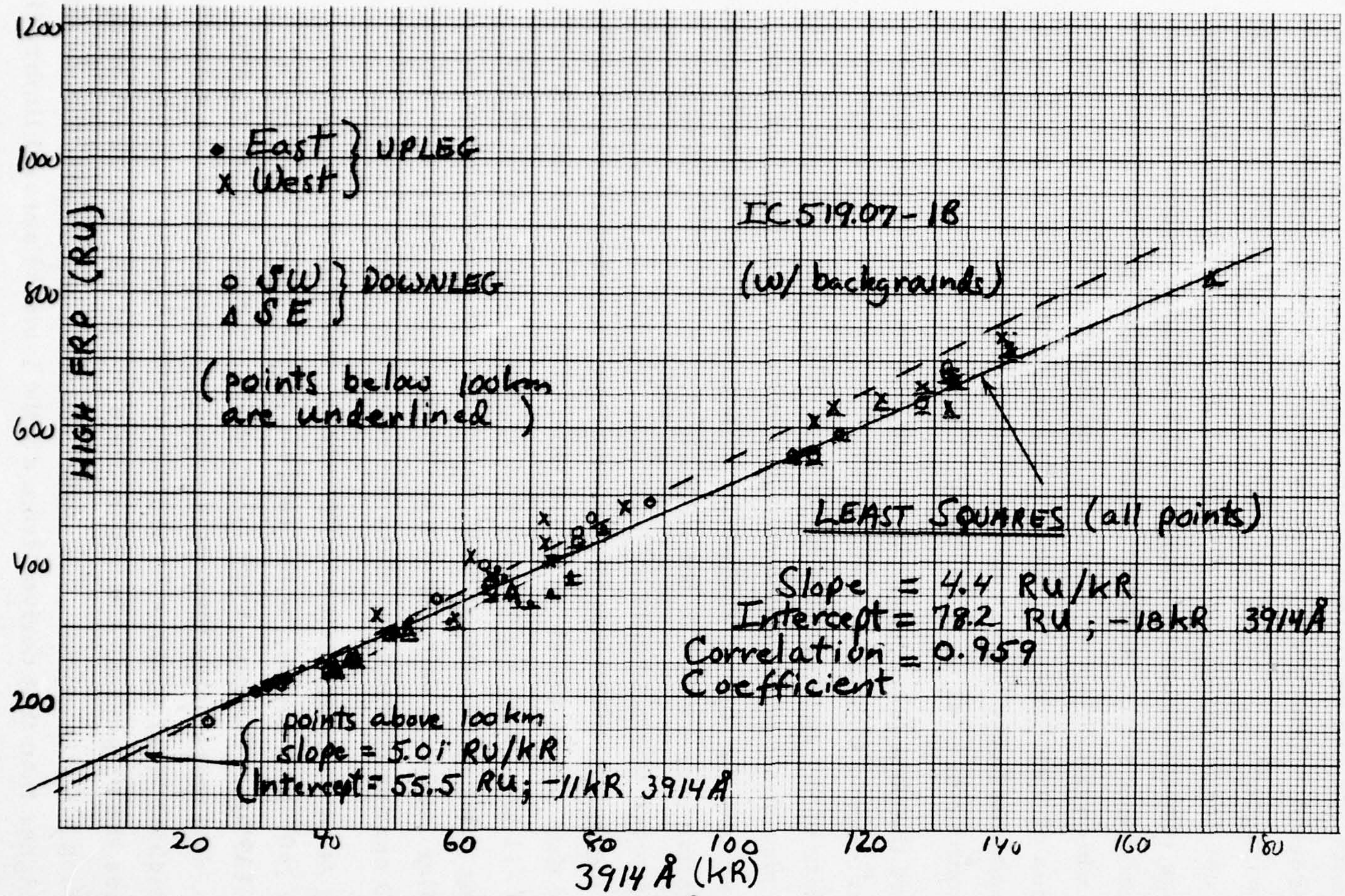

Figure 23. Scatter plot of 3914 Å and FRP limb peak intensities (background included), with a least squares fit to the 3914 Å readings, IC519.07-1B.

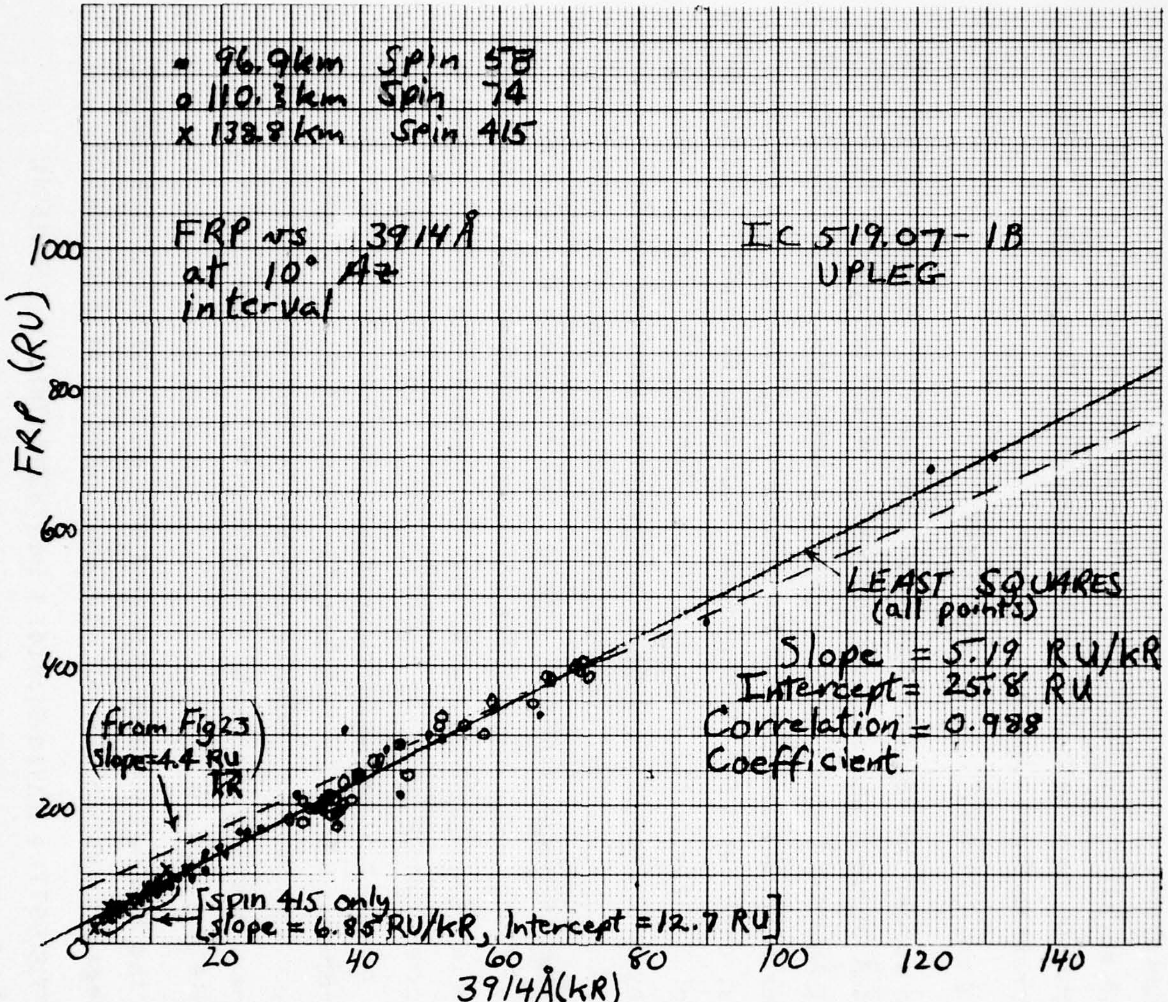

Figure 24. Scatter plot of 3914 Å and FRP intensities (background included) at 10° azimuth intervals over three 360° spin cycles of IC519.07-1B on upleg, with least squares fits.

markedly higher when the rocket is at 139 km. Furthermore the intercept drops to < -2 kR 3914 Å, which is large in comparison to what would be expected from any OI red-line (metastable) emission remaining in the instrument field. At the lowest fluorescent intensities measurable (at very high rocket altitudes) above the aforementioned noise, ~2 kR, the FRP signal is too erratic to establish the contribution of its phototube's dark current to these offsets.

EFFECT OF OI GREEN LINE EMISSION

To assess the relative contribution to the FRP signal from 5577 Å and 3914 Å auroral photons, we compiled altitude profiles of FRP/3914 Å and 5577 Å/3914 Å ratios (Fig 25) and a scatter plot of 5577 Å - 3914 Å radiances (Fig 26), for the arc limb maxima. (The data are the peak readings, unadjusted for "background" below the isolated maximum or for offsets of the type in Fig's 23 and 24). The 5577 Å/3914 Å ratio, as viewed by the rocket's sidelooking photometers (see our earlier comments on their actual elevation angles and arc-intercept altitudes), remains sensibly constant at 1.3 up to ~105 km where it begins to increase slowly. The slope of the least-squares fit of 5577 Å to 3914 Å radiance is somewhat less (1.22, Fig 26) because the 5577 Å signal is zero-shifted upward about $8\frac{1}{2}$ kilorayleighs. The radiance ratio FRP/3914 Å, however, shows a greater relative increase with rocket altitude (compare the 3 x 5577 Å/3914 Å profile drawn in Fig 25), which starts at 95 km. This larger relative increase is expected because the N_2^+ fluorescent intensity maintains a contribution to the numerator of the FRP/3914 Å ratio.

If the FRP's response depended only on the OI green line and N_2^+ First Negative system, its output signal would be proportional to

$$I(5577)S(5577) + I(3914)S(3914) + I(4278)S(4278) + I'(FN)\overline{S}(FN),$$

where the I's represent the relative photon intensities of the features and the S's the sensitivity of the FRP at the indicated wavelengths. The last term in the expression above makes a small additive correction for the bands of the First Negative system other than (0,0) with head at

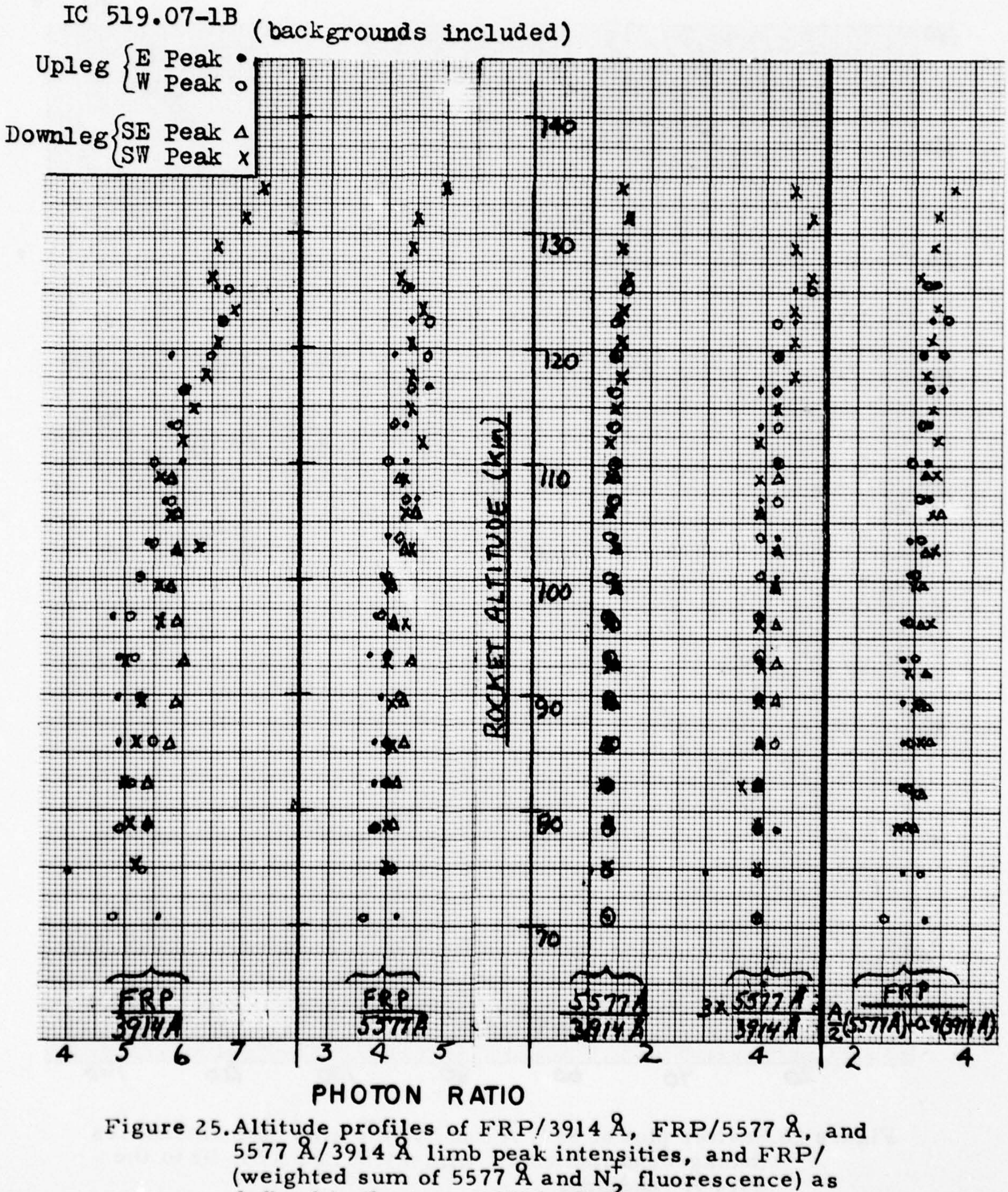

Figure 25. Altitude profiles of FRP/3914 Å, FRP/5577 Å, and 5577 Å/3914 Å limb peak intensities, and FRP/ (weighted sum of 5577 Å and N_2^+ fluorescence) as defined in the text, IC519.07-1B.

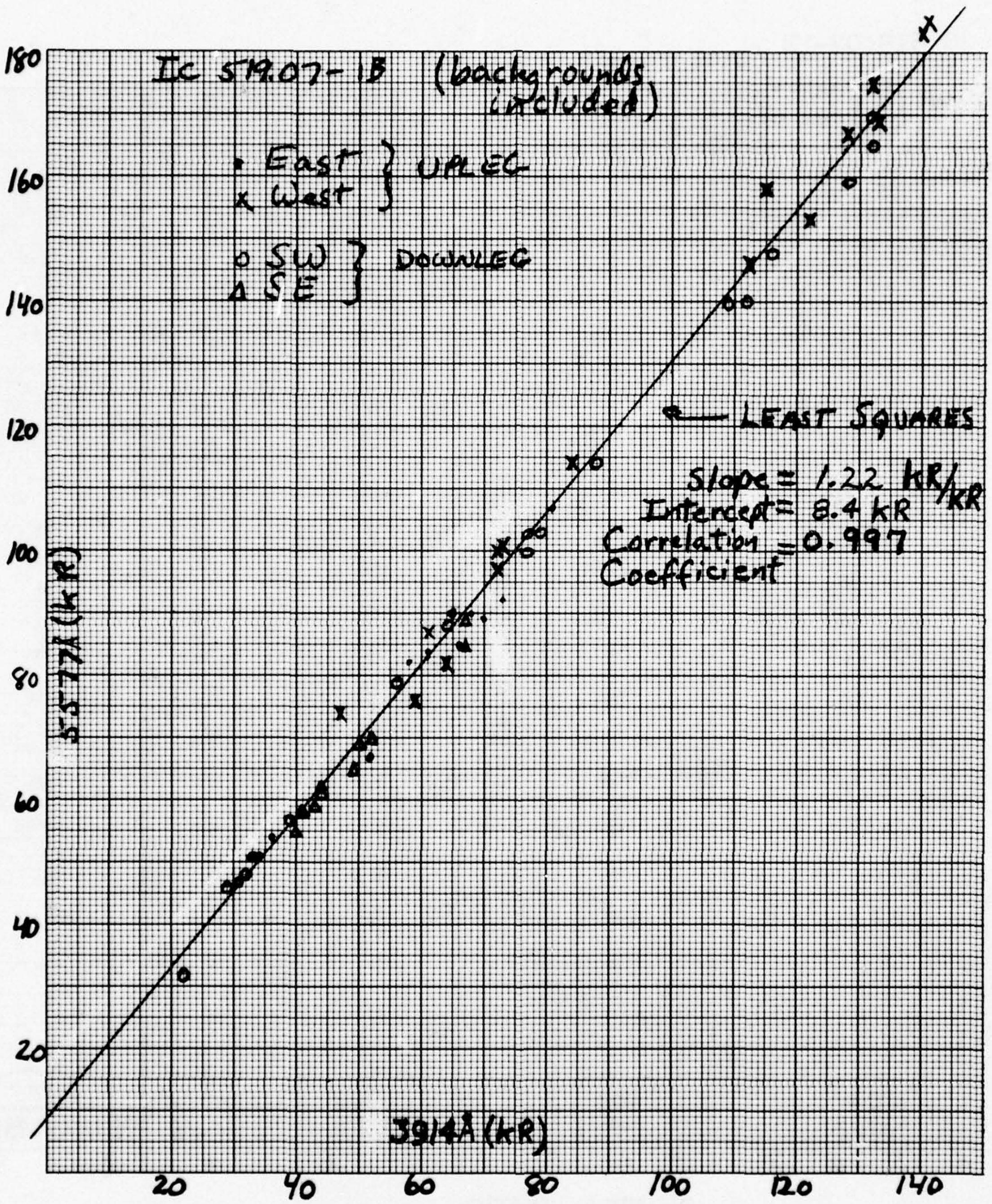

Figure 26. Scatter plot of 5577 Å and 3914 Å limb peak intensities (background included), with a least squares fit to the 3914 Å readings.

3914 Å and the 0.34-as-intense (0,1) at 4278 Å, in which are emitted ~1/6 as many photons as at 3914 Å. Applying the spectral response in Fig 19, this expression becomes

$$\frac{A}{2.0}\, I(5577) + 0.9\, I(3914) \equiv \Sigma\ ,$$

where A is the measured altitude-dependent ratio I(5577)/I(3914) (or as we have been labeling it 5577 Å/3914 Å) plotted in the center of Fig 25. The ratio FRP/Σ, at the right of Fig 25, shows a slow increase with altitude. This observation indicates that aurora-associated emitters whose intensities are not proportional to the FRP sensitivity-weighted sum of OI 5577 Å and N_2^+ First Negative band, are contributing relatively more photons to the film response photometer as the altitude of energy deposition increases (or alternatively, less with decreasing deposition altitude). Presumably these sources include metastable radiating species, less quenched at the higher altitudes.

SUMMARY, APPLICATION TO USE OF THE FRP ON AIRCRAFT

The ratio FRP/Σ in Fig 25 gives an indication of the departure of the FRP's response to actual auroral emission from its calculated response to high altitude air's two major visible features, for the viewing geometry of arc limbs. Fig's 23 and 24 show experimentally significant differences between the quantity that panchromatic film with fast wide angle lenses measures at different excitation altitudes, when this quantity is referenced to the electron impact-excited N_2^+ First Negative Band radiance that is conventionally taken as proportional to the column rate of production of ions by energetic charged particles. (Refer to Section V of Ref 3 for a review of the altitude dependence of this proportionality.) The offset of the FRP signals at low and high altitudes can at least in part be attributed to types of "predosing." No substantive evidence of nonlinearity of the FRP's response with auroral "intensity" at a given altitude - due to changes in volume rate of energy deposition, length of column viewed, or both - is resolvable in the sidelooking photometry data that we analyzed.

Since these results were derived from an isolated (albeit diffuse) auroral arc viewed at low elevation angles (< 20^{o}) from near coaltitude, they refer, in effect, to altitude profiles of the FRP's intensity response relative to the radiance of "standard" auroral features. To assess the FRP's performance when it views aurora in the zenith from below the excited volume, as from the aircraft, the rocket data presented here should be weighted by the altitude profile of energy deposition by the incoming charged particles. The usual concentration of this excitation in a height range of $\lesssim$ 25 km in the intense aurora most useful for measuring infrared emissions would have the effect of damping the altitude dependences that we observe from the multi rocket. (In addition the contribution of the continuum is small for zenith views.) That is to say, the aircraft FRP's signal from the aurora-excited vertical column would be expected to follow the 5577 Å and 3914 Å photometer signals even more closely than is indicated in the data in this Section. The FRP's response for the aircraft's viewing geometry could of course be more accurately determined by measurements on aurora from a ground station.

SECTION IV

N^2D DIFFERENTIAL PHOTOMETER, A18.219-1

FUNCTION

ICECAP 1974's multi-instrumented rocket (Sections I and II; Ref 3, Section II) carried a differential photometer whose performance in isolating the N^2D-^4S forbidden doublet 5198.7-5200.5 Å from nearby and overlying fluorescent and chemiluminescent radiations is evaluated in this Section. The radiance in this weak auroral-airglow feature measures the column concentration of atoms in the long-lived metastable upper (^2D) state, which, since they react relatively rapidly with ambient O_2, are considered to be the major precursor of 2.8μm overtone emission from vibrationally-excited NO molecules. A sidelooking filter radiometer boresighted with the differential photometer measured this infrared emission, as reported in Section II of Ref 3.

Earlier measurements from multi rockets made by single narrow wavelength-band photometers (Ref 1, Section I; Ref 3, Section I) indicated concentrations of N^2D in arcs below ~ 115 km at least an order of magnitude higher than those determined from the ground and aircraft with tilting filter photometers (Ref 1, Section V; Ref's 13, 14). The latter results are consistent with the N^2D state's known short lifetime against collisional deactivation at these altitudes. We interpreted the high readings from the rocket photometers as due principally to leakage to the photocathode of radiation at wavelengths just below the principal passband of the interference filter incident at angles greater than the $2\frac{1}{2}^{\circ}$ half-angular field (Ref 1, Appendix XV). The conclusion that auroral fluorescence overlapping 5199 Å is not the major source of the large excess signals is supported by ICECAP meridian scans (Ref 1, Section V) from the ground with a well-baffled tilting filter photometer having a passband only ~25% narrower than that of the fixed-filter rocket instrument. The auroral background when the groundbased photometer's sensitivity maximum was located at 5204 Å,

where the N_2^+ First Negative (0, 3) band contributes some signal, was only slightly higher than at 5185 Å, where auroral fluorescence is very weak (more on this point presently).

The differential photometer design is intended to subtract out the in-band contamination by determining its relative intensity over a narrow and a wider wavelength interval. The instrument would compensate adequately for the contribution of photons to the signals arriving from off-axis angles if the out-of-band responses of each of its channels were proportional to their respective bandwidths for all spatial distributions of auroral radiance. (Each channel has the same optical system as the photometer illustrated in Appendix XV of Ref 1; the off-axis transmission is not calculable a priori, and in any case the spurious photocurrents would be expected to depend on the specific spatial distribution.) To evaluate the performance of the differential photometer when viewing aurora at low elevation angles, we have made this preliminary review of the N^2D intensity data from the instrument coaligned with the other sidelooking photometers and radiometers on sounding rocket A18.219-1.

SPECTRAL SENSITIVITY OF THE PHOTOMETER AND DISTRIBUTION OF THE SOURCE

Fig 27 shows the transmission of the differential photometer's narrow-band (10 Å FWHM) and wider-band ($26\frac{1}{2}$ Å FWHM) interference filters, measured at normal incidence; the relative intensity in the N^2D-^4S forbidden doublet (corrected from Fig 17 of Ref 1); and the relative spectral intensity in the N_2^+ (0, 3) band at 300 K rotational temperature convolved with a 1 Å triangular scanning slit (also from Ref 1). This temperature implies a mean emission altitude at $116\frac{1}{2}$ km (CIRA 72 model atmosphere), which is representative of IBC-II auroral conditions; in any case, the intensity distribution in the lines of the R branch overlapping the filter passbands does not change rapidly enough with ambient temperature to impact detectably this present evaluation. (For peak energy deposition at $116\frac{1}{2}$ km, the

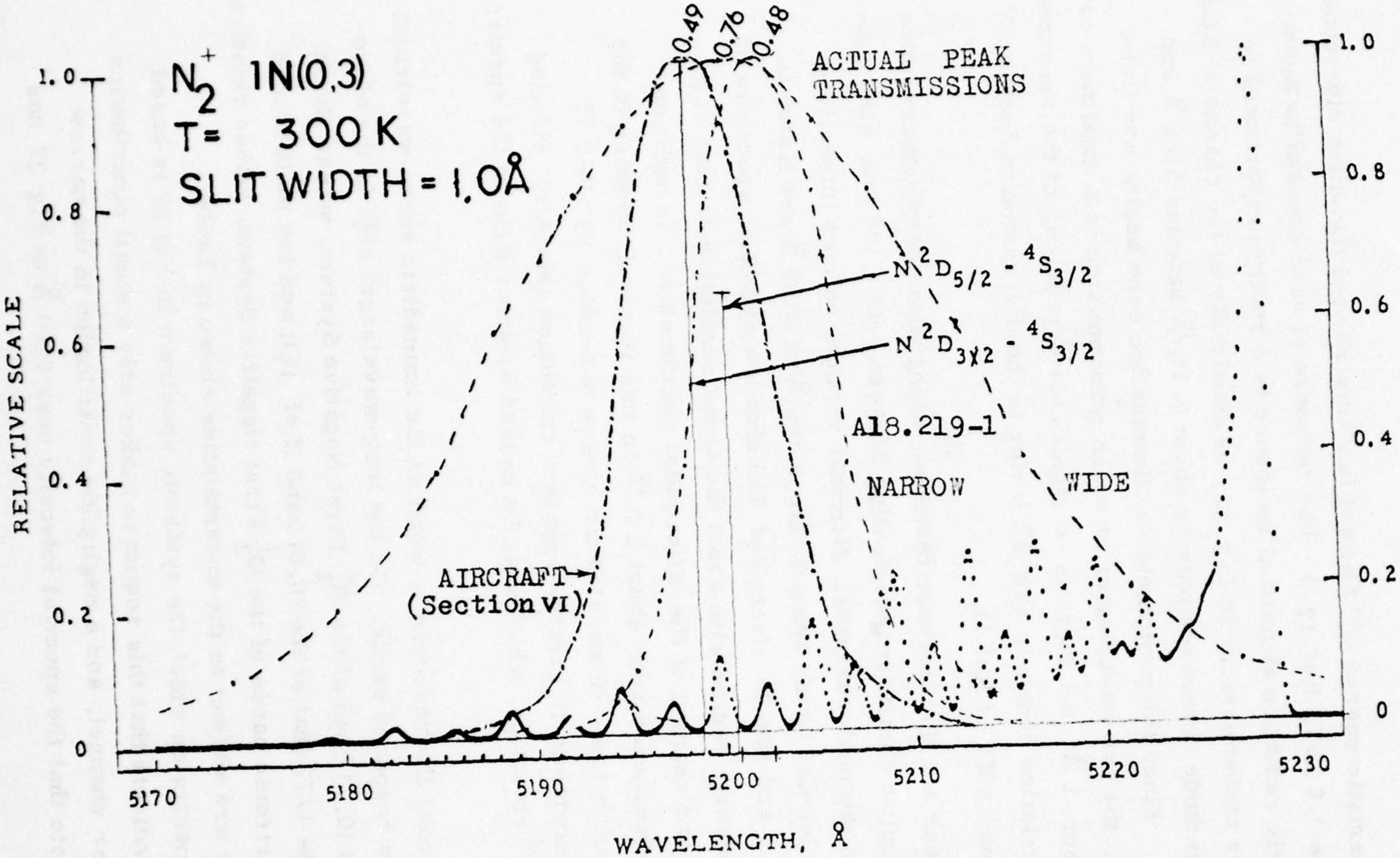

Figure 27. Transmission of the filters in the differential photometer (at normal incidence), and spectra of the $N\,^2D-^4S$ doublet and N_2^+ First Negative (0, 3) band.

characteristic energy of "Maxwellian"-distributed incoming electrons would be 3.0 keV, Ref 12.) The response of each channel to monochromatic radiation at normal incidence is directly proportional to the filter transmissions in Fig 27, as sensitivity of the channels' RCA 4516's cathode decreases only by about 0.1%/Å between 5180 Å and 5230 Å. Since the photometer's illumination cone angles are finite (5^{o} full), the two wavelengths at which transmission is a maximum each shift about -1 Å, but there is no significant broadening of the response characteristics shown in Fig 27 (refer to the discussion in Section IV and Appendix XV of Ref 1).

Other air fluorescence features, along with chemiluminescence in the airglow continuum originating between ~90 - 100 km, also contribute to the photocurrents. Nominal vertical column intensities of the molecular bands lying within ± 100 Å of 5199 Å are listed in Table 1, and Fig 28 (from Ref 15) shows a synthetic spectrum of this wavelength region with about the same resolution as that of the narrow-band channel of the differential photometer. In addition chemiluminescence adds about 2 R/Å in this interval, viewing in the zenith from below ~90 km altitude (compare Section III; Ref 15 reports substantially greater apparent continuum intensity viewing at 16^{o}-47^{o} elevation, which may be caused by stray light in the spectrometer).

Auroral fluorescence is weak on the immediate short-wavelength side of the response bands. On the long-wavelength side is the aforementioned (0, 3) band of the N_2^+ First Negative System, whose photon intensity is 1/72 that of the (0,0) band (Ref 16); and the multiheaded $\Delta v = 2$ electronic bands of the O_2^+ First Negative System, whose relative intensities are subject to the uncertainties shown in Table 1. Auroral spectra on which the synthetic spectrum in Fig 28 is based (Ref 17) indicate that this sequence makes only a small contribution in the wider channel, and a negligible contribution in the narrow channel (note that the spectral intensity near 5200 Å in Fig 28 has

Table 1. Air Fluorescence Bands Near 5199 Å *

Spectral Feature	Band Head Å	Shaded to	Nominal IBCIII R**
N_2 V-K (4, 17)	5090	Red	230***
N_2^+ 1N (1, 4)	5150	Blue	280
N_2^+ (M) (7, 1)	5174	Red	80
N_2 2P (2, 9)	5179	Blue	30
N_2^+ 1N (0, 3)	5228.3	Blue	780
N_2 V-K (5, 18)	5226	Red	170***
O_2^+ 1N (7, 5)	5234	Blue+	< 100, 400++
O_2^+ 1N (6, 4)	5241	Blue+	< 100, 200++
O_2^+ 1N (5, 3)	5251	Blue+	< 100, 600++
O_2^+ 1N (4, 2)	5259	Blue+	200, <200++
O_2^+ 1N (3, 1)	5275	Blue+	1400, 700++
O_2^+ 1N (2, 0)	5296	Blue+	1800, 700++
N_2 2P (1, 8)	5309	Blue	30

----

*From Ref's 15 and 17 except as indicated. V-K=Vegard-Kaplan band; 1N = First Negative; M=Meinel; 1P, 2P= First, Second Positive. Refer to text for estimate of continuum-chemiluminescence intensity.

**Column intensity viewing in the zenith when N_2^+ 1N (0, 0)=50 kR; only approximately represents sidelooking column radiance.

***Quenched at altitudes below ~120 km, therefore contributes relatively less to photometer signal.

+Complex (and diffuse), heads extend ~40 Å to blue from first head listed.

++Laboratory value from Ref 18, see text. The high values for the (3, 1) and (2, 0) transitions in Ref 15 may include the (4, 2), (5, 3), (6, 4), and (7, 5) transitions incompletely resolved in the auroral spectra.

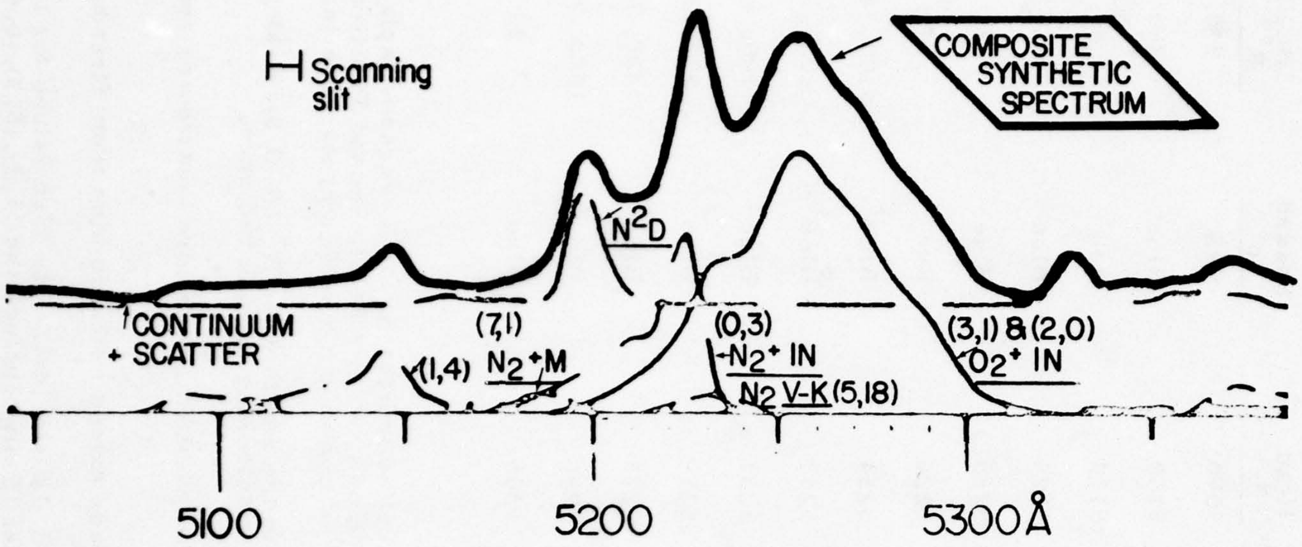

Figure 28. Synthetic auroral spectrum 5100-5300 Å, from Ref 15. In the O_2^+ First Negative system only the (3,1) and (2,0) bands are considered, the (2,9) band of N_2 Second Positive is neglected, and a strong continuum present in the Ref 15 spectrum data is included. The effective transmission of the scanning slit is actually a triangle of 7 Å FWHM convolved with an 8 Å rectangular function.

been increased by convolution with the scanning slit). The laboratory data on O_2 bombarded by kilovolt electrons (Ref 18), on the other hand, show more O_2^+ $\Delta v = 2$ band emission toward shorter wavelengths, which would result in a greater contribution of this sequence to the photocurrents.

PROCEDURE FOR EVALUATION OF FLIGHT DATA

The relationship of the readings from the two channels to instantaneous auroral column intensity measured by a boresighted 3914 Å - photometer is indicated qualitatively in the upleg azimuth-elevation scans in Fig's 29a and b. An isolated, narrow arc with peak 5577 Å radiance ~ 175 kR as viewed from PKR is ~50 km N of the rocket during this data period; refer to Ref 3's All-Sky images (Fig 55) and plot of trajectory and latitudinal extent of the arc (Fig 32). The ordinate scale in the near-meridian altitude profiles (Fig 30) is the rocket's altitude, which is about 11 km below the intercept of its photometers' fields of view on the isolated arc form. The elevation-azimuth scan when the rocket is at 85 km (Fig 29a) includes the airglow chemiluminescence (with a van Rhijn factor that varies between 4 and 10), little of which is expected to be present in the scan from 100 km altitude. Fig's 29 and 30 show that the wider-band channel's signals correlate more closely with the fluorescence directly excited by the aurora-producing particles, as would be expected from their lower content of $N\,^2D-^4S$ radiation.

We selected for this assessment four representative viewing geometries, pointing toward and away from the arc - geomagnetic N and S - from rocket altitudes above and below the main airglow-chemiluminescence layer - 85 km and 100 km. The radiance data points, which are averages over ~10° in azimuth averaged from two successive spin cycles, are listed in Table 2. No correction for the "background" levels has been attempted, as these should in principle drop out of the subtracted data, and in any case the baseline radiances

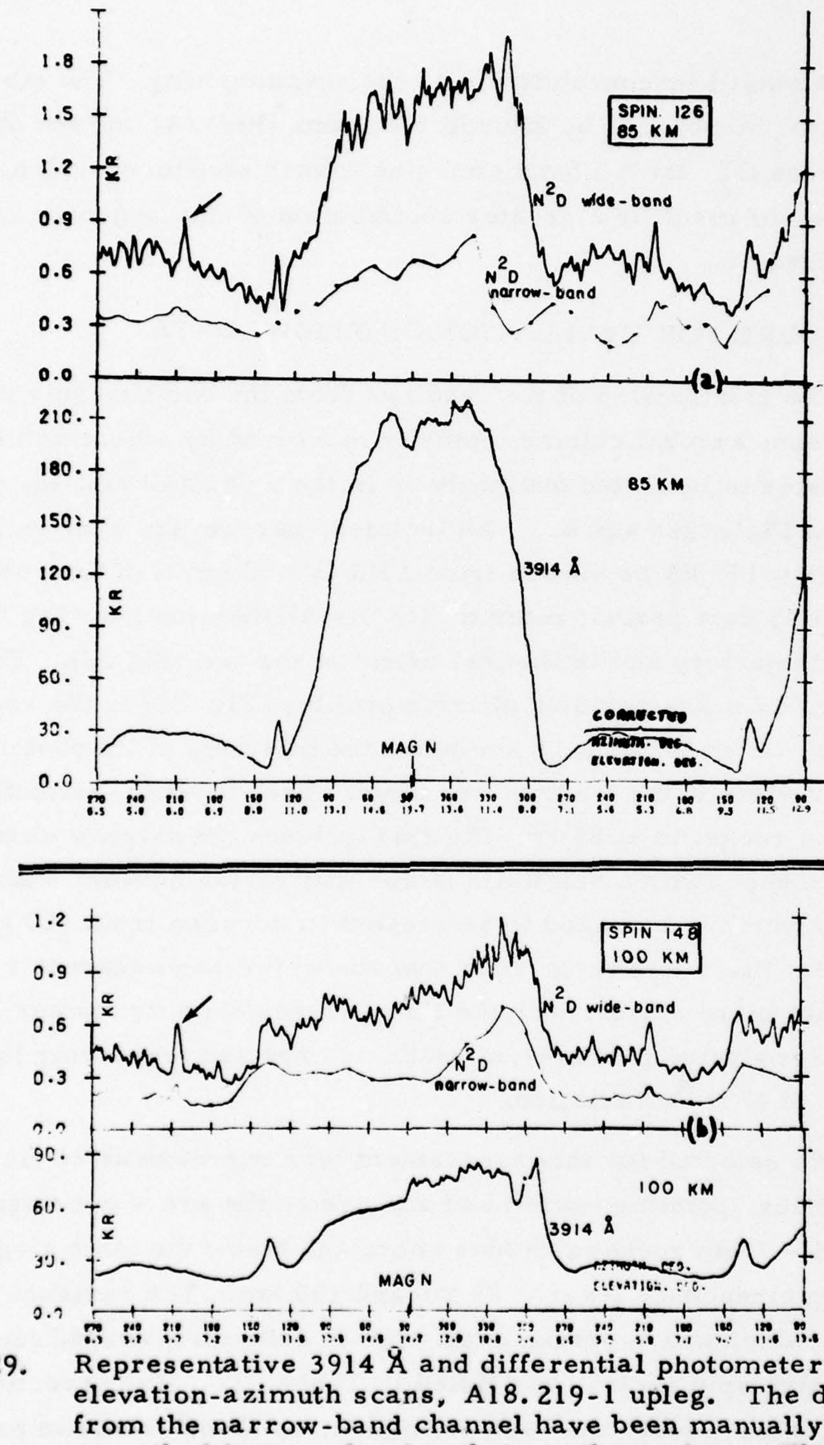

Figure 29. Representative 3914 Å and differential photometer elevation-azimuth scans, A18.219-1 upleg. The data from the narrow-band channel have been manually smoothed in transferring them to these plots. The arrow points to the feature identified in Section I as due to the star Sirius in the instrument's field of view.

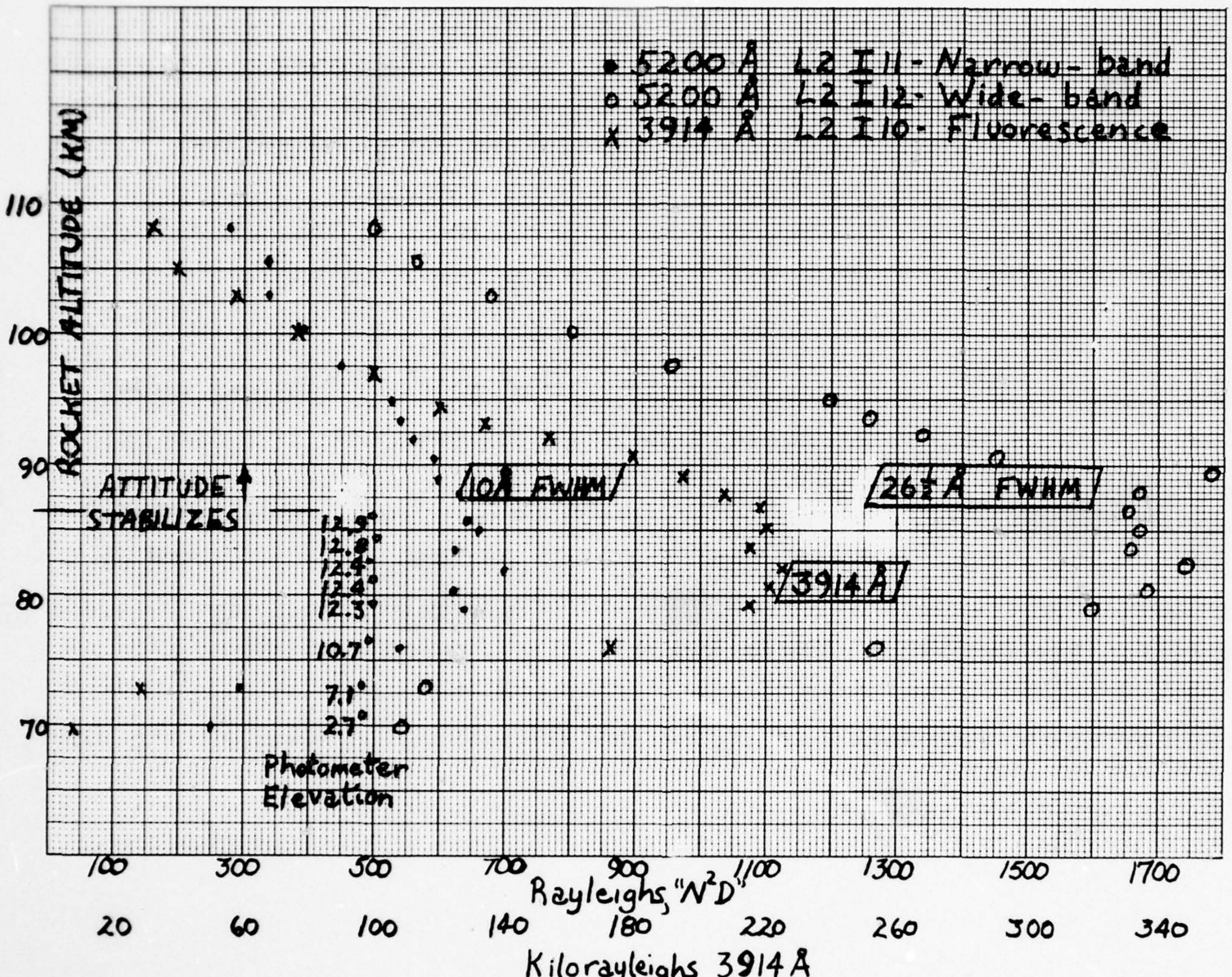

Figure 30. Altitude profiles of air fluorescence and signal levels of the two channels of the N^2D differential photometer at 330^o magnetic azimuth, A18. 219-1 upleg.

Table 2. Differential Photometer and Air Fluorescence Data for Table 3.

Item	Rocket Altitude,	Photometer Pointing	N^2D Wide(w), R	N^2D Narrow(n), R	3914 Å, kR
1	85 km,	360° Az, 11° Eℓ	1490	590	195
2	(Spins 125-7)	180° Az, 9° Eℓ	685	270	$28\frac{1}{2}$
3	100 km,	360° Az, $11\frac{1}{2}$° Eℓ	685	325	67
4	(Spins 148-9)	180° Az, 9° Eℓ	330	200	24

are expected to be a real physical effect of buildup of $[N^2D]$ in the auroral ionosphere (Ref 13). We make the assumption that each channel's calibration in terms of $N^2D-{}^4S$ radiant intensity, in which units the data have been presented by the photometer group, refers to its response to a doublet (only) whose lines have the 1.53:1 ratio and location on the sensitivity band shown in Fig 27. (The aforementioned shift in effective filter transmission, while introducing quantitatively substantial changes in the narrow channel's signal levels, was found in auxiliary calculations not to change qualitatively the conclusions of this evaluation.)

The radiation flux reaching each photocathode may thus be related to its datum point by the equation

(Transmission to $N^2D-{}^4S$) $\times$ (Actual $N^2D-{}^4S$ radiant intensity) +

Σ (Transmission to background feature) $\times$ (Radiant intensity of background feature)

= (Transmission to $N^2D-{}^4S$) $\times$ (Radiant intensity datum).

The background flux is the sum of products of spectral intensity of fluorescence bands (and continuum) and filter transmission. Applying the filter curves in Fig 27, we find that the weighted transmissions to the doublet are 0.39 and 0.75, and the area integrals (transmission summed over wavelength) are 4.8 Å and 20.3 Å, respectively for the narrow-band and wider-band channels of the differential photometer.

The two auroral "N^2D" data points in a row of Table 2 in two linear equations of the above form allow for solution for the $N^2D-{}^4S$ radiant intensity and the intensity of one background contaminant feature. Intensities of other auroral features can be ratioed to this latter number (we shall provide examples presently). Successful application of this concept requires, of course, that the folding of background spectral intensity into the response characteristics has been performed correctly, and that off-band-off-axis leakage is either negligible or relatable to the area integrals for all scene brightness distributions.

EVALUATION FOR SYNTHETIC-SPECTRUM MODELS

The first-approximation fit to the data (Calculation A) assumes that the wavelength-averaged background intensity is the same in the sensitivity bands of both channels. This is the reduction procedure usually applied to data from co-located wide- and narrow-band filter photometer pairs, particularly when little *a priori* information is available about the spectrum of the background radiation. The spectral radiance need not be uniform, or even have constant slope across the passbands; it need only have a shape that contributes photocurrents proportional to the area integrals of the filters.

A spectrum dominated by N_2^+ First Negative (0, 3) band radiation and airglow continuum (refer to Fig's 27 and 28) might appear to meet this condition reasonably well. The two simultaneous equations then become

$$0.39\, N^2D + 4.8r = 0.39n$$
$$0.75\, N^2D + 20.3r = 0.75w,$$

where n and w refer to the input data in Table 2, r is the mean background spectral intensity extending across both sensitivity bands (units are Rayleighs/Å), and N^2D the corrected radiant intensity of the doublet. Solutions of these equations, listed in the second and third columns of Table 3, are clearly inconsistent, as they result in physically-unrealizable negative N^2D-^4S intensities (and excessively high mean backgrounds 5185-5215 Å). Thus this zeroth-order calculation fails to subtract out the fluorescent-chemiluminescent auroral background contaminating the signal from metastable N^2D atom radiation.

The next logical step is to improve the background model by putting in the response of each channel to the expected spectrum of radiation from charged particle-excited air. As a second approximation, we add in the contribution of the (0, 3) band of the N_2^+ First Negative system and calculate the further quasi-continuum background radiance that (we assume) contributes photocurrents proportional to the area

Table 3. Calculated N^2D and Background Intensities from Four Synthetic-Spectra Models

Table Data	Background A, R/Å*	N^2D A, R	Background B, R/Å**	N^2D B, R	N_2^+ (0, 3) C, kR+	$N_2^+(0,3)$ / $N_2^+(0,0)$	N^2D C, R	N_2^+ (0, 3) D, kR++	$N_2^+(0,3)$ / $N_2^+(0,0)$	N^2D D, R	N^2D E, R
1	$81\frac{1}{2}$	-410	20	+40	3.3	1/59	+89	1.9	1/101	+247	+154
2	$37\frac{1}{2}$	-190	22	-47	1.00	1/29	-3	0.58	1/49	+44	+97
3	$32\frac{1}{2}$	-74	12	-129	2.14	1/32	+83	1.25	1/54	+184	+220
4	12	+52	3.8	-28	0.58	1/41	+134	0.34	1/71	+162	+162

*Mean auroral background r over filter bands, as defined in text for Calculation A.

**Mean auroral background r over filter bands, as defined in text for Calculation B

+Intensity of N_2^+ First Negative (0, 3) band, from Calculation C.

++Intensity of N_2^+ First Negative (0, 3) band, from Calculation D.

integrals. We took the intensity of the (0, 3) band as 1/72 that of the (0, 2) band, and folded its rotational spectrum from Ref 1 line-by-line into the transmission characteristic of each filter. The two equations for this Calculation B are then

$$0.39\ N^2D + 0.044\ N_2^+/72 + \ 4.8r = 0.39n$$

$$0.75\ N^2D + 0.253\ N_2^+/72 + 20.3r = 0.75w,$$

where N_2^+ is the measured (0, 0) band intensity, listed in Table 2. (Shifting the filter bandpasses 1 Å to shorter wavelengths gives effective (0, 3)-band transmissions of 0.038 and 0.23 respectively, as compared to 0.044 and 0.253 without such a shift.) This approach to a model spectrum also failed to produce realistic doublet intensities, as the solutions listed in Table 3 show.

Results of three further attempts to fit the differential photometer data are also shown in Table 3. The background spectrum for Calculation C was taken as a continuum having zenith intensity 2R/Å at 85 km and 0 R/Å at 100 km, plus the N_2^+ First Negative (0, 3) band whose intensity is one of the unknowns. The ratio of the inferred (0, 3) band intensity to the measured (0, 0) is the principal test of performance of this fitting procedure. Calculation D is a refinement of C, with the contribution of the $\Delta v = 2$ sequence of the O_2^+ First Negative system added as a fixed fraction of that from the N_2^+ (0, 3) band. Following Ref 15, we took the intensity of the sequence as 4x that of the latter band, and estimated that the wider filter and narrow filter transmit respectively 3% and 0% of its spectrum; refer to the synthetic spectrum in Fig 28. The simultaneous equations for Calculation D are

$$0.39\ N^2D + 0.044\ N_2^{+\prime} + 2v\ \ 4.8 = 0.39n$$

$$0.75\ N^2D + 0.373\ N_2^{+\prime} + 2v\ 20.3 = 0.75w$$

where $N_2^{+\prime}$ is the (0, 3) band's intensity (one of the unknowns) and v an effective van Rhijn factor viewing through the airglow layer (v =

$5\frac{1}{4}$ - $6\frac{1}{2}$ for the 85 km data, and is taken as zero at 100 km rocket altitude). For Calculation C, the equations are the same except that 0.373 (=0.253 + 4 x 0.03) is replaced by the wider-band channel's relative sensitivity to the (0, 3) band only, 0.253.

Calculation C results in too much N_2^+ (0, 3) band radiation and N^2D radiance levels comparable, with one exception, to those typically measured in aurora (see the arc measurements in Section V of Ref 1, and Ref 13). Calculation D results in better fits to the expected (0, 3):(0, 0) band ratio 1:72, but with excessive levels of doublet intensity.

Calculation E uses only the data from the narrow-band channel, correcting them for the contribution from the N_2^+ (0, 3) band whose intensity is ratioed from the measured (0, 0) band plus 2 R/Å of continuum (at 85 km rocket altitude only):

$$0.39\ N^2D + 0.044\ N_2^+/72 + 2v\ 4.8 = 0.39n.$$

The results (last column of Table 3), though also indicating somewhat too high doublet intensities, do show the expected higher N^2D concentrations in the arc. Intensities decrease with photometer intercept altitude in the arc and increase with altitude in the south. Note that even when the continuum is omitted – for the data at 100 km – the N^2D radiances for the conditions of Calculation E remain high.

CONCLUSIONS

These reductions of the data from the sidelooking differential photometer on A18.219-1, which apply various plausible model spectral distributions for the auroral background, have failed to provide credible values for the intensities of radiation in the N^2D-^4S doublet toward and away from an auroral arc.

The very poor results with Calculation A are most likely due to its inappropriately simple background spectrum. The inconsistencies from Calculations B-E – too much N_2^+-band and/or N^2D-^4S intensity – appear to stem from the excessively high signals in the narrow-wave-

length band channel. These photocurrents may result from inadequate baffling of the photometer's optical system against radiation from off-axis angles, as discussed earlier.

Since the spectral intensity of particle-excited air at auroral altitudes is both uncertain and decreasing sharply with decreasing wavelength near 5200 Å, the background is better referenced with narrow sensitivity-band channels than with a single broad channel. A second $\sim 7\frac{1}{2}$ Å photometer centered at 5205 Å would most likely provide adequately quantitative N^2D-^4S radiance data, for example (refer to the discussion on p128 of Ref 1). In contrast to the zenith view from aircraft (Section VI), the near-sidelooking view from sounding rockets results in a high contribution from the airglow continuum; - a layer with zenith spectral radiance 2 R/Å viewed with the typical van Rhijn path-length enhancement of 5 would produce 2 x 5 x 8 Å ≈ 80 R of spurious signal, which is comparable to the expected radiance levels in the doublet. Therefore even if the air fluorescence in molecular bands can be compensated by an improved synthetic spectrum and monitoring of the N_2^+ First Negative system's intensity, a reference photometer is needed in coordinated experiments from multi-instrumented rockets to measure accurately the column-concentrations of N^2D precursor atoms.

SECTION V

HIRIS VIEWING GEOMETRY

AURORAL CONDITIONS, POINTING REQUIREMENT

A Sergeant rocket carrying the helium cooled high resolution ($2\ cm^{-1}$) interferometric spectrometer payload HIRIS II (IC630.02-1A) was launched at 0805:20 UT 01Apr76 from Poker Research Range, AK to measure 4-22μm infrared emissions resulting from excitation of the upper atmosphere by energetic charged particles (Ref 19). Ground based observations (Ref's 19, 20) showed that there had been substantial predosing, a Class III+ breakup just before launch, and a weakening and southward movement of the visible aurora starting about one minute after launch. Large spatial/temporal variations in bombardment intensity were observed near the trajectory, with the rocket penetrating Class II diffuse regions on both upleg and downleg.

All-sky views of the spatial distribution of excitation as viewed from Poker Flat and Fort Yukon, along with projections (eℓ and az from these stations) of both the rocket and intercept of the magnetic field line through it with a plane at 100 km altitude, are in Fig 58 of Ref 3. Ref 20 contains further all-sky images, meridian photometer scans (records from both stations in four emission features are available), and other geophysical data characterizing the auroral ionosphere and lower atmosphere before and during flight. Ref 21 gives in addition electron density contours, energy spectra of the precipitating particles, and other ionosphere parameters derivable from incoherent-backscatter data taken by the DNA 617 (Chatanika) radar.

Vertical attitude stabilization was not achieved due to a malfunction of the rocket's control system that caused its long axis to pitch at $10\frac{1}{2}$ degrees/sec. Thus the spectrometer scanned periodically across the earth's limb and surface as well as through auroral particle-

excited air. This section outlines the procedure for establishing pointing of the tumbling instrument's field of view (taken from the aspect and trajectory data, Ref 22) against the dynamically-changing, three-dimensional aurora (whose surface radiance distribution is determined from meridian scanning photometer and all sky camera data records).

ROCKET POINTING GEOMETRY

A projection into the meridian plane of the rocket's trajectory, whose plane lay 8° E of geomagnetic N, is in Fig 31. During the time that the instrument door was open (88 km on upleg to 62 km on downleg) the rocket rotated six times about a horizontal axis, with a period of closely $34\frac{1}{2}$ sec. The period about a vertical axis was about $\frac{1}{2}$ sec longer, which results in a slow N → E directed (clockwise as viewed from above the rocket) precession of the azimuth angle at which the spectrometer's optic axis reaches each elevation angle. Specifically, the rate of precession around the vertical direction averages $\sim +0.013°$/sec, or 360° in $7\frac{1}{2}$ hr, so that this azimuth angle increases by $\sim 0.46^{\circ}$ per rotation of the rocket about a horizontal axis ($\pm$ 0.25° in the six rotations, as indicated by the entries in the last column of Table 4).

The inset in Fig 31 illustrates the spectrometer's elevation and azimuth pointing angles in 1 km altitude intervals for the first such (complete) rotation in the data period (altitudes 96 to 116 km). Fig 32 is a parallel, vertical projection of the rocket's long axis onto a horizontal plane for this rotation, without considering its 14 km northward movement or 20 km rise. The lengths of the lines in Fig 32 are proportional to the apparent length of the rocket to an overhead observer traveling parallel to the rocket's ballistic trajectory at a distance large compared to the rocket's full length. In the rocket's translational frame of reference, its nose - that is, the spectrometer - is describing a cone of full angle $\sim 165^{\circ}$ whose axis points at an average elevation of + $\sim 9^{\circ}$ and azimuth $\sim 130^{\circ}$ during the six rotation

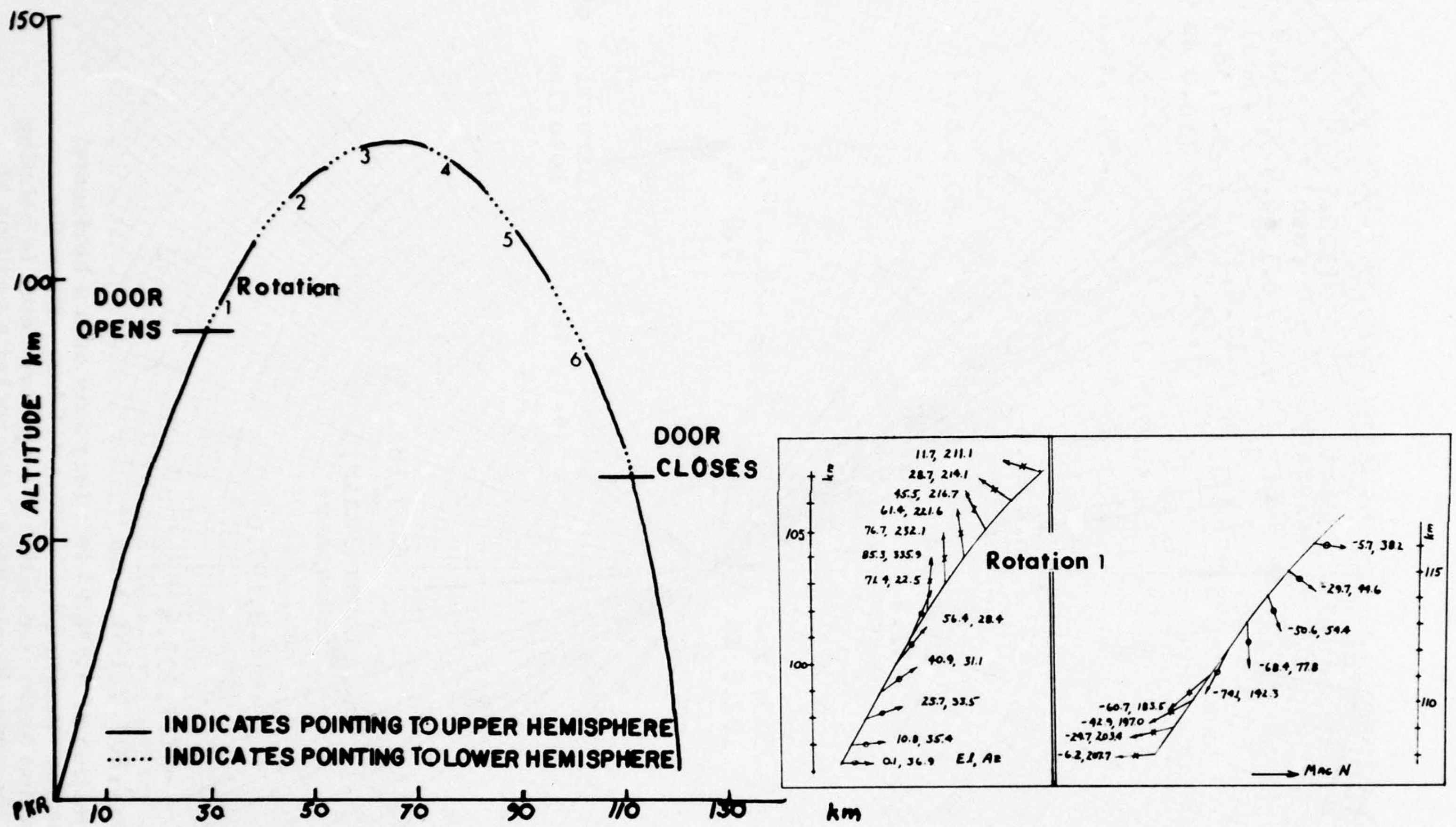

Figure 31. Trajectory of HIRIS II (IC630.02-1A) projected into the meridian plane through PKR, with the altitude ranges over which the axially mounted interferometric spectrometer points into the upper and lower hemispheres. The insets show the elevation and geomagnetic azimuth angles of the rocket's long axis in 1.0-km altitude intervals during the first complete rotation of the rocket about a horizontal axis after the instrument begins to take data. o's and x's indicate E and W pointing components, out of and into the plane of the page respectively.

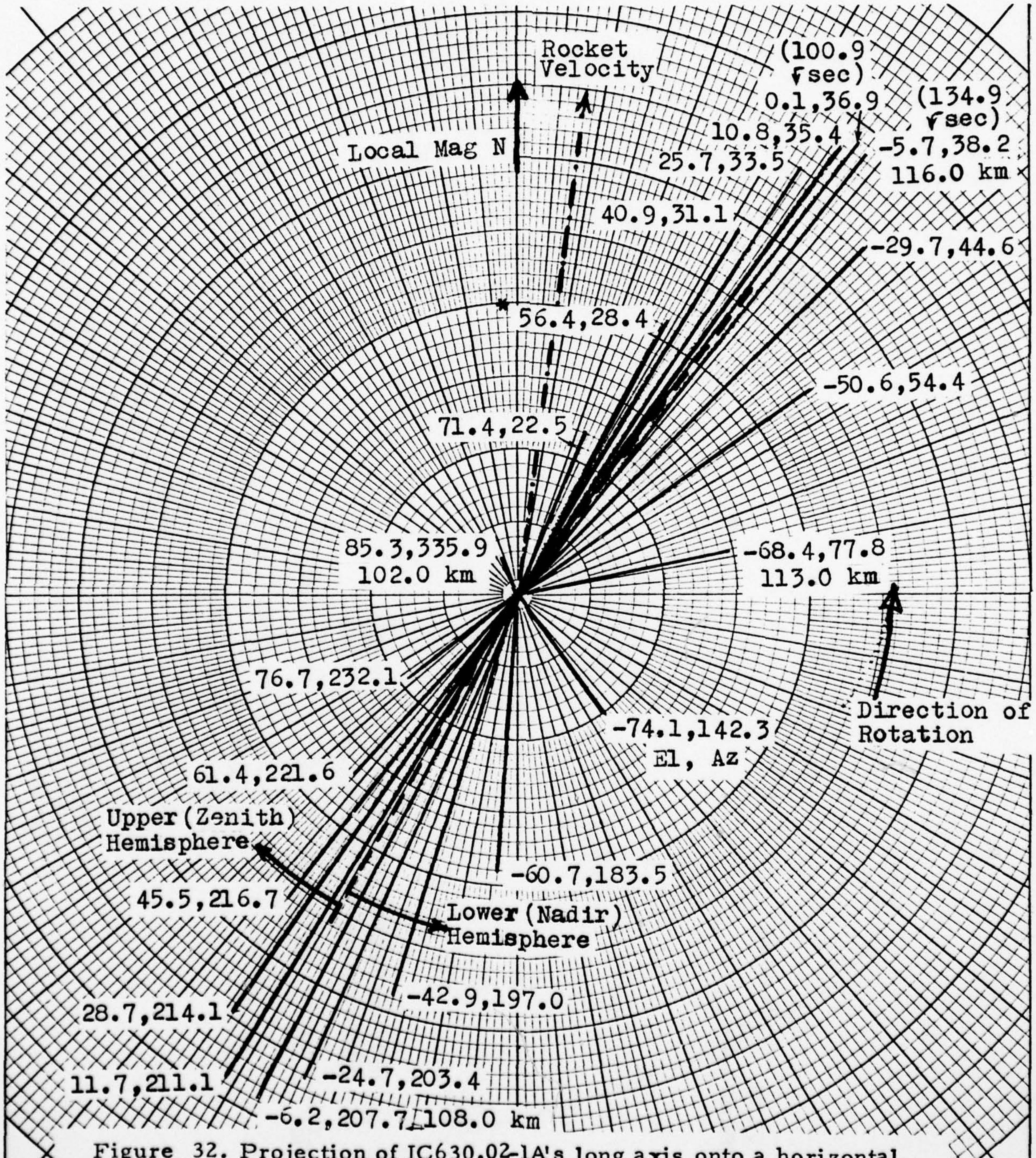

Figure 32. Projection of IC630.02-1A's long axis onto a horizontal plane for Rotation 1, 96 to 116 km. When the elevation angle is positive the spectrometer is pointing into the upper hemisphere. The rocket's position at 106 sec (*) keys to Fig 34.

Table 4. Times/Altitudes of Zero, Maximum, and Minimum Elevation Pointing Angle of IC630.02-1A

Rotation	Time (sec after launch)	Rocket Altitude (km)	Instrument Elevation (degrees)	Instrument Azimuth (geomagnetic)
1	100.9	96.3	0.0	36.9
	109.3	102.2	86.2	304.0
	118.2	107.7	0.0	209.1
	126.6	112.2	-74.9	129.6
2	135.5	116.2	0.0	37.1
	143.7	119.3	85.3	301.0
	152.6	121.9	0.0	210.4
	161.1	123.7	-75.0	125.5
3	170.0	124.9	0.0	37.8
	177.9	125.3	84.0	320.4
	187.1	125.0	0.0	211.0
	195.3	124.1	-77.5	129.5
4	204.5	122.4	0.0	38.3
	212.4	120.2	84.4	308.3
	221.7	116.9	0.0	213.5
	229.6	113.5	-77.5	130.2
5	239.1	108.6	0.0	38.7
	246.9	103.9	83.0	302.8
	256.1	97.6	0.0	214.8
	264.2	91.4	-77.1	123.1
6	273.3	83.7	0.0	39.2
	280.4	77.2	85.0	308.4
	289.6	67.9	0.0	222.3

cycles. To an observer looking W, as for Fig 31, the rocket appears to be rotating counterclockwise. The "plane" of this rotation – actually the pointing is $\pm 8^{\circ}$ out of plane – is "crabbing," lying some 30° from the 8°-E plane of the trajectory (refer to Fig 32).

The spectrometer completes one spectral scan (compiles a double-sided interferogram) in 1.36 sec. Thus over each $34\frac{1}{2}$ sec rocket rotation it obtains approximately 12 spectra in both the upper and lower hemispheres plus 2 spectra while crossing the earth's limb. Altitudes and times when the indicated maximum, minimum, and zero elevation angles are reached in the six rotations are in Table 4. Near zero elevation angle, when the instrument is viewing aurorally excited air side-on from co-altitude – that is, when the van Rhijn gain is high – its angular sweep rates are $+10.75^{\circ}$ $e\ell$/sec and -2.1° az/sec (upswing), and -10.37° $e\ell$/sec and -1.9° az/sec (downswing). Fig 33 is a detailed altitude profile of the HIRIS spectrometer axis' elevation and azimuth pointing over the data-taking period.

As an example (from Rotation 1), when the rocket was at 96.3 km the instrument's elevation angle is 0° at azimuth 37° (E of local magnetic N). At 102.2 km the rocket's axis was nearly vertical (at 3.8° zenith angle), so that the recorded spectrum represents in effect integrated column emissions overhead from that altitude. Earth limb and van Rhijn effect-enhanced data are again obtained from near 107.7 km (118.2 sec), at azimuths centered at 209°. Minimum elevation (-74.9°) is reached at 112.2 km 8.4 sec later, at $129\frac{1}{2}^{\circ}$ az. The azimuths at which the elevation is 0° increase slowly, as noted previously, in each rotation; the spectrometer points northeast on the upswing, and southwest – back, toward the intense aurora to the S – on downswing.

AURORAL-EXCITATION INTERCEPTS

Meridian photometer scans output quantitative records of visible-auroral emission rates summed over columns extending from the ground

AD-A055 884 PHOTOMETRICS INC LEXINGTON MASS F/G 4/1
ASSESSMENT AND EVALUATION OF SIMULATION DATA.(U)
NOV 77 I L KOFSKY, D P VILLANUCCI, G DAVIDSON DNA001-77-C-0208
UNCLASSIFIED PHM-01-78 DNA-4303F NL

2 OF 2
ADA
055884

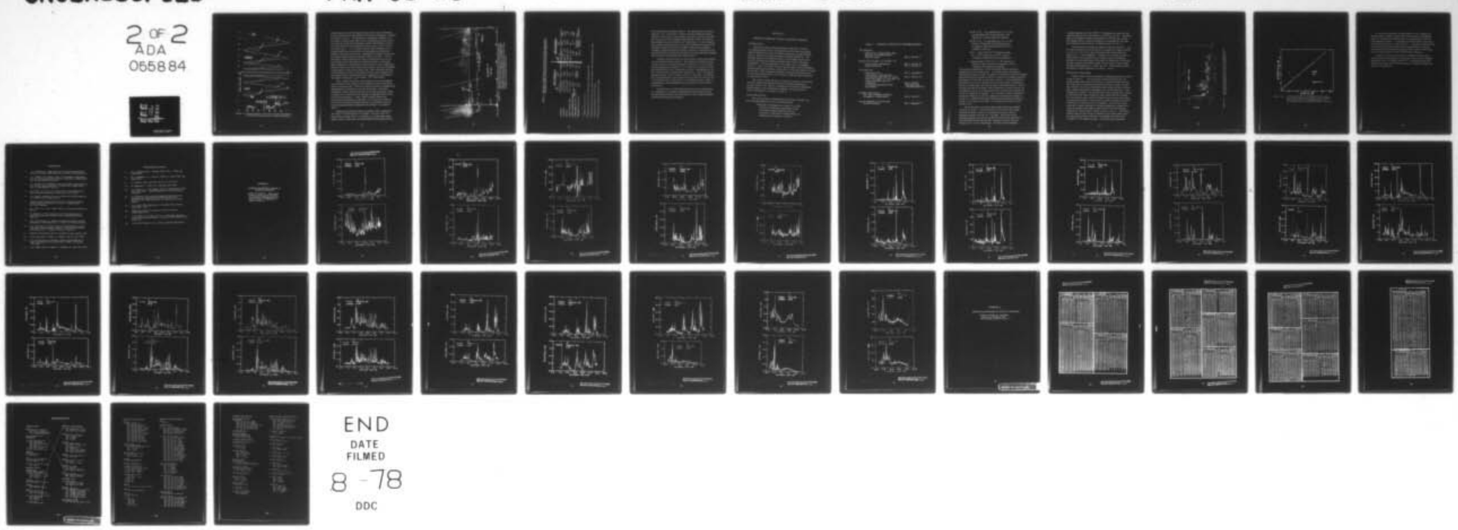

END
DATE
FILMED
8-78
DDC

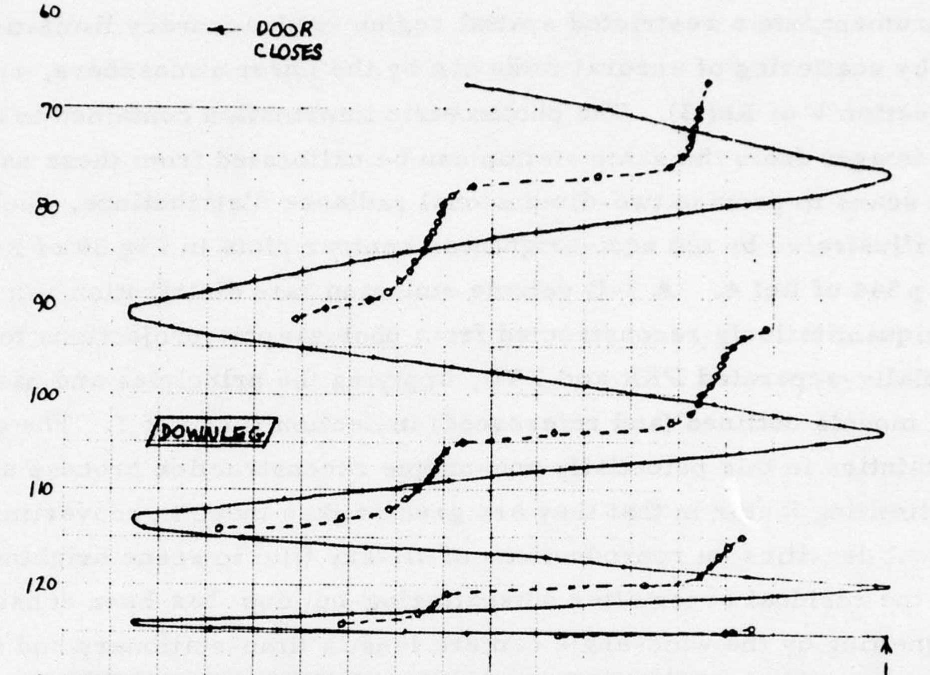

Figure 33. Altitude profiles of elevation and azimuth angles of IC630.02-1A's spectrometer on upleg and downleg.

instrument into a restricted spatial region (with accuracy limitations set by scattering of auroral radiation by the lower atmosphere, reviewed in Section V of Ref 3). The photometric information contained in all-sky images from the same station can be calibrated from these narrow line scans to provide two-dimensional radiance distributions, such as are illustrated by the equi-brightness contour plots in Fig 30 of Ref 1 and p 344 of Ref 4. A 3-D volume emission rate distribution can be semiquantitatively reconstructed from photographic projections to spatially-separated PKR and FYU, applying the principles and particle-flux models outlined (and referenced) in Section II of Ref 1. The uncertainties in this potentially non-unique reconstruction process are the limiting factor, in that they are greater than those in converting optical densities on reproductions of all-sky film to scene brightnesses and the residual error after outscattering-buildup has been considered. (Vignetting by the wide-angle camera lens is time-stationary and thus can be readily corrected, processing of the film can be expected to be reasonably uniform, and procedures are available for correcting for atmospheric scattering to $\lesssim 30\%$ within $\sim 60^{\circ}$ of the zenith.)

These "unfold" principles can be applied to assess the instantaneous emission in the column of the instrument's field of view during specific spectrum scans. With more laborious but still straightforward computations the predosing can also be determined. (The three-dimensional column emission rate data do not lend themselves readily to display, as is evidenced by the attempts in Appendix XVIII of Ref 1, p XVIII-28 in particular.) Some rocket locations-aspects with various physical phenomena in the field – auroral activity, little (as in Fig 34) or no prompt excitation present, and radiations from the lower hemisphere with and without aurora included – are listed in Table 5.

Intensity of the bright moving arc system to the S remained at 100-150 kR 5577Å during most of the flight. When the rocket was near 108 km on upleg (119 sec, in Rotation 1), the west limb of this region, narrow at that time, passed through the instrument's field of

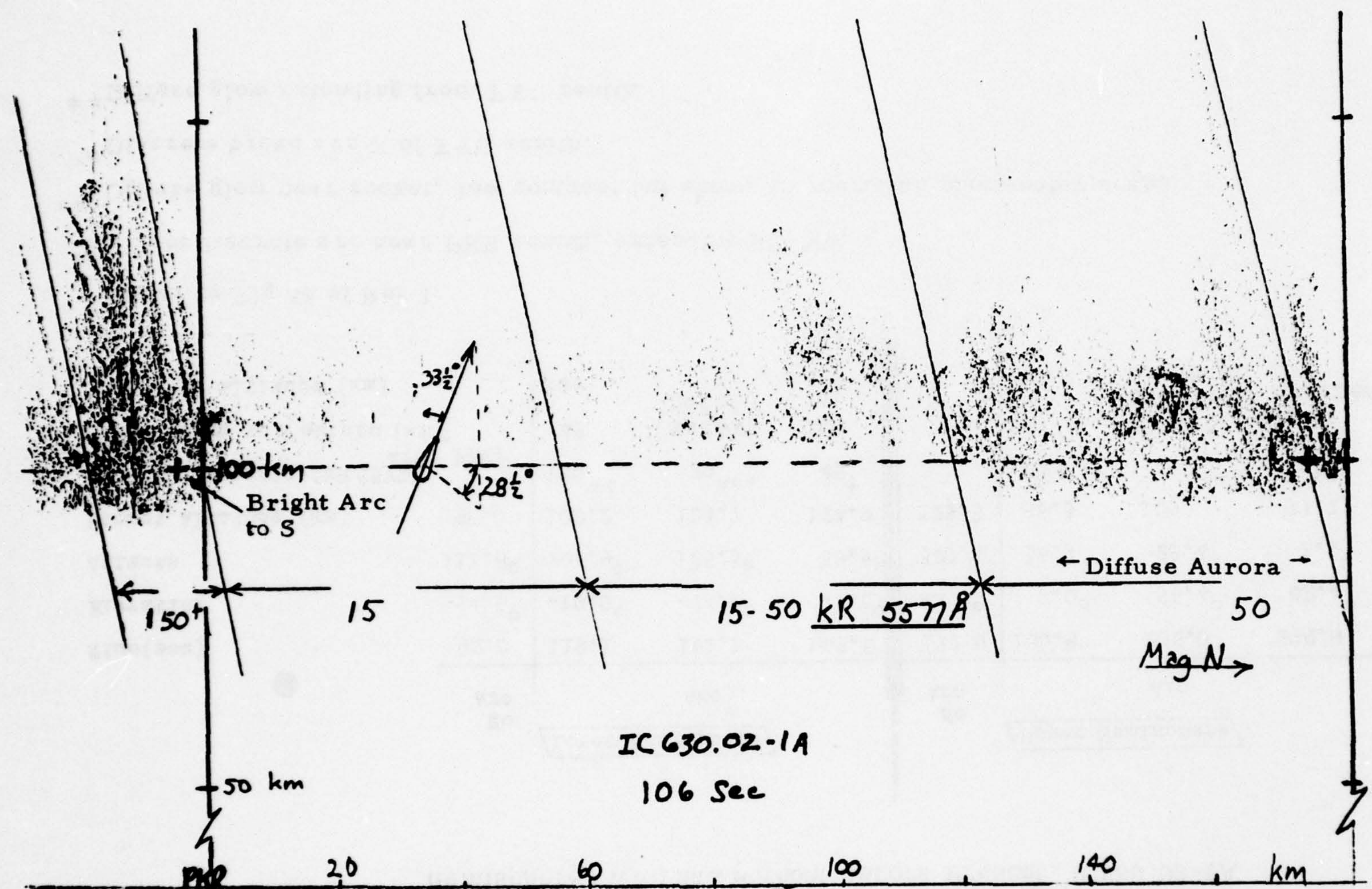

Figure 34. Spectrometer pointing into the upper hemisphere at 106.0 sec (100.0 km, Rotation 1), with approximate intensities in the meridian plane from PKR of the bright arc to the S and diffuse aurora to the N (refer to column 7 of Table 5), IC630.02-1A.

Table 5. Examples of Spectrometer Pointing Into the Upper and Lower Hemispheres With and Without Aurora Present, IC630.02-1A

	Lower Hemisphere				Upper Hemisphere			
	No Arc	Arc*			No Arc	Arc		
Time(sec)	92.8	119.1	161.1	169.6	177.9	100.9	106.0	279.8
Elevation	-74.5°	-10.9°	-74.9°	-5.0°	84.0°	0.0°	56.4°	82.4°
Azimuth	111.8°	206.9°	125.5°	38.5°	320.4°	36.9°	28.4°	1.2°
Rocket Altitude (km)	90.0	108.2	123.7	124.9	125.3	96.3	100	77.7
Auroral Intensity(kR 5577Å from PKR)		150**	20***	45†		60‡	15***	20‡‡
Slant Range to Feature (km)		45	(aurora below)	100		100	(rocket "inside" aurora)	(glow overhead)
Intercept Altitude (km)		100		116		96.3		

----

* Refer to Fig 58 of Ref 3.

** Bright discrete arc near PKR zenith, extending SE-NW.

*** Diffuse glow near rocket, low contrast but shows in meridian photometer scans.

‡ Discrete broad arc N of FYU zenith.

‡‡ Diffuse glow extending from FYU zenith.

view (second entry column in Table 5). The spectrometer's elevation angle was -11°, az was 207°, so that it was intercepting the excited volume ~45 km S near 100 km altitude. Earlier in the spin cycle when the rocket was at 100 km altitude (seventh entry column, and Fig 34), little excitation lay in the field at $33\frac{1}{2}^{\circ}$ zenith angle. In later rotations, the northward movement of the rocket plus southward movement of the excitation results in much less favorable viewing of this intensely-radiating, broadened region; the relative increase in separation causes the spectrometer to point generally below the energy deposition altitudes when its field is directed into the southern sector.

At higher rocket altitudes the spectrometer viewed mostly diffuse (20-45 kR zenith radiance) aurora. Near apogee for example a broad ~20 kR region lay (principally) below the rocket; at 161 sec when the tumbling payload was pointing at -75° eℓ (third entry column) it views this region and the earth's atmosphere-surface. Approximately 9 sec later (fourth column) elevation had increased to -5° at a NE azimuth, placing a distant (~100 km range) 45 kR arc in the field. On downleg, the rocket penetrated a region that had been predosed by Class II+ -III (~50-100 kR) aurora in the period ~5-15 minutes previous. When it reached 80 km, the instantaneous auroral intensity in its zenith was about 20 kR.

As noted above, meridian photometer and all-sky camera data are available for assessing semiquantitatively the prompt and past auroral-particle dosing in the spectrometer's field at these and other rocket aspects/trajectory positions.

SECTION VI

AURORAL INTENSITIES, ICECAP 76 AIRCRAFT PROGRAM

INTRODUCTION

AFGL's IR-Optical Flying Laboratory (USAF NKC-135A S/N 55-3120) performed a series of measurements of the short-wavelength infrared emissions from auroral particle-excited air during the period 22 Feb - 28 Mar 1976, under the program heading ICECAP 76. The principal function of the flight missions is to investigate spatial structure of, and processes leading to, radiation near 2.8μm by the upper atmosphere. The Operating Plan for the flight series is Appendix I of Ref 3, Table I-1 of which lists the characteristics of the radiometers. interferometric spectrometers, photometers, and all-sky camera carried by the aircraft. Other background material on the eight night flights in the auroral zone and the similar set of missions conducted under ICECAP 75 is referenced in Table 6.

This section reports the auroral radiances measured in the moving aircraft's zenith by five channels of the narrow-filter photometer of aircraft system E-05, which is coaligned with the infrared radiometers. Characteristics of this sequentially-sampling, thermoelectrically-cooled instrument are in Table I-2 of Ref 3.

DATA APPLICATION

The air fluorescence-chemiluminescence features reported, and their principal functions in the aircraft program, are

> 4278 Å N_2^+ First Negative (0, 1) band (7.7, 2.4 Å): monitor of column rate of production of ions by incoming charged particles (refer to discussion of the ratio of column intensity to ionization rate in Section V of Ref 3);

Table 6. Reports on ICECAP Aircraft Measurements

1975 Missions	
– Instruments, flight paths, data periods, coordination with PKR facilities	Ref 2, Section V
Results from Flight 75-4 (10 Mar 75)	
– Preliminary assessment	Ref 2, Section III
– Final evaluation	Ref 3, Section IV
1976 Missions	
– Operating Plan	Ref 3, Appendix I
– Instruments, data periods, coordination with DNA 617 radar	Ref 3, Section VI
– Data from Flight 76-9 (07 Mar 76), 2.8μm synthetic spectra & passbands	Ref 4, p 207 ff
– 12-channel photometer data, flight paths	THIS SECTION + APPENDIXES I&II
Synthetic Spectra for NO + OH + thermal radiation, atmosphere transmission	Ref 2, Section I
Optical Method for determining auroral altitudes	Ref 3, Appendix II

5577 Å OI $^1S_0$ - $^1D_2$ forbidden line (7.9, 3.4 Å): second indicator of auroral intensity, with application to energy deposition altitudes;

6300 Å OI $^1D_2$ - $^3P_2$ forbidden line (9.2, 5.5 Å): indicator, when taken with N_2^+ fluorescence, of altitude of peak energy deposition (refer to Appendix II of Ref 3);

5198.7 - 5200.5 Å NI ^2D - ^4S forbidden doublet (8.5, 4.5 Å): precursor of NO^+, measure of buildup of [NO] in the auroral ionosphere;

Continuum near 5312 Å (10.0, 7.1 Å): measure of buildup of [NO] in the auroral ionosphere, and of continuum sky brightness at twilight.

The numbers in parentheses are the full-widths-to-half-maximum-response and area integrals of the individual channel. The absolute calibration procedure includes convolution of the emission feature's spectral shape with that of the sensitivity band as corrected for radiation filling the photometer's 2^o full field of view; refer to Ref 23. Some contribution to the signals in the last two channels from air fluorescence is expected on the basis of experience from auroral flights of this photometer in 1968-72. The data from the N^2D channel, whose sensitivity is shown in Fig 27, are reasonably accurate, as evidenced by the fact that they follow closely the OI red line radiances as expected. The correction for the contribution of the N_2^+ First Negative (0, 3) band, applying the procedure described in Section IV, is 3R/kR 4278 Å band (viewing in the zenith the continuum of Fig 28, if it is indeed a real effect, is not expected to introduce much further error).

The photometer's 12-position filter wheel makes one complete revolution in 24 sec. During this time the aircraft's forward speed advances the fields-of-view, as projected on the typical energy deposition altitude of 100 km, by $\sim 1\frac{1}{2}$ fields. Data from the two additional channels that monitor N_2^+ fluorescence and one sensitive to the 6300 Å line would lower the time resolution for these emission features to 8 or 12 sec respectively. Records are also available

of zenith intensity of the 3466 Å N^2P - ^4S forbidden line, and from the relatively fluorescence-free channel at 5525 Å (9.0, 4.6 Å). The latter data can be applied to extend measurement of 5577 Å aurora-airglow into twilight, and/or measure brightness of the twilight sky (for other than ICECAP auroral missions, as listed in Table 6 of Ref 3).

The forty plots of zenith-sky radiance in the above features - five for each of the seven cross-auroral arc or parallel-arc flights ICECAP 76-3, 4, 5, 6, 9, 10, and 16, plus the Eielson AFB→ Pease AFB ferry flight 76-17, — are in Appendix I. Appendix II is a listing for each of the seventeen 1976 missions of the aircraft's position and heading, altitude, air and ground speed, and outside air temperature, along with the sun's azimuth and elevation angles from the earth's surface below its flight path (prepared by J. Reed, Ref 24). Data periods and other particulars of these missions are in Table 6 of Ref 3.

REDUCTION PROCEDURE

Typical output from the sequentially-sampling photometer is shown in Fig 76 of Ref 3. To access these interlaced channel data, the signal voltages above dark-current level are manually measured from the strip charts and entered by teletype into AFGL's central computer. Also entered is the control information flight number and date, mission type, channel (identified by wavelength) and its calibration factor, and amplifier gain setting. The program that creates the data file is written so that only those values of gain and output voltage that have changed from the previous entry need be entered for each successive data point. An existing PhotoMetrics program then computes and plots the auroral brightnesses in formats such as in Appendix I. The abscissa (time) scale can be readily adjusted for convenient qualitative comparison to similarly-plotted zenith radiance data from the aircraft's infrared radiometers (whose format is shown in Ref's 2 and 4). The visible radiance data are also stored on punched cards to allow ready access for reprinting or further reduction, for example correction of the continuum or N^2D channels for their air fluorescence components.

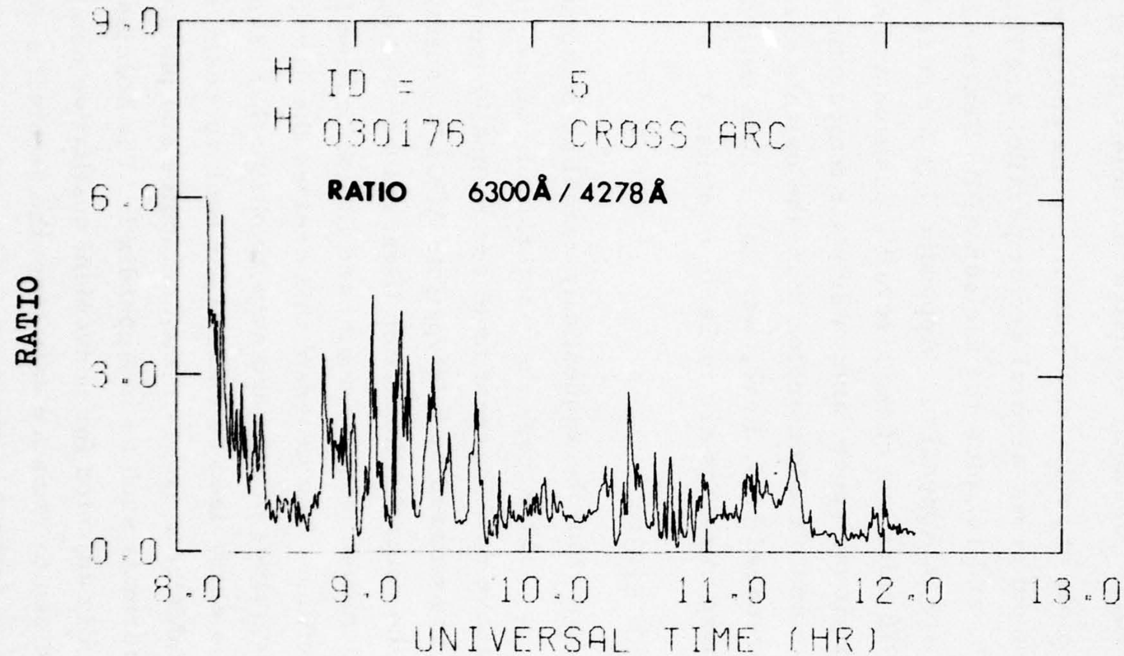

Figure 35. Ratio of column intensities of the OI 6300 Å line to the N_2^+ First Negative (0, 1) band, ICECAP 76-5.

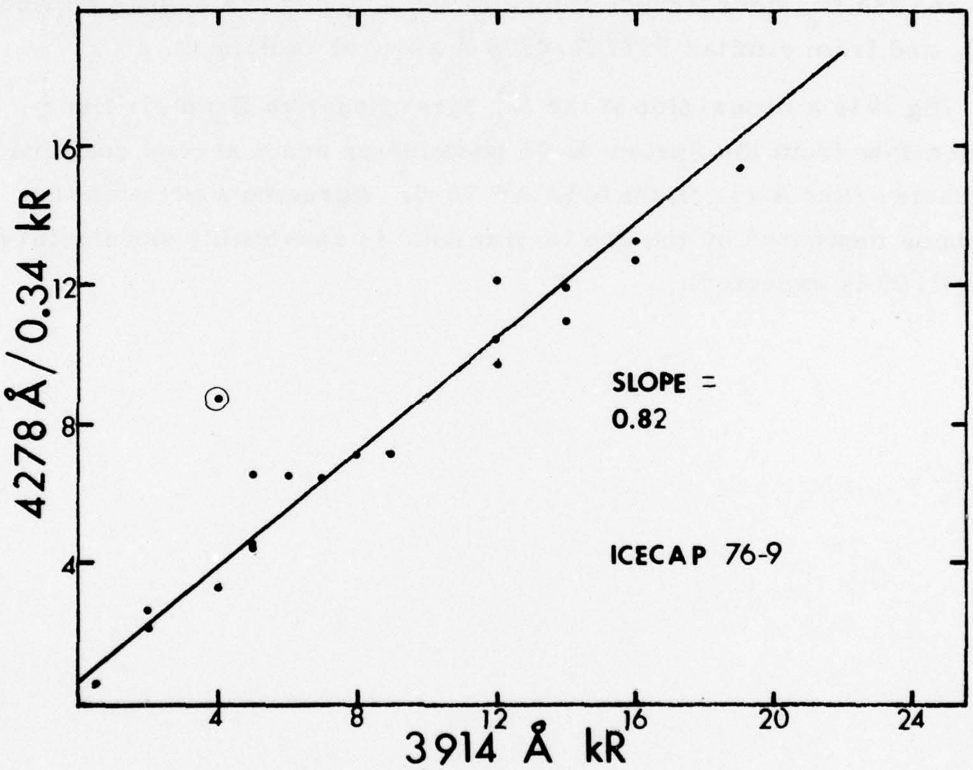

Figure 36. Scatter plot of N_2^+ First Negative fluorescence intensities, with a least-squares fit to the 4278 Å data from the multi-channel photometer. The circled point has been omitted in the fit calculation.

A major such application of these radiances is to computing an altitude profile of volume ionization rate by the primary precipitating electrons, using photon intensity ratios in auroral-emission features (see Appendix II of Ref 3). An example of 6300 Å/4278 Å column ratios from the 1976 data files is shown in Fig 35. A program is being written to calculate directly the altitude of peak energy deposition from this ratio and the N_2^+ fluorescence intensity (on which it has a weak dependence), and from similar 5577 Å-4278 Å auroral radiances.

Fig 36 is a cross-plot of the N_2^+ First Negative Band air fluorescence data from the System E-05 photometer and a second coaligned photometer (Ref 4) in flight ICECAP 76-9. Agreement between the radiances measured by the two instruments is reasonably satisfactory (slope 1.00 is expected).

REFERENCES

1. I. L. Kofsky et al., Data Reduction and Auroral Characterizations for ICECAP, HAES Report No. 4, DNA 3511F (10 Apr 75).

2. I. L. Kofsky, R. B. Sluder, and C. A. Trowbridge, Data Reduction and Auroral Characterizations for ICECAP II, HAES Report No. 27, DNA 3789F (25 Oct 75).

3. I. L. Kofsky, D. P. Villanucci, and R. B. Sluder, Data Reduction and Auroral Characterizations for ICECAP III, HAES Report No. 59, DNA 4220F (31 Jan 77).

4. A. T. Stair, Jr., and J. C. Ulwick (ed's), Proceedings of the HAES Infrared Data Review, AFGL-OP-TM-05, Jun 77.

5. J. B. Kumer, Analysis of 4.3μm ICECAP Data, HAES Report No. 19, AFCRL-TR-74-0334, (Jul 74).

6. Analysis and Simulation Branch AFCRL Computation Center, Aspect Report for Rocket No. A18.219-1, Aspect Report No. 4598, (undated).

7. A. T. Stair, Jr., and R. Nadile (AFGL), private communication (Oct 77).

8. H. Mitchell, 2.8 Micron Emission Further Examination of DNA/AFGL Data and Probable Causes, Unpublished Report (Feb 77).

9. W. F. Grieder and L. A. Whelan, Geometric Aspects of Rocket Photometry, HAES Report No. 41, AFGL-TR-76-0046 (Feb 76).

10. D. A. Burt and C. S. Davis, Rocket Instrumentation for Icecap 73A Auroral Measurements Program - Black Brant 18.205-1, HAES Report No. 3, AFCRL-TR-74-0195 (Feb 74).

11. Reference Atmosphere CIRA 72, Akademie Verlag, Berlin, 1972.

12. M. H. Rees and D. Luckey, J. Geophys. Res. 71, 5181 (1974).

13. J-C. Gerard and O. E. Harang, in Physics and Chemistry of Upper Atmospheres (ed B. McCormac), Reidel, Dordrecht, 1973, p241.

14. R. H. Eather and S. B. Mende, J. Geophys. Res. 76, 1746 (1971).

REFERENCES (continued)

15. R. L. Gattinger and A. Vallance Jones, Can. J. Phys. 52, 2343 (1974).

16. W. R. Pendleton, Jr., and R. R. O'Neil, J. Chem. Phys. 56, 6260 (1972).

17. A. Vallance Jones, Space Sci. Rev's. 11, 826 (1971).

18. H. Nishimura, J. Phys. Soc. Japan 21, 1018 (1966).

19. A. T. Stair, Jr., J. W. Rogers, and W. R. Williamson, Quick Look Data Report - HIRIS Experiment, AFGL-OP-TM-02, 15 Apr 76.

20. G. J. Romick, Report on the Geophysical Description and Available Data Associated with Rocket PF-SGT-116 (IC630.02-1A), HAES Report No. 63, AFGL-TR-77-0073, Mar 77.

21. T. M. Watt, HIRIS Experiment - Chatanika Radar Results, DNA 4229T, Jan 77.

22. Aspect and trajectory listings for IC630.02-1A, from AFGL/OPR (1976).

23. I. L. Kofsky, J. D. Geller, and C. A. Trowbridge, Sky Background Measurement Program, AFCRL-70-0012 (PhM-101-69), 30 Nov 69.

24. J. W. Reed (Visidyne, Inc.), private communication (Sep 77).

APPENDIX I

AURORAL RADIANCES, ICECAP 76 AIRCRAFT MISSIONS

(Refer to Section VI. The mission numbers, at the top of each plot, are identified with flight data and DNA 617 radar coordination in Table 8 of Ref 3.)

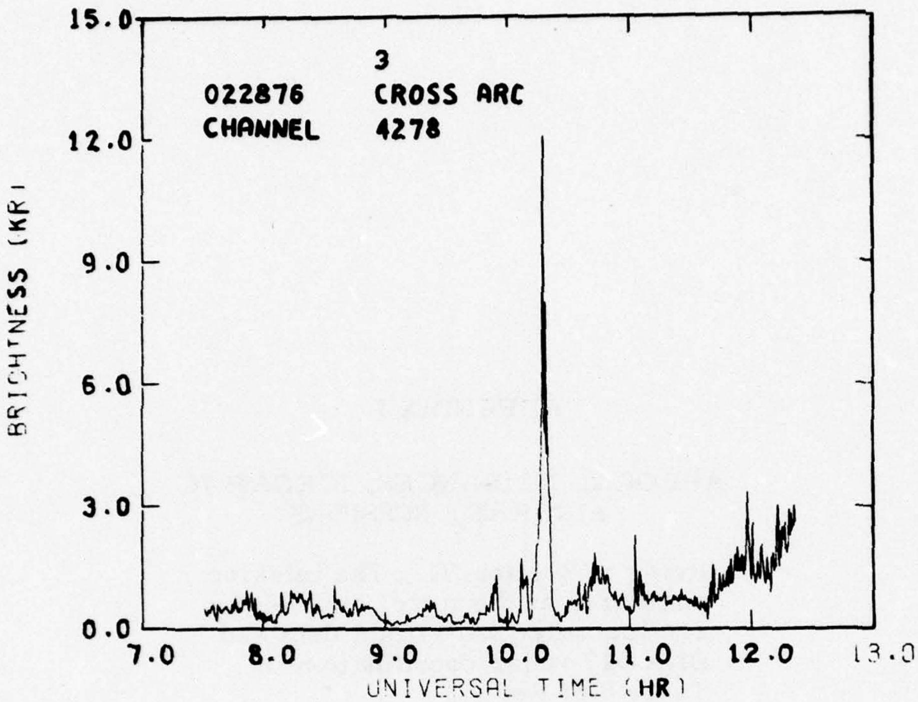
15.0
12.0
9.0
6.0
3.0
0.0
3
022876 CROSS ARC
CHANNEL 4278
BRIGHTNESS (KR)
7.0
8.0
9.0
10.0
11.0
12.0
13.0
UNIVERSAL TIME (HR)

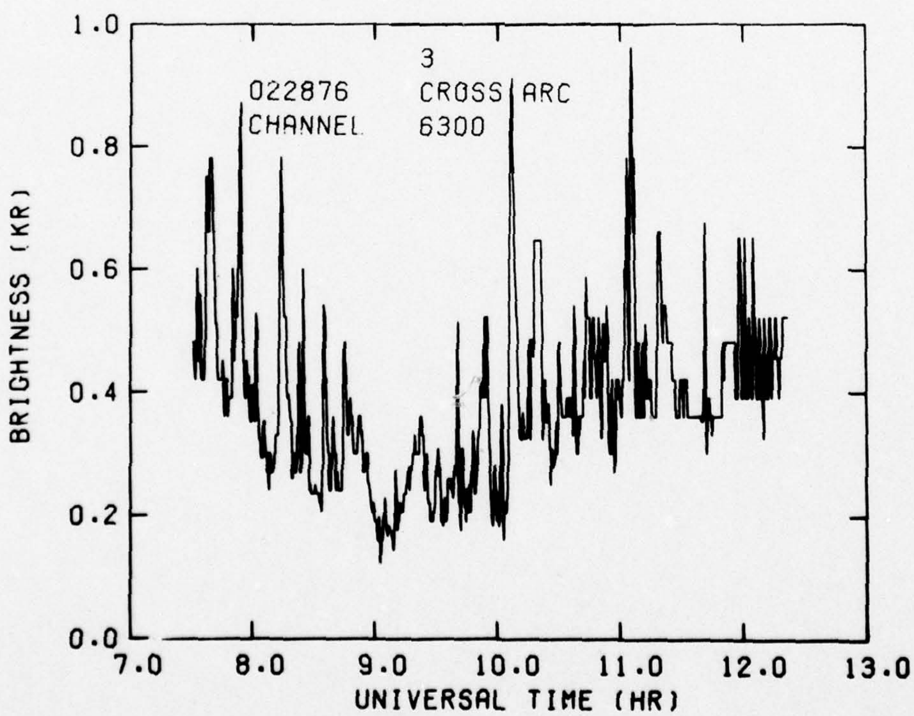
1.0
0.8
0.6
0.4
0.2
0.0
3
022876 CROSS ARC
CHANNEL 6300
BRIGHTNESS (KR)
7.0
8.0
9.0
10.0
11.0
12.0
13.0
UNIVERSAL TIME (HR)

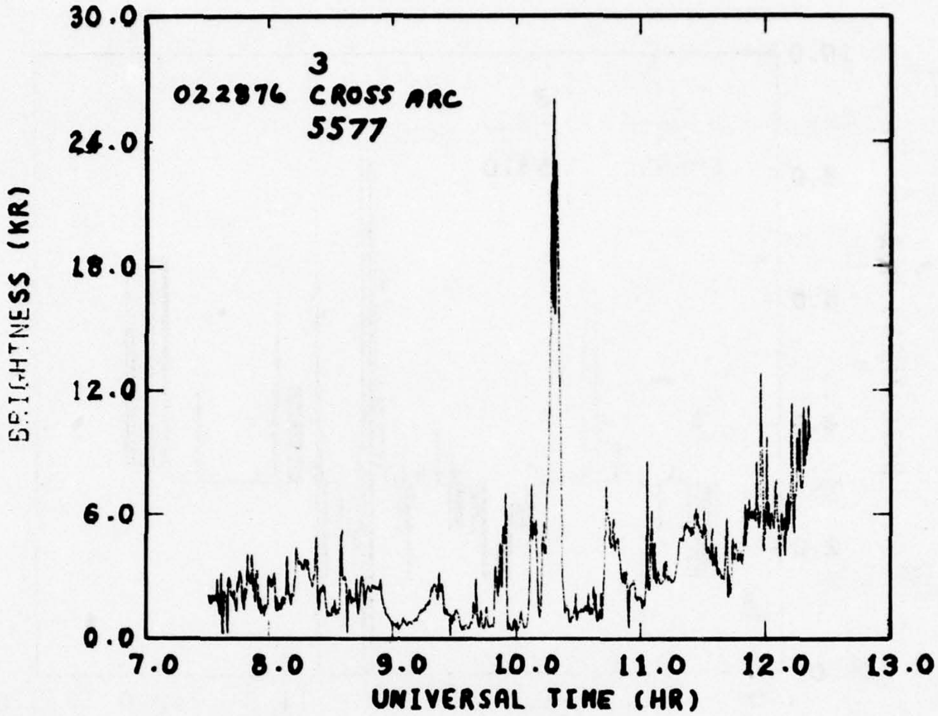
30.0
24.0
18.0
12.0
6.0
0.0
3
022876 CROSS ARC
5577
BRIGHTNESS (KR)
7.0
8.0
9.0
10.0
11.0
12.0
13.0
UNIVERSAL TIME (HR)

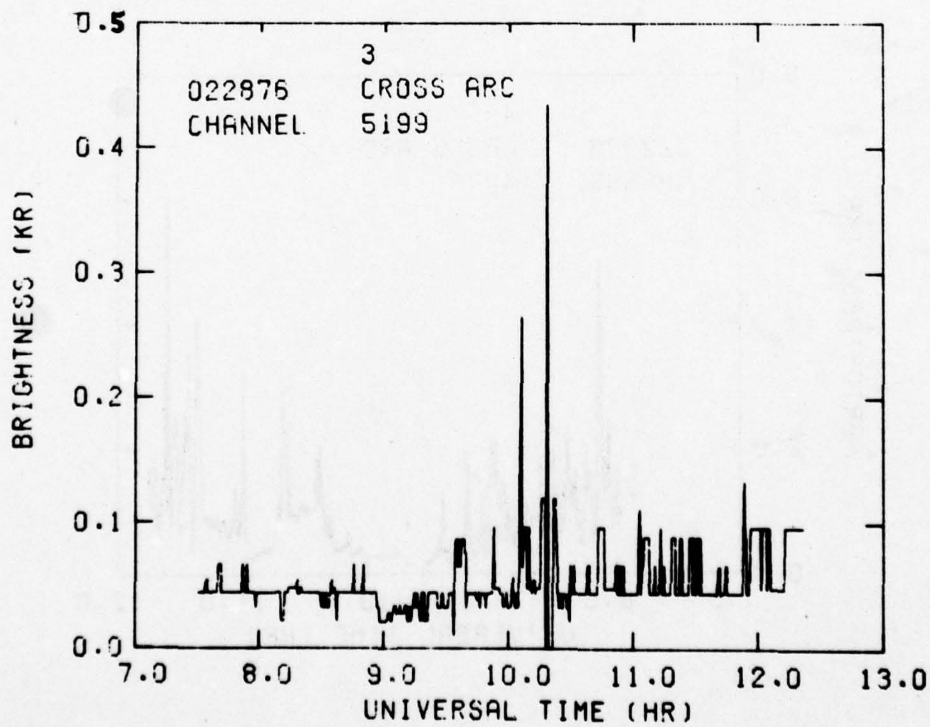
0.5
0.4
0.3
0.2
0.1
0.0
3
022876 CROSS ARC
CHANNEL 5199
BRIGHTNESS (KR)
7.0
8.0
9.0
10.0
11.0
12.0
13.0
UNIVERSAL TIME (HR)

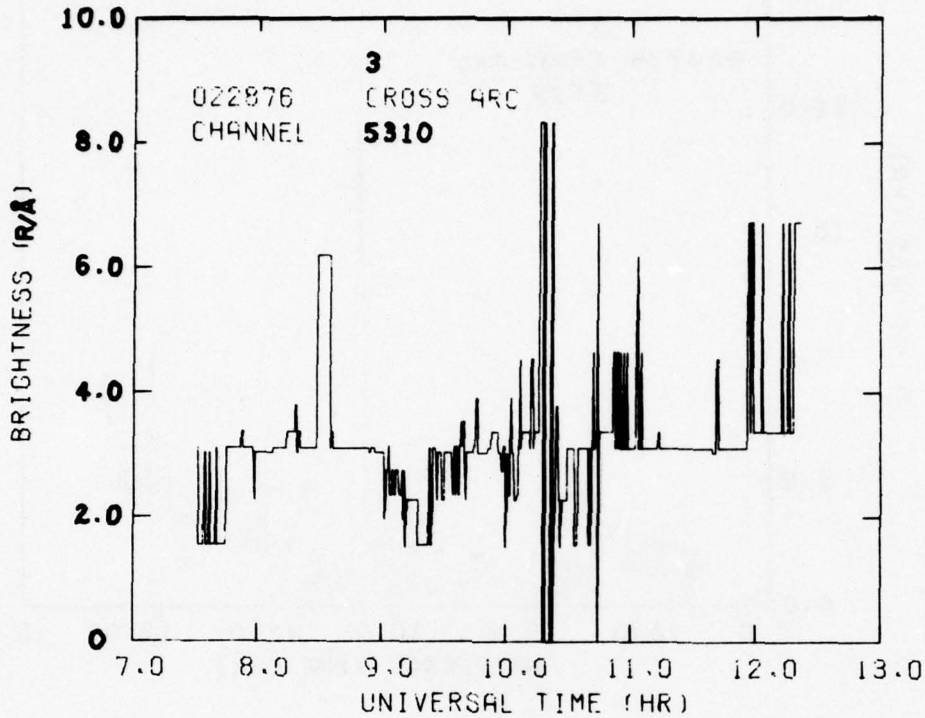
3
022876 CROSS ARC
CHANNEL 5310
BRIGHTNESS (R/Å)
10.0
8.0
6.0
4.0
2.0
0
7.0
8.0
9.0
10.0
11.0
12.0
13.0
UNIVERSAL TIME (HR)

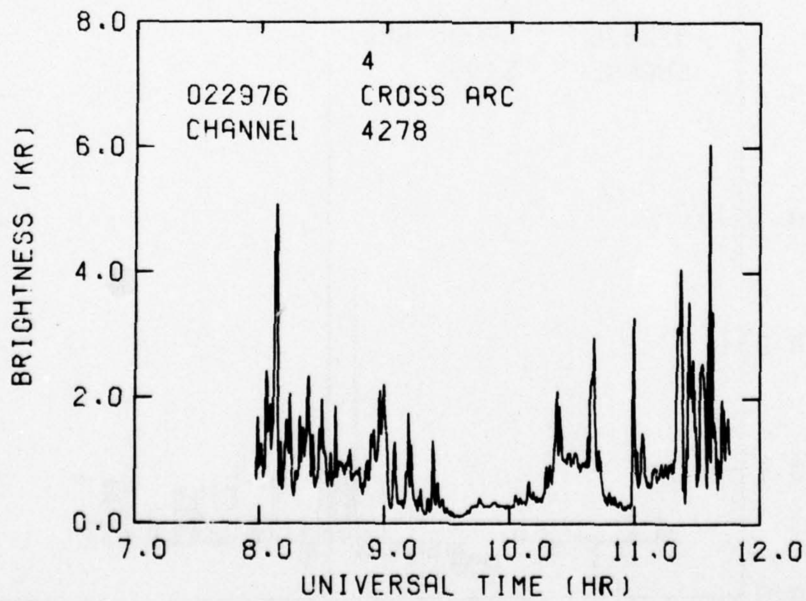
4
022976 CROSS ARC
CHANNEL 4278
BRIGHTNESS (KR)
8.0
6.0
4.0
2.0
0.0
7.0
8.0
9.0
10.0
11.0
12.0
UNIVERSAL TIME (HR)

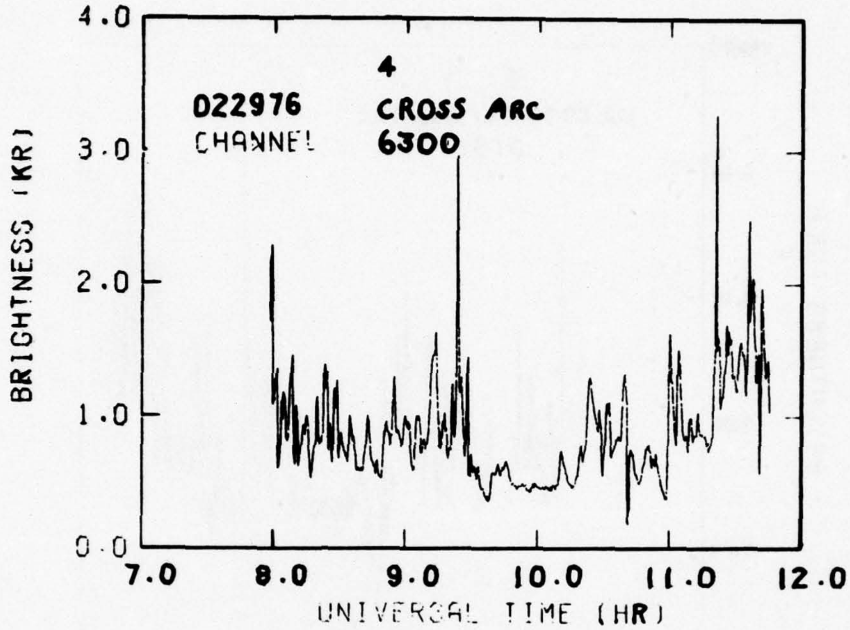
4
022976 CROSS ARC
CHANNEL 6300
BRIGHTNESS (KR)
4.0
3.0
2.0
1.0
0.0
7.0
8.0
9.0
10.0
11.0
12.0
UNIVERSAL TIME (HR)

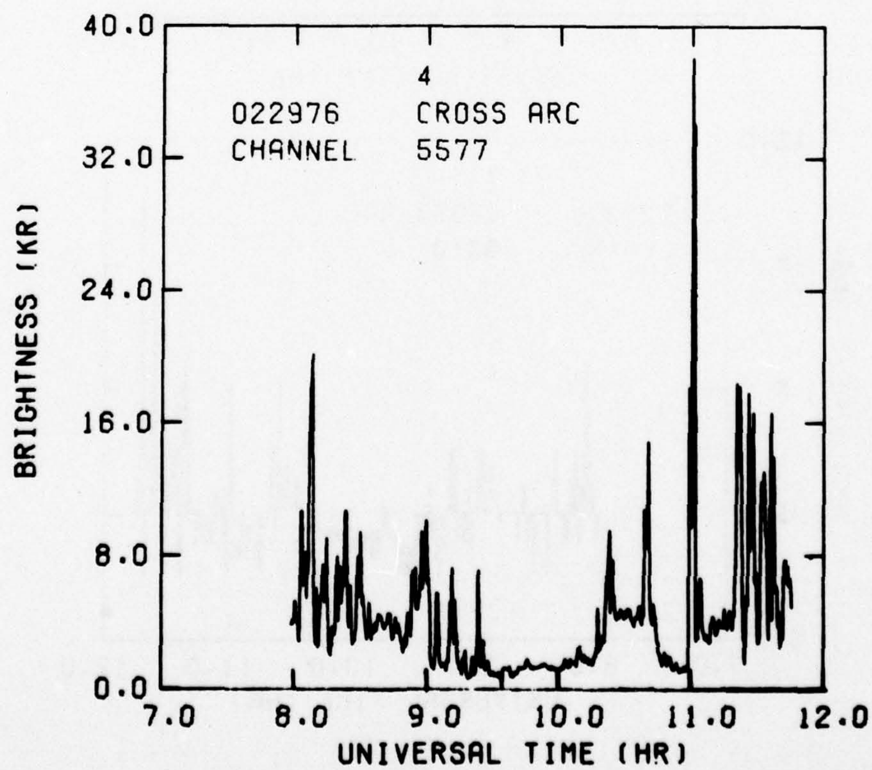
4
022976 CROSS ARC
CHANNEL 5577
BRIGHTNESS (KR)
40.0
32.0
24.0
16.0
8.0
0.0
7.0
8.0
9.0
10.0
11.0
12.0
UNIVERSAL TIME (HR)

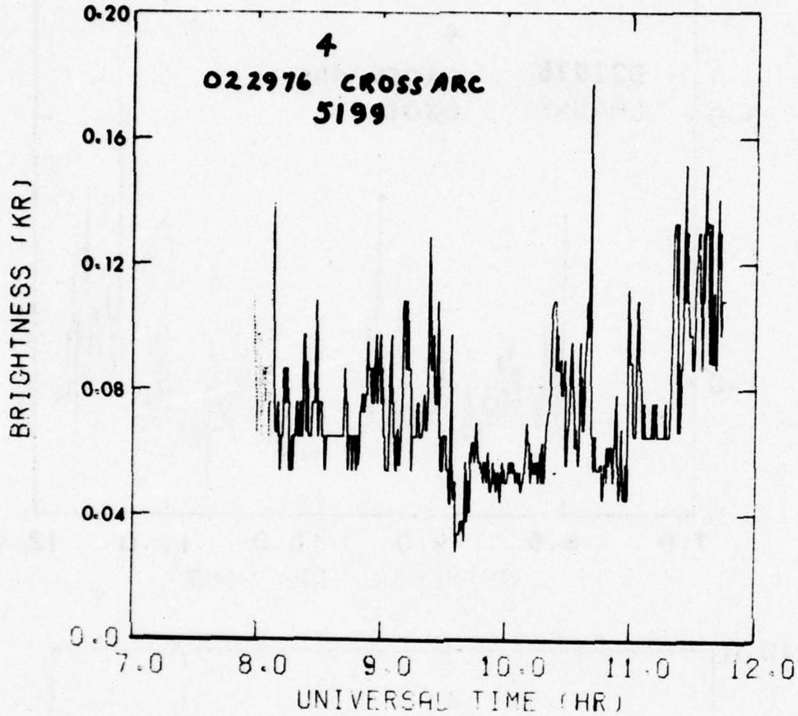
4
022976 CROSS ARC
5199
BRIGHTNESS (KR)
0.20
0.16
0.12
0.08
0.04
0.0
7.0
8.0
9.0
10.0
11.0
12.0
UNIVERSAL TIME (HR)

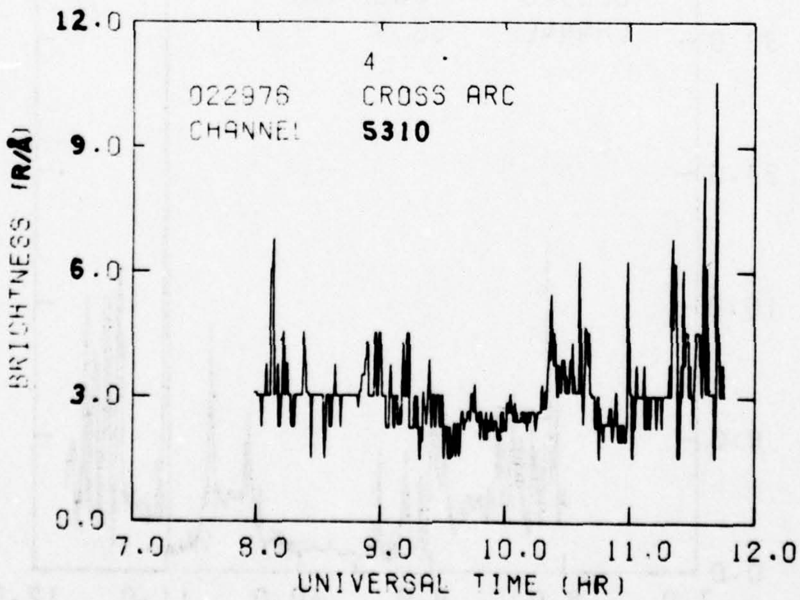
4
022976 CROSS ARC
CHANNEL 5310
BRIGHTNESS (R/Å)
12.0
9.0
6.0
3.0
0.0
7.0
8.0
9.0
10.0
11.0
12.0
UNIVERSAL TIME (HR)

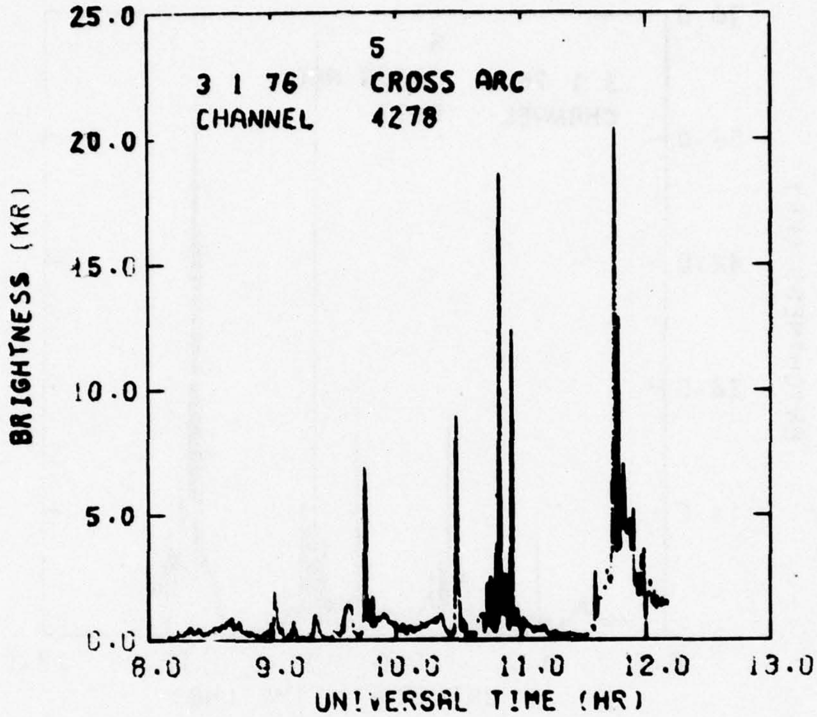
25.0
20.0
15.0
10.0
5.0
0.0
5
3 1 76
CROSS ARC
CHANNEL
4278
BRIGHTNESS (KR)
8.0
9.0
10.0
11.0
12.0
13.0
UNIVERSAL TIME (HR)

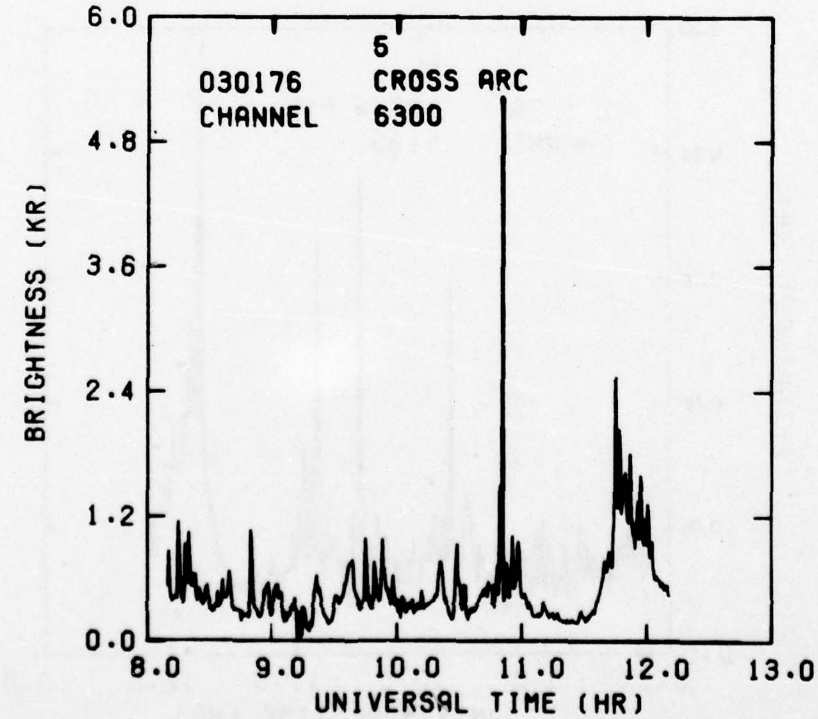
6.0
4.8
3.6
2.4
1.2
0.0
5
030176
CROSS ARC
CHANNEL
6300
BRIGHTNESS (KR)
8.0
9.0
10.0
11.0
12.0
13.0
UNIVERSAL TIME (HR)

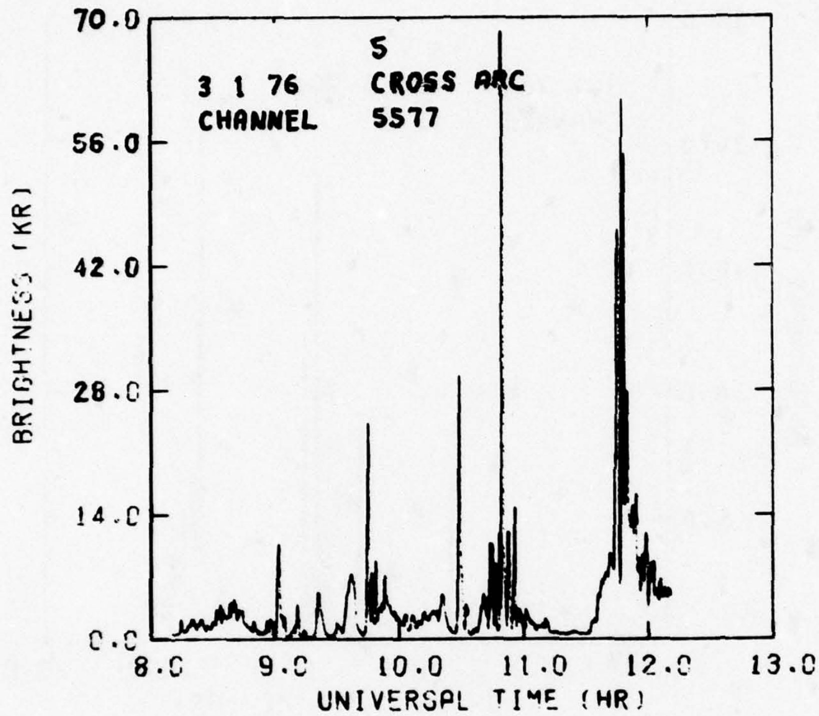

5
3 1 76
CHANNEL
CROSS ARC
5577
BRIGHTNESS (KR)
UNIVERSAL TIME (HR)

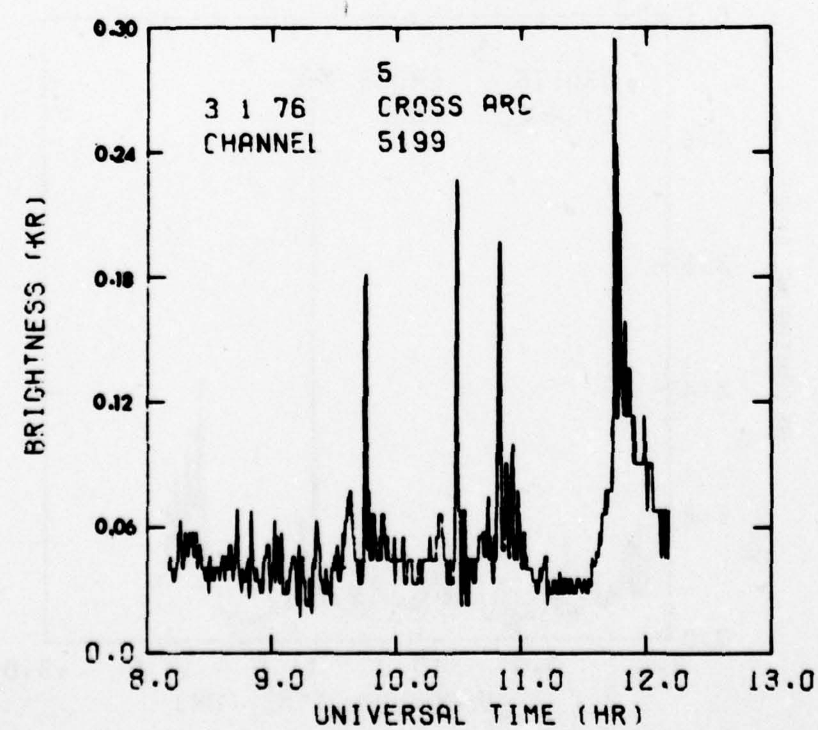

5
3 1 76
CHANNEL
CROSS ARC
5199
BRIGHTNESS (KR)
UNIVERSAL TIME (HR)

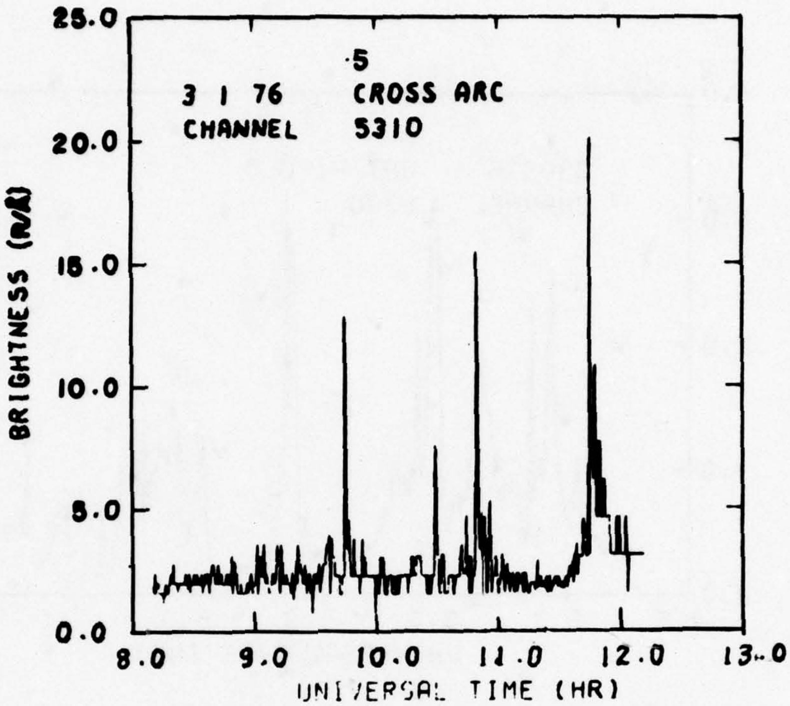

5
3 1 76
CROSS ARC
CHANNEL
5310
BRIGHTNESS (KR)
UNIVERSAL TIME (HR)
25.0
20.0
15.0
10.0
5.0
0.0
8.0
9.0
10.0
11.0
12.0
13.0

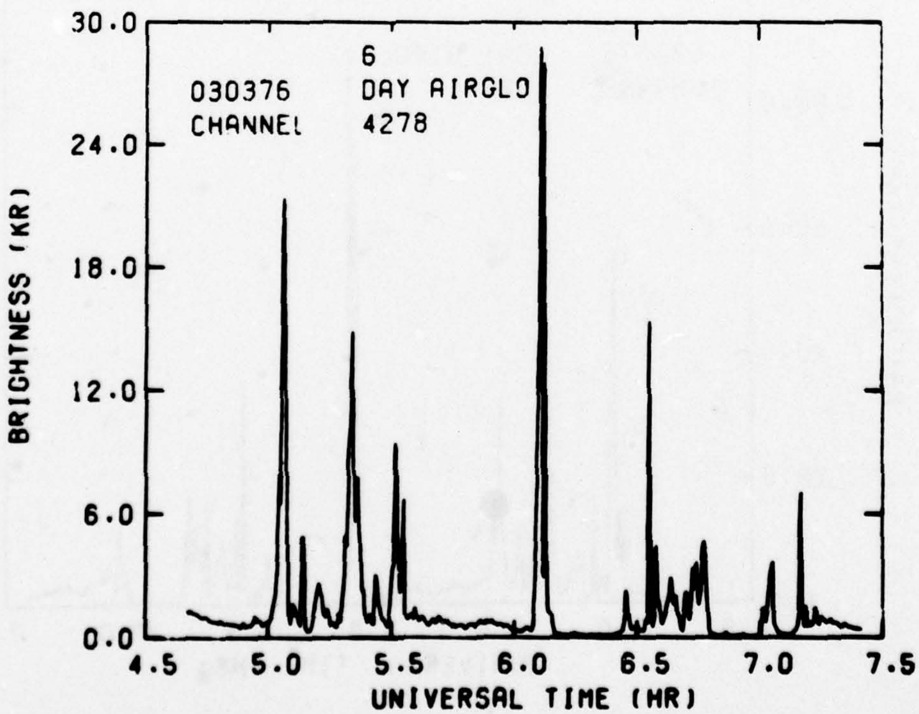

6
030376
DAY AIRGLO
CHANNEL
4278
BRIGHTNESS (KR)
UNIVERSAL TIME (HR)
30.0
24.0
18.0
12.0
6.0
0.0
4.5
5.0
5.5
6.0
6.5
7.0
7.5

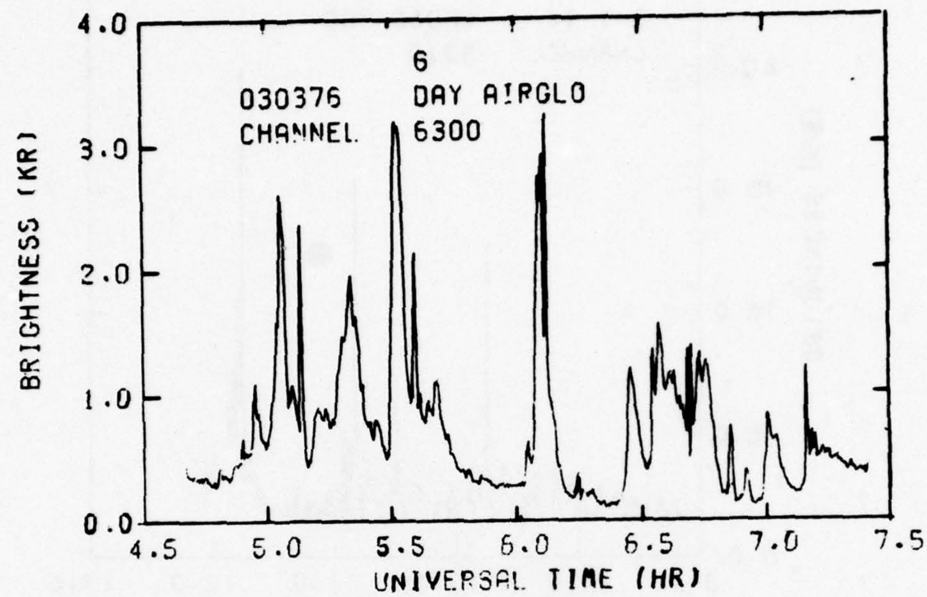

6
030376
CHANNEL
DAY AIRGLO
6300
BRIGHTNESS (KR)
UNIVERSAL TIME (HR)

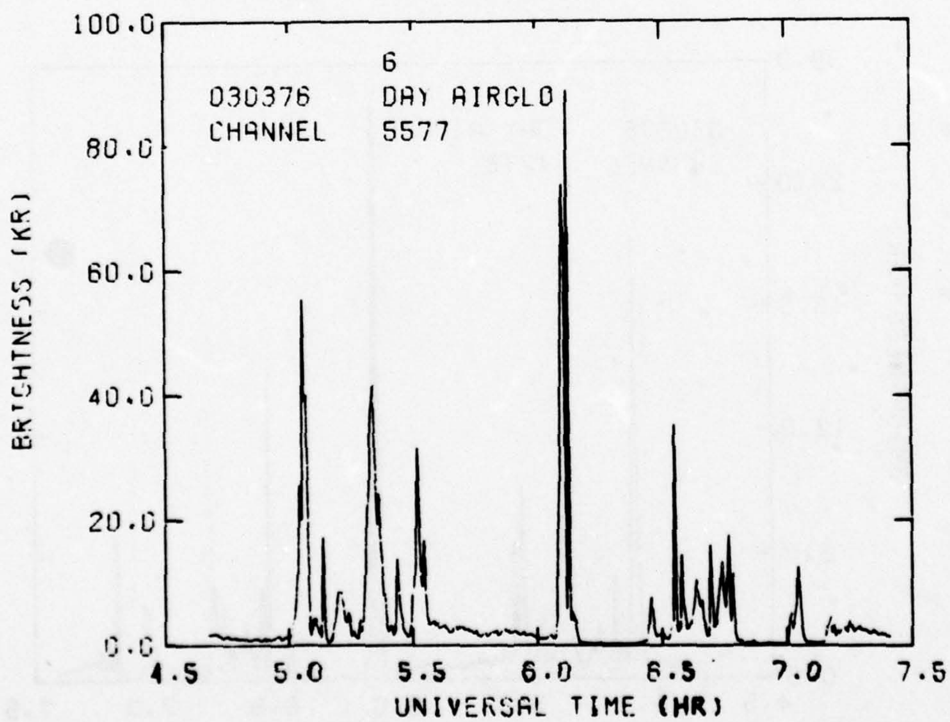

6
030376
CHANNEL
DAY AIRGLO
5577
BRIGHTNESS (KR)
UNIVERSAL TIME (HR)

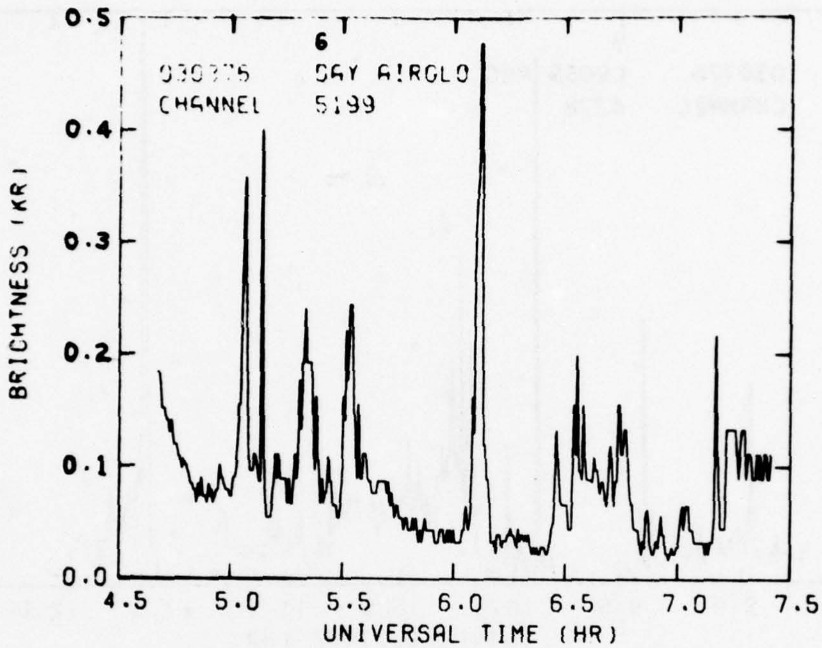
6
DAY AIRGLO
CHANNEL
5199
BRIGHTNESS (KR)
0.5
0.4
0.3
0.2
0.1
0.0
4.5
5.0
5.5
6.0
6.5
7.0
7.5
UNIVERSAL TIME (HR)

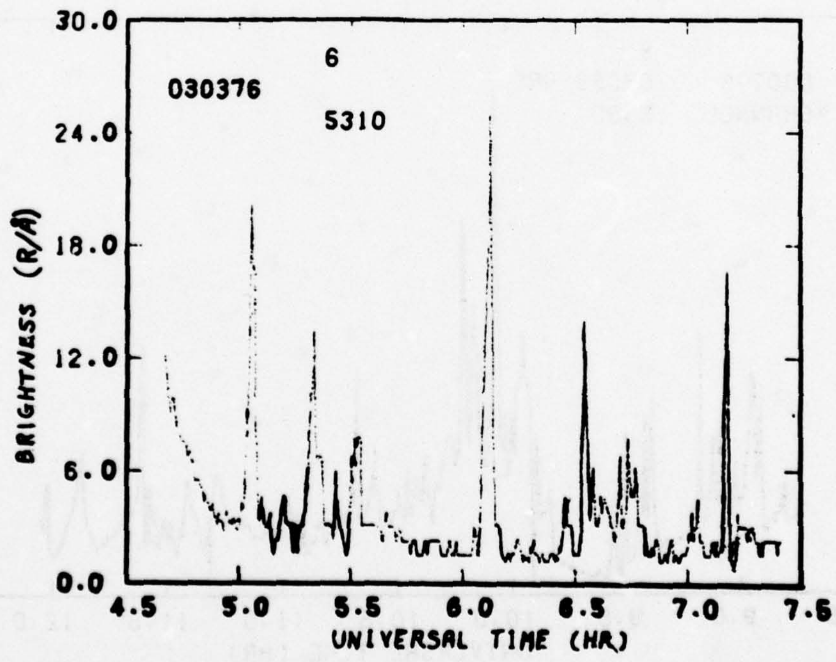
6
030376
5310
BRIGHTNESS (R/Å)
30.0
24.0
18.0
12.0
6.0
0.0
4.5
5.0
5.5
6.0
6.5
7.0
7.5
UNIVERSAL TIME (HR)

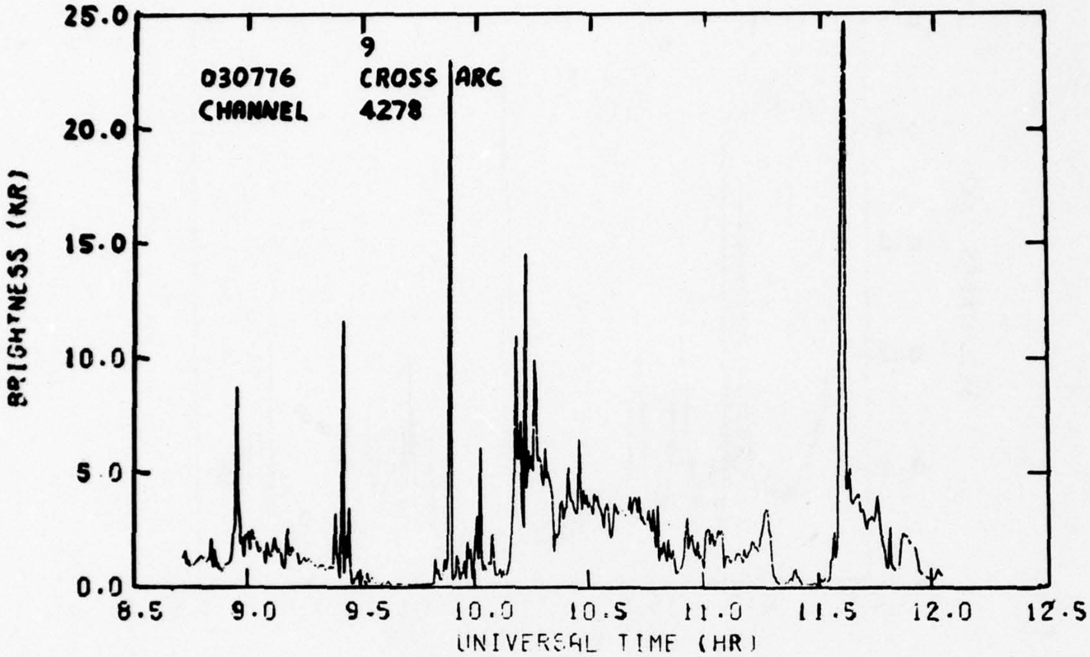

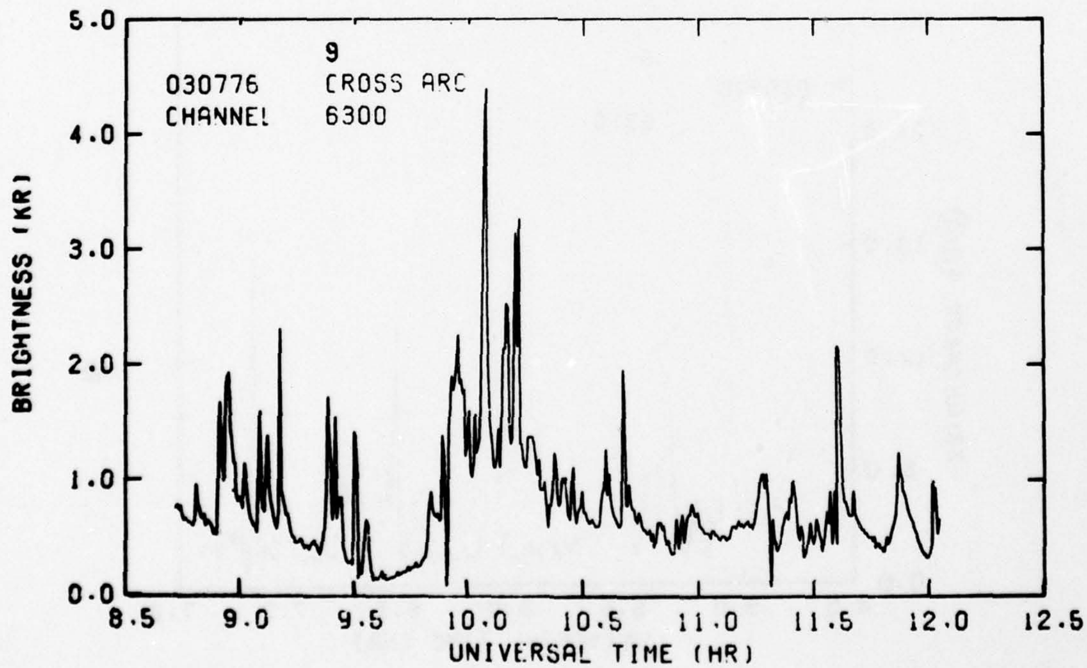

THIS PAGE IS BEST QUALITY PRACTICABLE
FROM COPY FURNISHED TO DDC

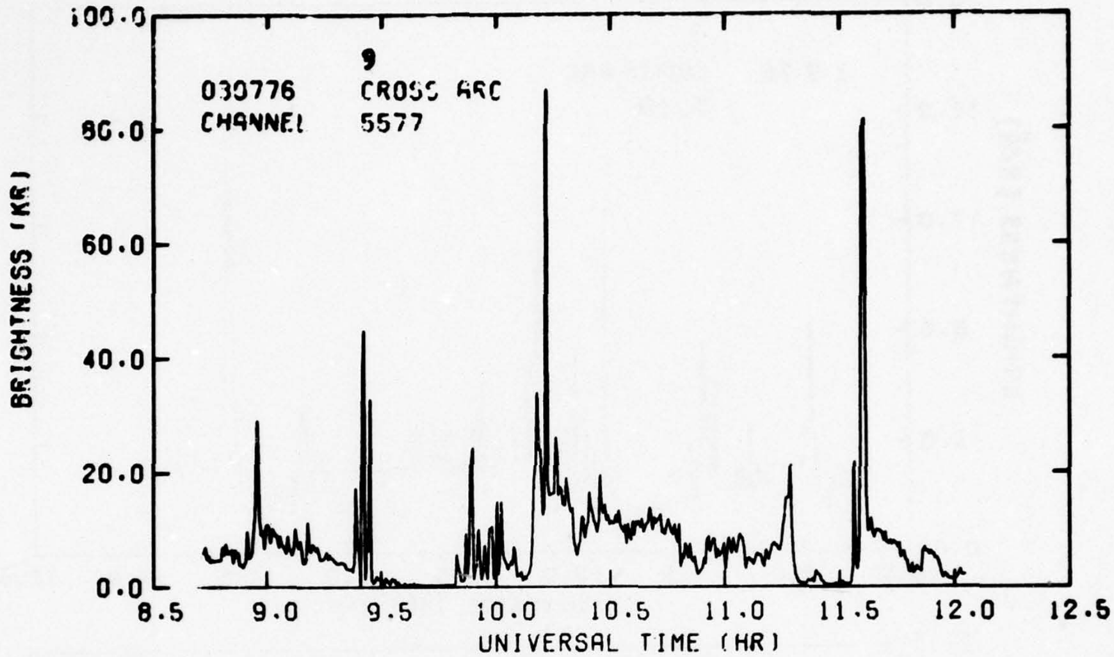

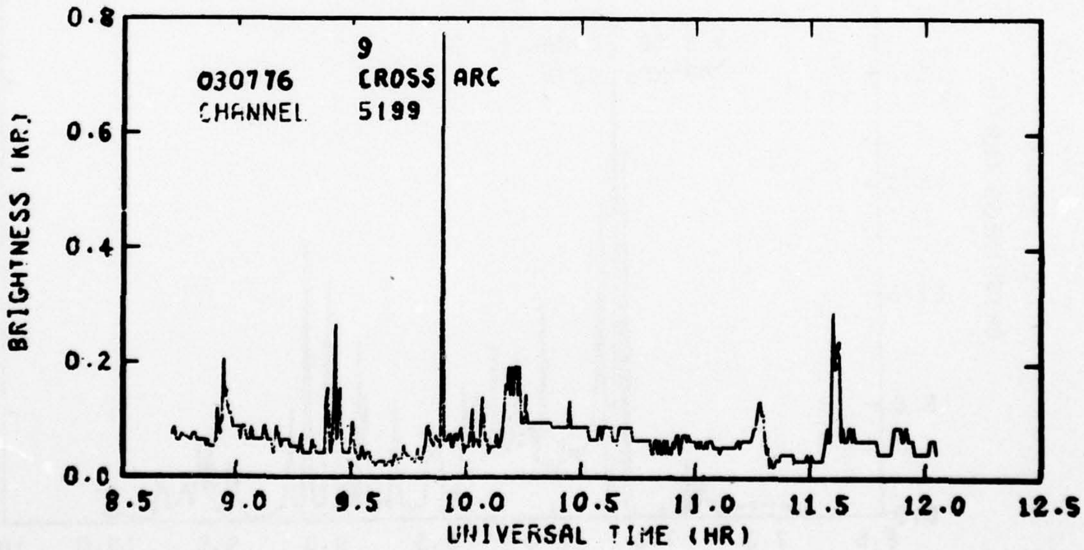

THIS PAGE IS BEST QUALITY PRACTICABLE
FROM COPY FURNISHED TO DDC

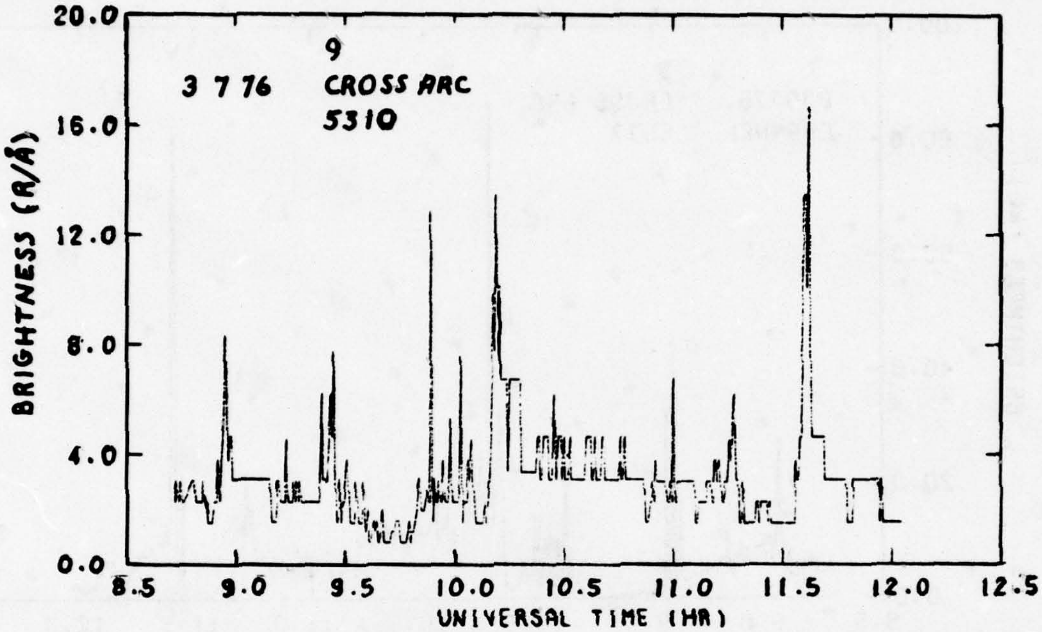
9
3 7 76
CROSS ARC
5310
BRIGHTNESS (R/Å)
UNIVERSAL TIME (HR)

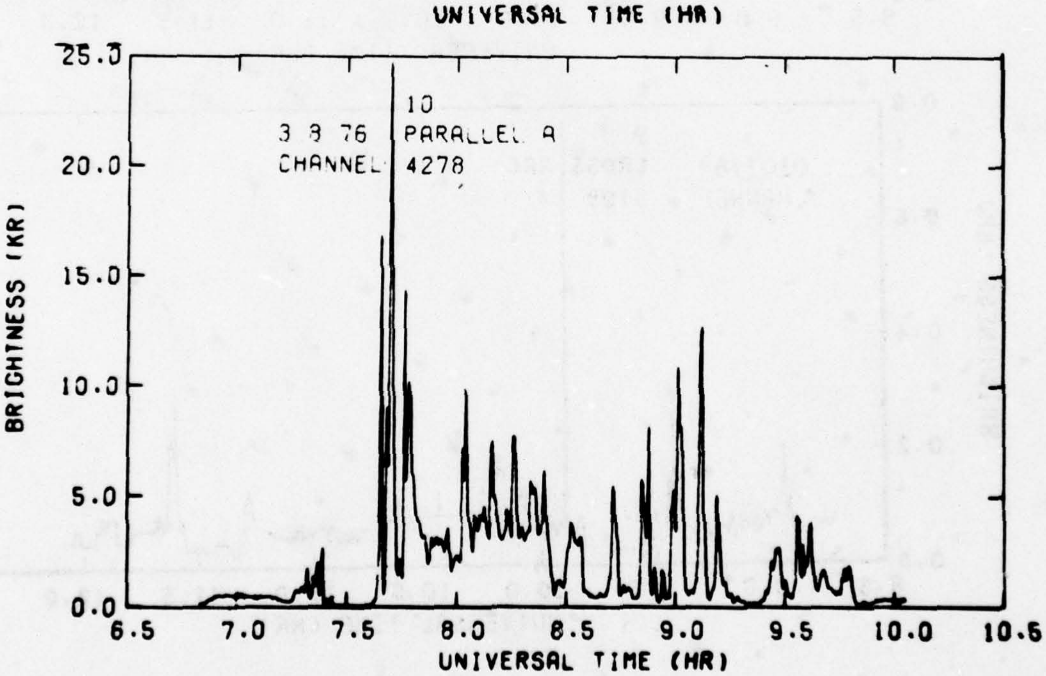
10
3 8 76
PARALLEL A
CHANNEL 4278
BRIGHTNESS (KR)
UNIVERSAL TIME (HR)

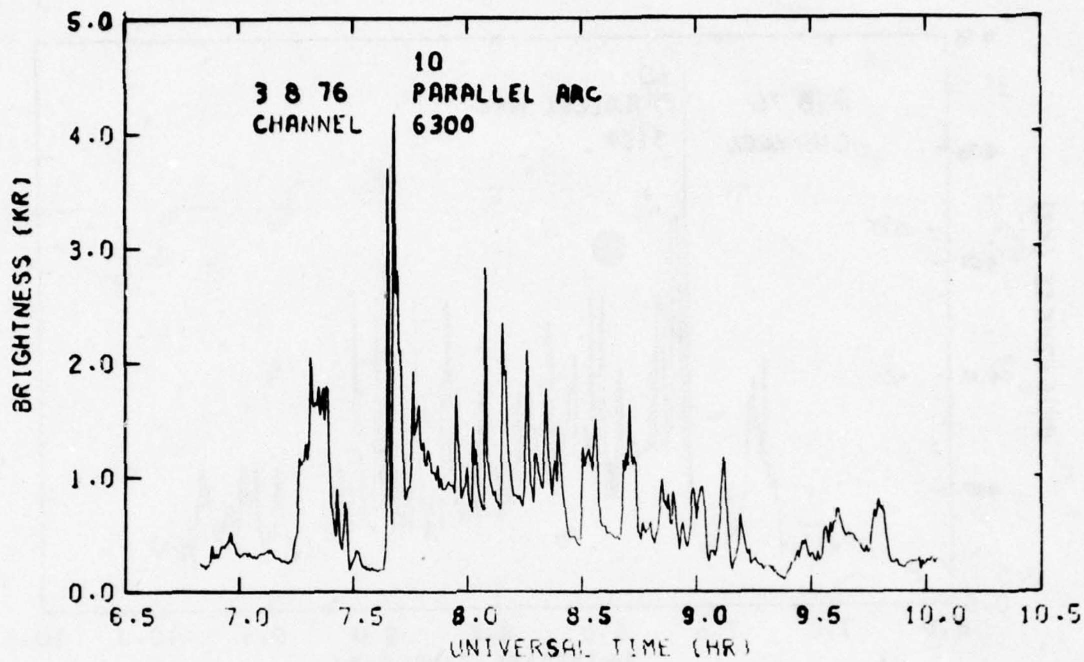
3 8 76
CHANNEL
10
PARALLEL ARC
6300
BRIGHTNESS (KR)
UNIVERSAL TIME (HR)
0.0
1.0
2.0
3.0
4.0
5.0
6.5
7.0
7.5
8.0
8.5
9.0
9.5
10.0
10.5

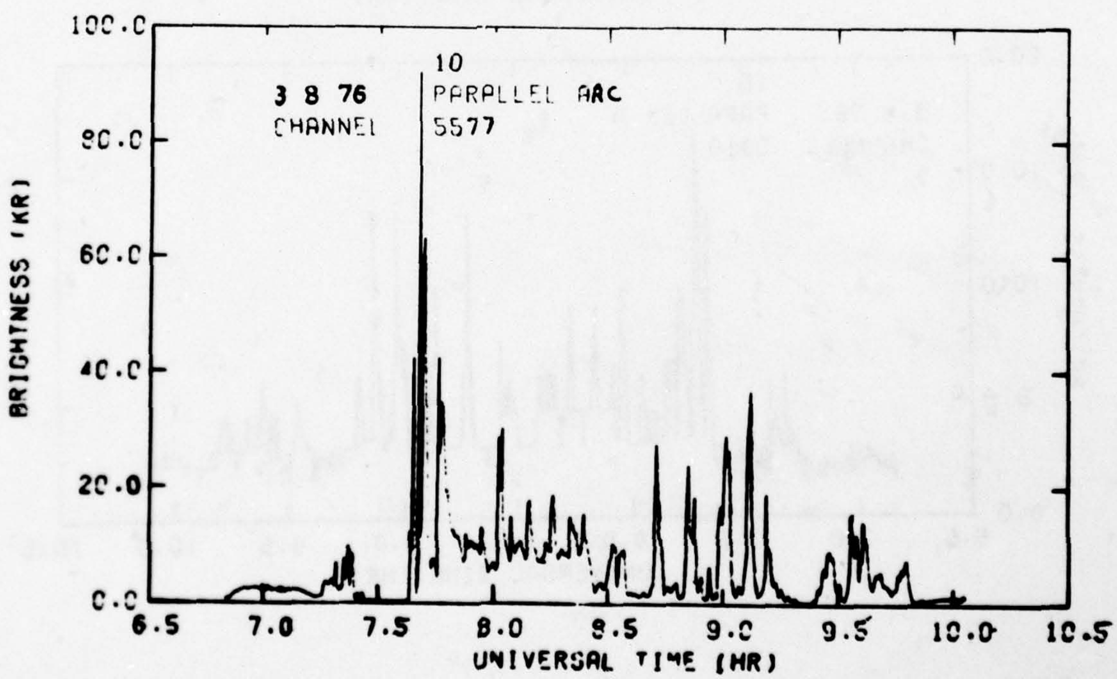
3 8 76
CHANNEL
10
PARALLEL ARC
5577
BRIGHTNESS (KR)
UNIVERSAL TIME (HR)
0.0
20.0
40.0
60.0
80.0
100.0
6.5
7.0
7.5
8.0
8.5
9.0
9.5
10.0
10.5

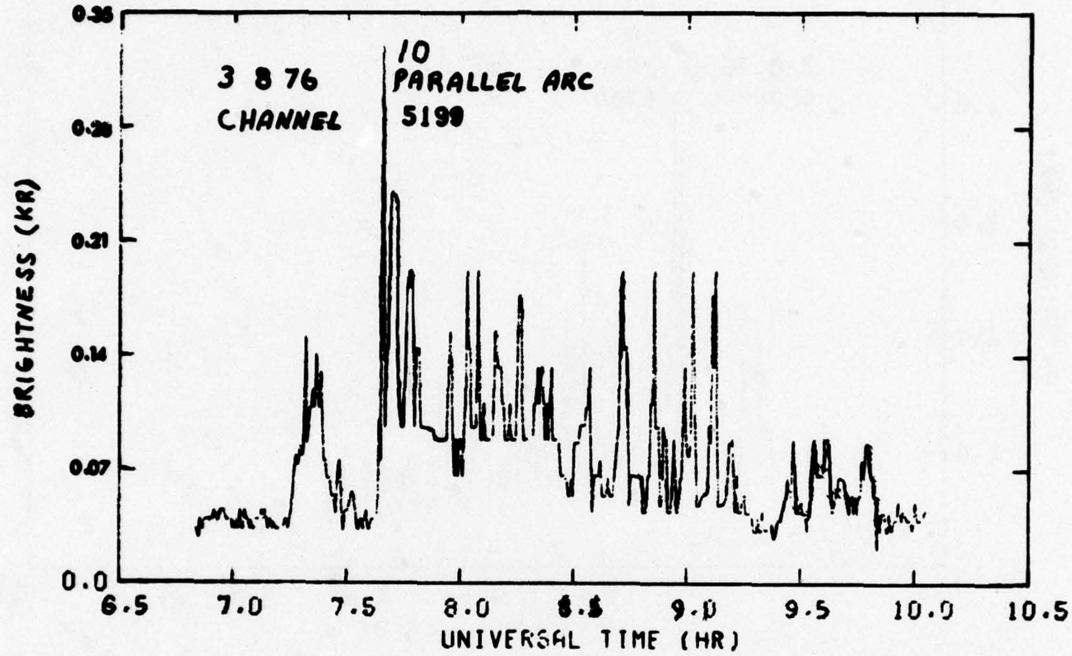
3 8 76
CHANNEL
10
PARALLEL ARC
5199
BRIGHTNESS (KR)
0.07
0.14
0.21
0.0
6.5
7.0
7.5
8.0
9.0
9.5
10.0
10.5
UNIVERSAL TIME (HR)

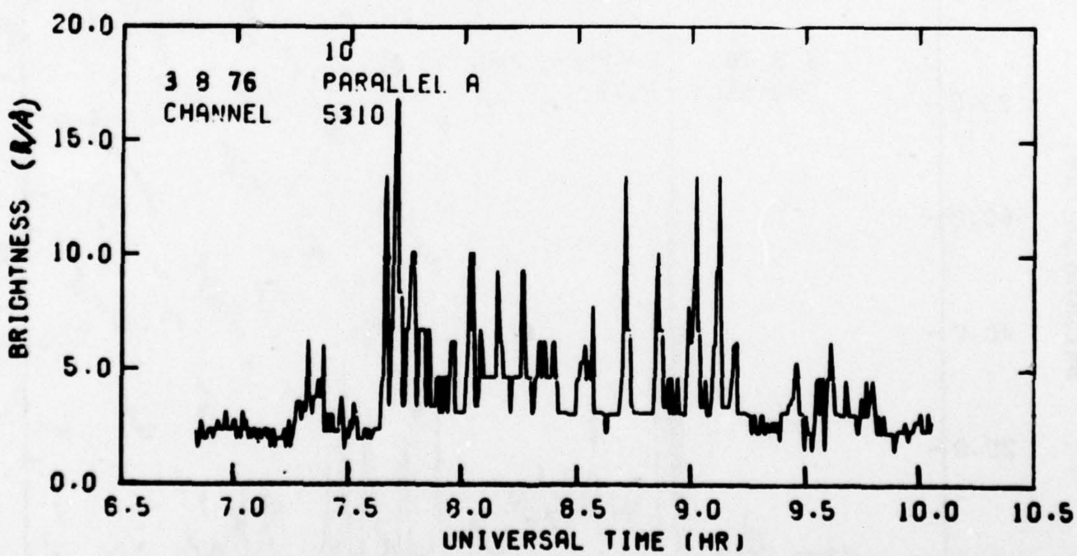
3 8 76
CHANNEL
10
PARALLEL A
5310
BRIGHTNESS
20.0
15.0
10.0
5.0
0.0
6.5
7.0
7.5
8.0
8.5
9.0
9.5
10.0
10.5
UNIVERSAL TIME (HR)

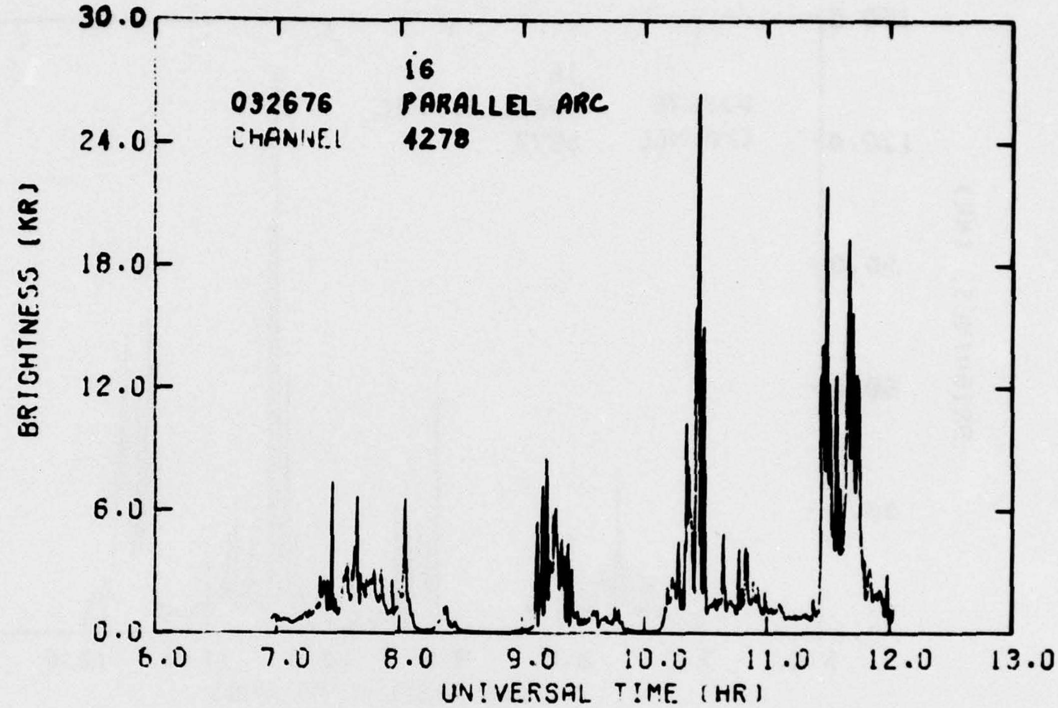

16
032676
CHANNEL
PARALLEL ARC
4278
BRIGHTNESS (KR)
30.0
24.0
18.0
12.0
6.0
0.0
6.0
7.0
8.0
9.0
10.0
11.0
12.0
13.0
UNIVERSAL TIME (HR)

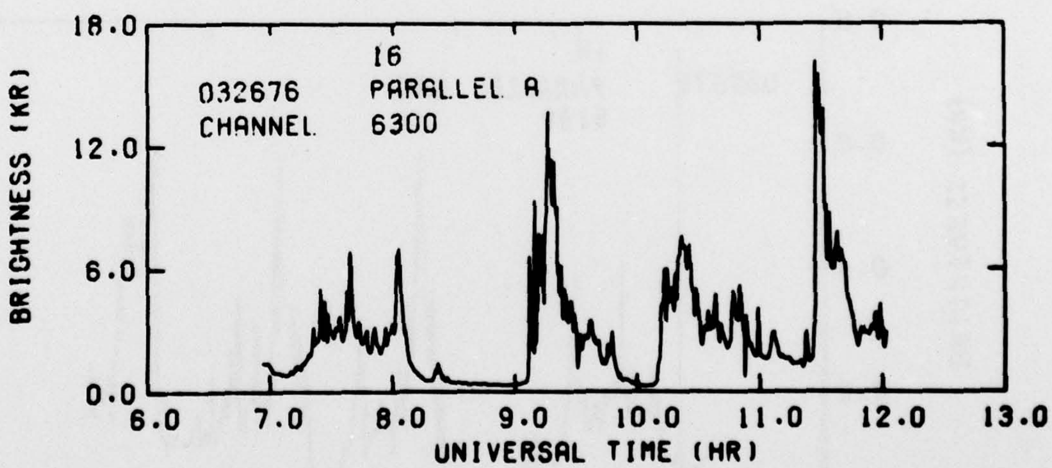

16
032676
CHANNEL
PARALLEL A
6300
BRIGHTNESS (KR)
18.0
12.0
6.0
0.0
6.0
7.0
8.0
9.0
10.0
11.0
12.0
13.0
UNIVERSAL TIME (HR)

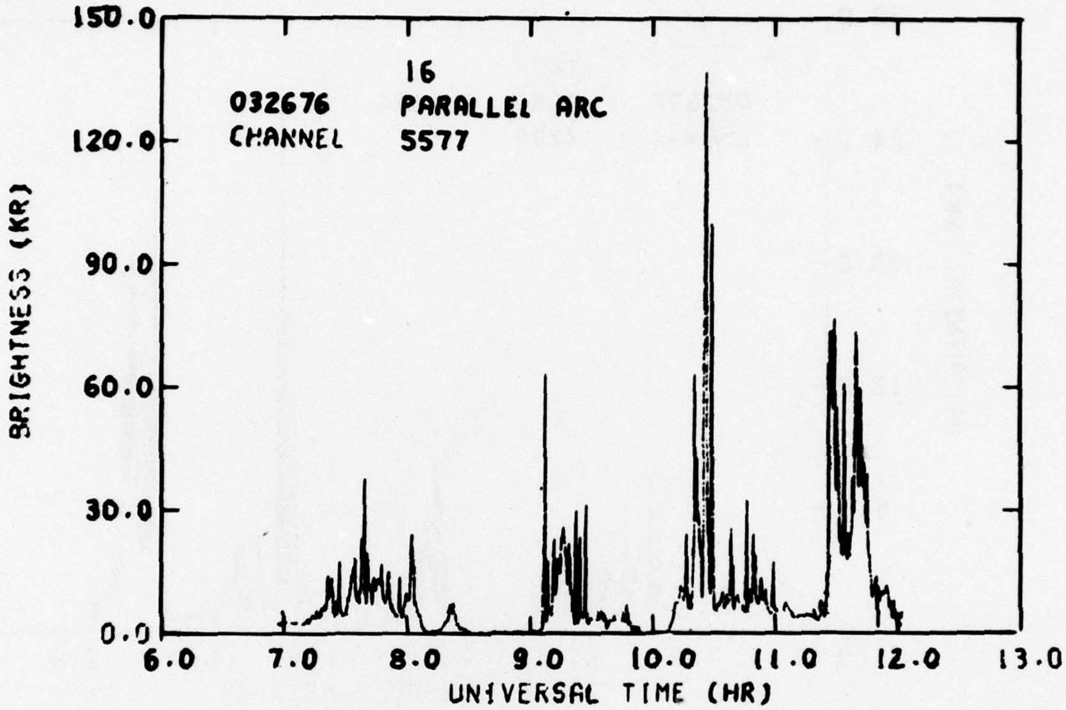
16
032676
PARALLEL ARC
CHANNEL
5577
150.0
120.0
90.0
60.0
30.0
0.0
BRIGHTNESS (KR)
6.0
7.0
8.0
9.0
10.0
11.0
12.0
13.0
UNIVERSAL TIME (HR)

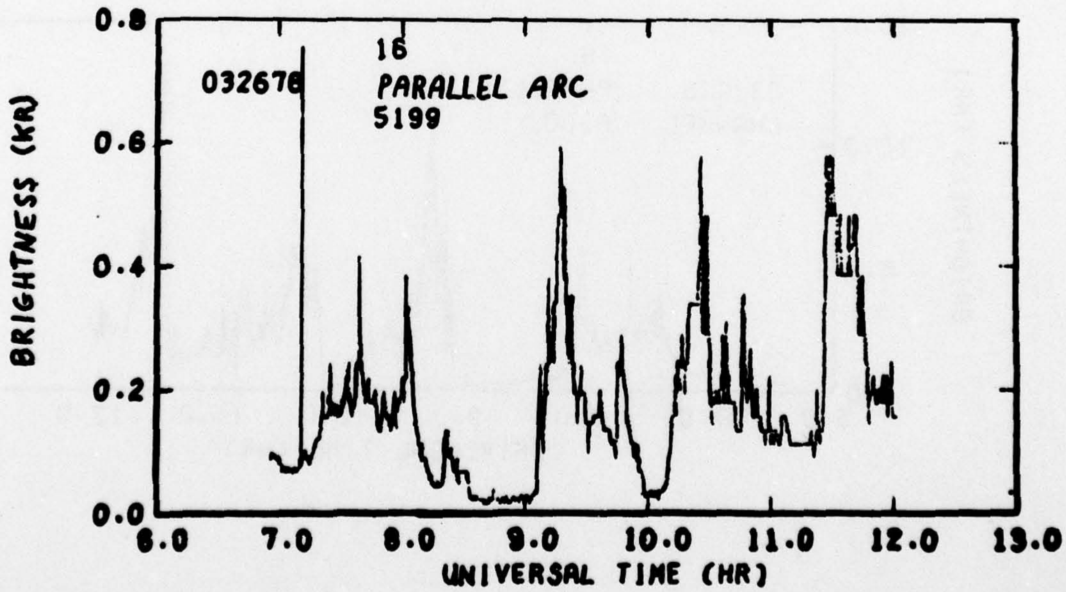
16
032676
PARALLEL ARC
5199
0.8
0.6
0.4
0.2
0.0
BRIGHTNESS (KR)
6.0
7.0
8.0
9.0
10.0
11.0
12.0
13.0
UNIVERSAL TIME (HR)

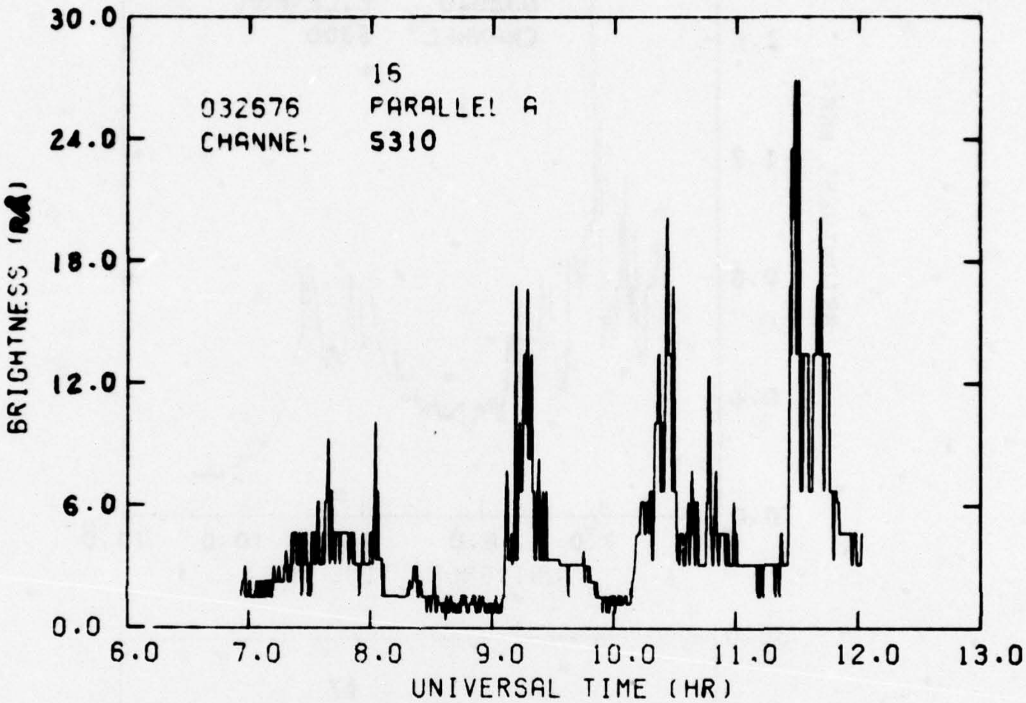

30.0
24.0
18.0
12.0
6.0
0.0
BRIGHTNESS (KR)
15
032676 PARALLEL A
CHANNEL 5310
6.0
7.0
8.0
9.0
10.0
11.0
12.0
13.0
UNIVERSAL TIME (HR)

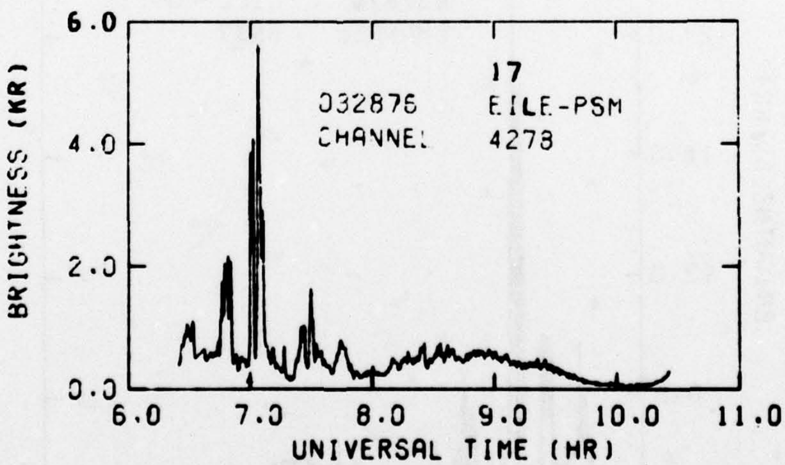

6.0
4.0
2.0
0.0
BRIGHTNESS (KR)
17
032876 EILE-PSM
CHANNEL 4278
6.0
7.0
8.0
9.0
10.0
11.0
UNIVERSAL TIME (HR)

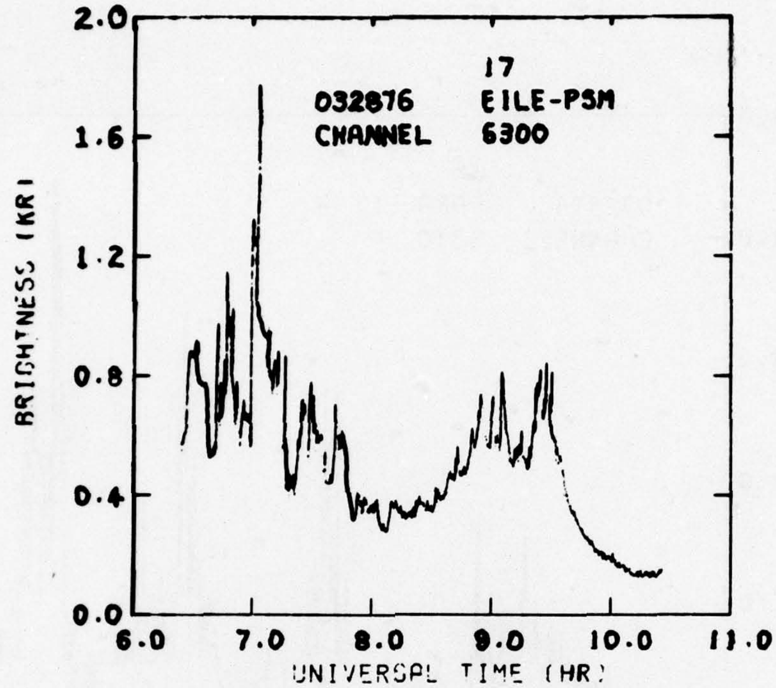
17
032876 EILE-PSM
CHANNEL 6300
BRIGHTNESS (KR)
2.0
1.6
1.2
0.8
0.4
0.0
6.0
7.0
8.0
9.0
10.0
11.0
UNIVERSAL TIME (HR)

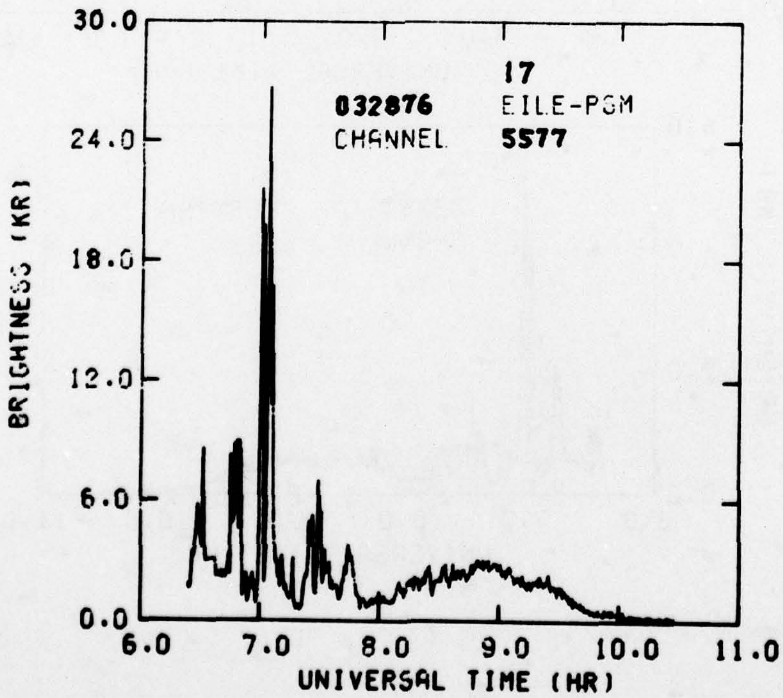
17
032876 EILE-PSM
CHANNEL 5577
BRIGHTNESS (KR)
30.0
24.0
18.0
12.0
6.0
0.0
6.0
7.0
8.0
9.0
10.0
11.0
UNIVERSAL TIME (HR)

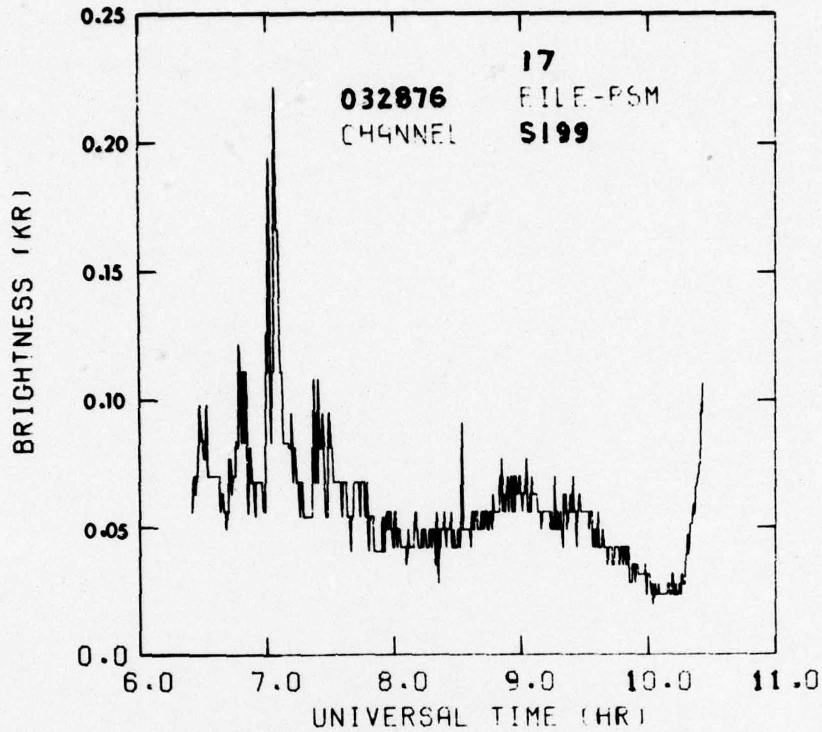

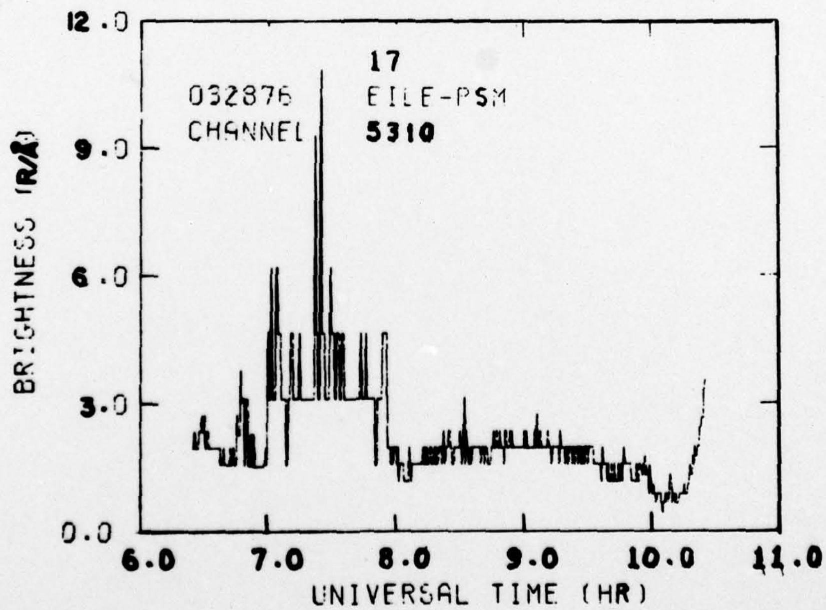

THIS PAGE IS BEST QUALITY PRACTICABLE
FROM COPY FURNISHED TO DDC

APPENDIX II

POSITION AND HEADING OF ICECAP 76 AIRCRAFT

(Refer to Section VI. The flight numbers are identified with mission type in Table 6 of Ref 3.)

MISSION: ICECAP 76-1 PSM/EIL DATE: 22 FEB 1976

#	TIME Z	LATITUDE N °	'	LONGITUDE W °	'	ALT. FL.	O.A.T. TRUE °C	HEADING MAG °	HEADING TRUE °	SPEED TR.AIR KTS	SPEED GRD KTS	SOLAR ANGLE ELEV. °	SOLAR ANGLE AZIM. °
1	1435	43	05	70	49	[illegible]	–	–	–	–	–	27.5	138.8
2	1505	46	47	73	14	?	–	–	–	–	–	30.0	149.8
3	1510	42	46	73	53	280	–	321	308	450	410	30.3	145.5
4	1550	46	22	78	15	280	–	324	314	450	420	29.3	152.4
5	1630	50	01	83	04	310	–	327	318	450	415	27.4	158.8
6	1647	51	22	84	57	312	-45	311	307	450	410	26.6	161.7
7	1710	53	00	87	46	310	-46	314	313	450	380	25.6	165.1
8	1720	53	41	89	20	310	-48	311	313	450	370	25.1	166.0
9	1750	55	26	93	27	350	-48	305	313	450	345	23.8	169.8
10	1805	56	12	95	33	350	-50	308	316	450	335	23.2	171.6
11	1825	57	27	97	55	350	-49	286	302	450	325	22.1	174.6
12	1840	58	06	100	05	350	-45	283	301	450	320	21.5	176.3
13	1940	61	26	109	23	350	–	248	280	455	390	18.2	182.3
14	2020	62	32	118	26	350	–	245	278	460	405	17.2	183.2
15	2040	63	06	123	20	350	-42	243	278	462	420	16.6	183.4
16	2100	63	35	129	31	350	-45	240	274	450	410	16.1	183.1
17	2130	63	57	136	12	350	-45	238	270	450	425	15.8	182.9
18	2135	64	16	138	14	350	-45	234	266	450	435	15.4	182.1
19	2215	64	40	147	06	LAND						15.0	183.3

MISSION: ICECAP 76-2 EIL/EIL DATE: 26 FEB 1976

TIME Z	LATITUDE N °	'	LONGITUDE W °	'	ALT. FL.	O.A.T. TRUE °C	HEADING MAG °	HEADING TRUE °	SPEED TR.AIR KTS	SPEED GRD KTS	SOLAR ANGLE ELEV. °	SOLAR ANGLE AZIM. °
1515	64	40	147	06	370	–	–	–	–	–	-13.0	82.5
1544	65	11	147	30	350	[illegible]	180	208	450	410	-10.1	89.4
1600	65	2	147	30	350	[illegible]	[illegible]	[illegible]	480	420	-8.4	93.0
1610	66	10	146	00	350	[illegible]	358	029	500	440	-6.8	96.6
1620	67	14	144	35	350	[illegible]	355	026	500	440	-5.4	99.9
1630	67	16	144	30	350	[illegible]	178	209	410	450	-4.4	102.3
1640	66	12	146	15	350	[illegible]	178	207	400	440	-3.9	104.1
1650	65	03	147	30	350	[illegible]	178	206	400	445	-3.2	104.2
1700	64	04	149	05	350	[illegible]	175	203	395	435	-2.5	105.2
1710	64	00	148	42	350	[illegible]	357	025	500	440	-1.3	107.8
1720	65	00	147	30	350	[illegible]	357	026	500	435	-0.1	111.0
1730	66	04	146	15	350	[illegible]	358	028	500	432	+0.9	114.5
1741	67	16	144	30	350	[illegible]	358	026	500	430	1.9	118.6
1750	67	16	144	30	350	[illegible]	179	208	390	440	2.7	120.7
1800	66	12	146	12	350	[illegible]	178	207	390	440	3.5	121.4
1809	66	17	146	16	350	[illegible]	357	028	500	430	4.2	123.5
1819	67	18	144	30	350	[illegible]	360	032	500	435	5.0	127.6
1829	67	16	144	25	350	[illegible]	179	209	380	465	5.8	129.9
1839	66	11	146	00	350	[illegible]	180	209	380	425	6.8	130.8
1849	65	14	147	05	350	[illegible]	174	202	360	430	7.7	131.4
1900	64	04	149	03	350	[illegible]	176	203	400	450	8.4	132.6
1911	64	04	148	53	350	[illegible]	360	028	510	440	9.8	135.4
1921	65	28	147	21	350	[illegible]	359	028	510	435	10.2	139.3
1931	66	12	146	02	350	[illegible]	358	028	510	430	10.4	143.3
1941	67	16	144	31	350	[illegible]	358	029	510	425	10.4	147.2
1950	67	15	144	35	350	[illegible]	178	208	400	445	10.8	149.9
2000	66	14	146	00	350	[illegible]	180	209	390	440	12.2	151.9
2010	65	12	147	27	350	[illegible]	179	208	390	445	13.0	[illegible]
2020	64	03	149	00	350	[illegible]	176	204	380	420	14.3	152.1
2024	64	12	149	06	350	[illegible]	359	027	470	[illegible]	14.3	153.0
[illegible]	65	12	148	05	350	[illegible]	357	027	505	430	14.1	156.7
2040	65	29	147	02	350	[illegible]	357	027	505	430	14.2	159.3
2044	65	35	147	00	350	[illegible]	172	204	410	440	14.2	160.2
2053	64	35	148	10	350	[illegible]	181	210	380	420	15.3	164.3
2105	64	40	147	06	LAND							

MISSION: ICECAP 76-3 EIL/EIL DATE: 18 FEB 1976

#	TIME Z	LATITUDE N °	'	LONGITUDE W °	'	ALT FL.	O.A.T. TRUE °C	HEADING MAG °	HEADING TRUE °	SPEED TR.AIR KTS	SPEED GRD KTS	SOLAR ANGLE ELEV. °	SOLAR ANGLE AZIM. °
1	0704	64	40	147	06	370	–	–	–	–	–	[illegible]	[illegible]
2	0730	–	–	–	–	350	–	010	038	450	–	–	–
3	0801	65	08	147	30	350	[illegible]	357	026	490	432	-28.3	324.8
4	0811	66	12	146	00	350	[illegible]	357	028	495	440	-29.2	329.5
5	0821	67	14	144	24	350	[illegible]	REVERSE COURSE			–	-29.1	[illegible]
6	0831	67	16	144	30	350	[illegible]	177	208	402	440	-29.4	332.1
7	0841	66	12	146	07	350	[illegible]	178	207	403	440	-30.5	337.8
8	0851	65	09	147	30	350	[illegible]	175	202	410	440	-31.7	332.9
9	0901	64	02	148	46	350	[illegible]	177	204	410	440	-32.9	340.1
10	0910	64	05	148	55	350	[illegible]	004	032	490	440	-32.2	[illegible]
11	0920	65	06	147	25	350	[illegible]	003	032	490	440	-32.6	341.3
12	0930	66	10	146	05	350	[illegible]	358	029	493	440	-31.8	353.0
13	0940	67	12	144	40	350	[illegible]	052	085	490	480	-31.0	356.6
14	0950	67	20	143	10	350	[illegible]	353	026	492	430	-30.9	001.1
15	0958	68	06	142	00	350	[illegible]	353	026	492	430	-30.1	004.9
16	1005	67	48	141	12	350	[illegible]	179	212	400	440	-30.2	002.3
17	1016	67	07	143	45	350	[illegible]	182	213	412	440	-30.9	009.1
18	1026	66	00	145	46	350	[illegible]	172	202	410	440	-32.0	008.6
19	1036	65	00	147	04	350	[illegible]	172	202	410	440	-32.9	010.2
20	1041	65	00	146	45	350	[illegible]	002	032	490	440	-32.8	012.0
21	1051	65	56	144	55	350	[illegible]	350	021	495	440	-31.4	016.9
22	1101	67	04	143	48	350	[illegible]	345	015	495	440	[illegible]	020.9
23	1110	67	06	143	52	350	[illegible]	177	208	420	440	-29.5	023.3
24	1120	66	02	145	25	350	[illegible]	179	209	420	450	-30.3	024.5
25	1130	65	01	146	53	350	[illegible]	176	204	420	440	-31.1	026.0
26	1140	63	55	148	16	350	[illegible]	042	070	410	400	-31.8	027.6
27	1152	HOLDING		DEPART 1208									
28	1220	64	40	147	06	LAND							

MISSION: ICECAP 76-4 EIL/EIL DATE: 29 FEB 1976

TIME Z	LATITUDE N °	'	LONGITUDE W °	'	ALT. FL.	O.A.T. TRUE °C	HEADING MAG °	HEADING TRUE °	SPEED TR.AIR KTS	SPEED GRD KTS	SOLAR ANGLE ELEV. °	SOLAR ANGLE AZIM. °
0743	64	40	147	06	370	–	–	–	–	–	-29.2	320.3
0808	–	–	–	–	350	[illegible]	177	205	440	425	–	–
0824	64	32	148	08	350	[illegible]	360	028	440	420	-30.5	330.4
0830	64	40	147	48	350	[illegible]	187	214	440	420	-30.8	332.5
0836	64	03	148	47	350	[illegible]	271	298	440	450	-31.4	332.9
0846	64	30	150	55	350	[illegible]	002	029	450	440	-31.1	333.5
0856	65	35	149	45	350	[illegible]	359	027	450	435	-30.8	337.8
0906	66	42	148	12	350	[illegible]	001	031	455	438	-30.3	342.7
0916	67	47	146	46	350	[illegible]	359	030	465	440	-29.6	347.4
0926	68	50	145	10	350	[illegible]	358	029	470	440	-28.8	352.2
0936	68	55	145	00	350	[illegible]	179	210	410	440	-28.8	355.1
0946	67	38	146	38	350	[illegible]	178	208	435	440	-30.2	356.1
0956	66	48	148	24	350	[illegible]	178	206	425	440	-31.0	356.8
1006	65	45	149	45	350	[illegible]	176	202	445	440	-32.1	358.1
1016	64	44	151	00	350	[illegible]	171	196	460	440	-33.1	359.7
1026	63	42	152	05	350	[illegible]	171	196	460	440	-34.1	001.3
1035	63	34	152	15	350	[illegible]	004	030	460	450	-34.2	[illegible]
1045	64	34	150	54	350	[illegible]	005	032	470	440	-32.0	[illegible]
1055	65	20	149	35	350	[illegible]	183	211	450	420	-32.0	012.6
1059	64	53	150	30	350	[illegible]	183	211	450	440	-32.4	012.8
1107	64	28	151	37	350	[illegible]	183	211	450	440	-33.1	014.1
1115	64	17	151	50	350	[illegible]	011	038	460	450	-32.7	016.1
1120	64	40	150	52	350	[illegible]	004	032	465	450	-32.1	018.5
1128	65	26	149	29	350	–	–	–	–	–	-30.8	022.4
[illegible]	64	40	147	06	LAND							

MISSION: ICE CAP 76-[illegible] E1L/E1L DATE: 1 MARCH 197[illegible]

#	TIME Z	LATITUDE N °	'	LONGITUDE W °	'	ALT 100 FT. FL.	OAT PVE °C	HEADING MAG °	TRUE °	SPEED TR.AIR KTS	GRD KTS	SOLAR ANGLE ELEV. °	AZIM. °
1	0753	64	40	147	06	T/0			-			-28.6	[illegible]
2	0818	[illegible]		[illegible]		350		[illegible]	[illegible]	[illegible]	-		
3	0828	65	41	149	50	350	[illegible]	004	032	390	420	[illegible]	[illegible]
4	0838	66	42	148	12	350	[illegible]	359	029	390	420	[illegible]	[illegible]
5	0848	67	45	146	45	350	[illegible]	359	030	385	420	-27.6	339.9
6	0858	68	49	144	55	350	[illegible]	357	030	405	420	[illegible]	[illegible]
7	0909	69	56	143	31	350	[illegible]	357	030	405	420	-27.2	349.4
8	0920	69	57	143	20	350	[illegible]	177	210	470	420	[illegible]	[illegible]
9	0930	68	56	144	05	350	[illegible]	175	207	495	440	[illegible]	354.8
10	0941	67	49	146	50	350	[illegible]	172	203	497	432	[illegible]	354.7
11	0952	66	43	148	21	350	[illegible]	175	203	497	422	-30.7	356.2
12	1002	65	36	149	22	350	[illegible]	180	208	500	420	-31.8	357.7
13	1010	65	35	149	23	350	[illegible]	359	027	395	440	-31.9	000.2
14	1020	66	42	148	05	350	[illegible]	352	022	395	440	-30.7	004.5
15	1030	67	49	146	45	350	[illegible]	356	027	400	435	-29.4	008.8
16	1032	68	03	146	29	350		-	-	-		-29.1	009.6
17	1034	67	57	146	21	350	-	178	208	450	400	-29.2	010.5
18	1036	67	45	146	45	350	[illegible]	176	206	500	435	-29.4	010.5
19	1047	66	42	148	27	350	[illegible]	-	-	500	-	-30.3	011.8
20	1050	66	44	148	47	350	-	030	060	450	480	-30.2	012.3
21	1054	67	02	147	51	350	-	002	032	450	500	-29.8	014.5
22	1100	67	45	146	33	350	[illegible]	356	027	400	440	-28.2	017.5
23	1110	68	44	145	12	350	[illegible]	359	027	410	440	-27.4	021.7
24	1120	68	49	145	06	350	[illegible]	187	218	497	439	-27.0	024.4
25	1130	67	50	146	50	350	[illegible]	173	203	500	425	-27.7	025.6
26	1141	66	42	14[illegible]	20	350	[illegible]	175	203	500	425	-28.5	027.2
27	1151	65	37	149	34	350	[illegible]	174	201	500	430	-29.2	028.9
28	1201	64	35	150	51	350	[illegible]	079	107	450	460	-29.9	030.6
29	1245	64	40	147	06	LAND	-						

MISSION: ICE CAP 76-7 EIL/RIV DATE: 4 MARCH [illegible]

#	TIME Z	LATITUDE N °	'	LONGITUDE W °	'	ALT 100 FT. FL.	OAT	HEADING MAG °	TRUE °	SPEED TR.AIR KTS	GRD KTS	SOLAR ANGLE ELEV. °	AZIM. °
1	0910	64	40	147	06	T/0	[illegible]	-	-	-	-	-31.1	[illegible]
2	0937	62	56	141	50	330	[illegible]	120	150	462	490	-33.4	[illegible]
3	0951	61	23	139	00	330	-	131	161	490	525	-34.7	008.4
4	1010	59	00	136	08	330		126	155	490	532	-36.1	018.1
5	1031	56	30	134	00	330		125	154	490	535	-36.9	027.7
6	1042	55	02	131	32	330		125	151	490	535	-36.6	034.4
7	1100	52	35	128	50	330		121	146	495	550	-35.8	043.8
8	1116	50	38	126	55	330		099	122	495	530	-34.4	051.2
9	1136	48	38	123	25	330		120	142	497	540	-31.0	060.7
10	1146	47	25	122	26	330		148	168	500	536	-29.4	064.6
11	1200	45	26	121	36	330		147	166	500	530	-27.5	069.3
12	1221	42	30	120	32	330		149	168	500	540	-24.0	075.7
13	1241	39	30	119	40	330		158	175	500	542	-20.3	081.1
14	1302	36	18	119	11	330		138	153	500	532	-16.2	085.8
15	1340	33	54	117	15	LAND							

MISSION: ICE CAP 76-8 RIV/EIL DATE: 4 MARCH 1976

#	TIME Z	LATITUDE N °	'	LONGITUDE W °	'	ALT 100 FT. FL.	OAT TRUE °C	HEADING MAG °	TRUE °	SPEED TR.AIR KTS	GRD KTS	SOLAR ANGLE ELEV. °	AZIM. °
1	1543	33	54	117	15	T/0		-	-	-	-	+17.2	110.1
2	1612	35	18	119	07	310	[illegible]	339	356	465	420	20.7	114.2
3	1630	37	28	119	20	310	[illegible]	338	355	497	420	22.9	118.1
4	1645	39	14	119	37	310	[illegible]	328	346	497	430	24.4	121.5
5	1700	41	00	120	05	310	[illegible]	329	347	498	430	25.5	125.0
6	1715	42	52	120	47	350	[illegible]	327	346	475	425	26.2	128.4
7	1732	44	36	121	31	350	[illegible]	326	346	480	415	27.0	132.2
8	1745	45	53	122	58	350	[illegible]	338	358	485	390	27.3	134.4
9	1800	47	15	123	25	350	[illegible]	337	358	485	390	27.6	138.2
10	1812	48	45	123	31	350	[illegible]	313	336	480	390	27.7	141.6
11	1830	49	57	125	32	390	[illegible]	295	318	480	400	27.8	144.[illegible]
12	1846	51	11	127	27	390	[illegible]	306	332	470	390	27.5	147.2
13	1903	52	48	129	25	390	[illegible]	309	335	475	395	26.8	150.0
14	1915	54	00	130	22	390	[illegible]	302	330	475	400	26.4	152.4
15	1930	55	25	131	55	390	—	302	330	475	410	25.7	155.1
16	1945	56	53	132	29	390	[illegible]	291	320	480	420	25.0	158.8
17	1958	58	08	135	12	390	[illegible]	297	327	470	440	24.0	159.6
18	2015	59	56	137	10	410	[illegible]	291	321	462	430	22.7	162.3
19	2032	61	47	139	00	390	[illegible]	276	306	460	430	21.2	165.0
20	2045	63	46	141	50	390	[illegible]	264	295	469	435	20.3	165.6
21	2105	64	00	145	40	390	—	280	311	465	430	19.2	166.8
22	2114	64	57	146	55	—		-				18.4	168.0
23	2205	64	40	147	06	LAND							

MISSION: ICE CAP 76-6 EIL/EIL DATE: 3 MARCH 1976

#	TIME Z	LATITUDE N °	'	LONGITUDE W °	'	ALT 100 FT. FL.	OAT TRUE °C	HEADING MAG °	TRUE °	SPEED TR.AIR KTS	GRD KTS	SOLAR ANGLE ELEV. °	AZIM. °
1	0105	64	40	147	06	T/0	-	-	-	-	-	+10.9	226.8
2	0136	65	07	147	29	350	-	[illegible]	[illegible]	450	-	+8.1	233.7
3	0145	65	08	147	30	350	[illegible]	[illegible]	[illegible]	450	440	+7.3	235.8
4	0154	66	12	146	05	350	[illegible]	350	020	425	440	+5.5	239.2
5	0204	67	15	144	33	350	[illegible]	349	020	405	420	+3.5	242.9
6	0215	67	12	144	38	350	[illegible]	189	219	460	440	+2.6	245.4
7	0225	66	11	146	06	350	[illegible]	189	218	490	435	+2.7	246.4
8	0235	65	09	147	25	350	[illegible]	186	215	490	440	+2.7	247.4
9	0245	65	08	147	16	350	[illegible]	349	019	430	435	+1.6	249.9
10	0255	66	11	146	06	350	[illegible]	349	019	420	440	-0.2	253.3
11	0305	67	15	144	33	350	[illegible]	349	020	428	439	-1.9	256.9
12	0315	67	17	144	28	350	[illegible]	187	218	495	440	-2.9	259.3
13	0325	66	14	146	02	350	[illegible]	188	217	497	444	-3.1	260.2
14	0335	65	09	149	28	350	[illegible]	185	214	495	448	-3.3	261.0
15	0345	65	14	147	23	350	[illegible]	351	021	450	468	-4.4	263.4
16	0355	66	12	146	05	350	[illegible]	345	016	468	430	-6.1	267.0
17	0405	67	16	144	33	350	[illegible]	348	019	468	431	-7.7	270.7
18	0415	67	14	144	35	350	[illegible]	185	216	495	440	-8.6	273.1
19	0425	66	14	146	02	350	[illegible]	189	219	490	440	-9.1	273.9
20	0435	65	09	147	29	350	[illegible]	186	214	490	440	-9.6	274.6
21	0445	65	09	147	32	350	[illegible]	353	022	440	450	-10.6	276.9
22	0455	66	05	146	08	350	[illegible]	351	018	435	440	-12.1	280.8
23	0506	67	16	144	32	350	[illegible]	348	018	440	445	-13.4	284.7
24	0518	67	13	144	43	350	[illegible]	184	214	475	440	-14.6	287.7
25	0523	66	10	146	08	350	[illegible]	188	218	485	436	-14.8	287.2
26	0533	65	07	147	32	350	[illegible]	185	214	485	435	-15.6	288.0
27	0543	65	08	147	29	410	[illegible]	350	019	430	445	-16.6	290.5
28	0553	66	15	146	02	410	[illegible]	350	020	410	437	-17.6	294.5
29	0603	67	13	144	36	410	[illegible]	347	019	435	440	-18.4	298.7
30	0613	68	14	142	53	410	[illegible]	344	021	440	445	-19.4	302.2
31	0624	68	17	142	55	410	[illegible]	189	220	420	435	-20.2	305.9
32	0634	67	15	144	35	410	[illegible]	185	216	495	448	-21.1	306.5
33	0642	66	32	145	37	410	[illegible]	186	216	480	440	-21.8	307.2
34	0650	67	[illegible]	144	28	410	[illegible]	[illegible]	011	460	460	-22.3	310.6
35	0700	67	12	144	32	410	[illegible]	193	221	440	445	-23.1	[illegible]
36	0710	66	04	144	55	410	[illegible]	197	227	485	440	-24.5	[illegible]
37	0720	65	08	147	47	410	[illegible]	196	226	480	420	-25.0	[illegible]
38	0755	64	40	147	06	LAND							

MISSION: ICE CAP 76-9 EIL/EIL DATE: 7 MARCH 1976

#	TIME Z	LATITUDE N °	'	LONGITUDE W °	'	ALT 100 FT. FL.	OAT TRUE °C	HEADING MAG °	TRUE °	SPEED TR.AIR KTS	GRD KTS	SOLAR ANGLE ELEV. °	AZIM. °
1	0831	64	40	147	06	T/0	-	-	-	-	-	-28.4	339.9
2	0859	65	07	147	31	350	[illegible]	004	034	392	440	-29.0	342.2
3	0909	66	12	145	55	350	[illegible]	354	025	398	440	-28.4	347.1
4	0919	67	15	144	36	350	[illegible]	358	030	402	440	-27.7	351.6
5	0929	67	55	144	00	350	[illegible]	358	030	402	440	-27.2	355.0
6	0939	67	55	144	[illegible]	350	[illegible]	181	214	[illegible]	440	-27.2	357.8
7	0949	67	17	144	52	350	[illegible]	177	208	500	435	-27.9	359.7
8	0959	66	14	146	10	350	[illegible]	180	190	500	440	-28.9	000.9
9	1010	66	17	145	56	350	[illegible]	358	029	400	430	-28.8	004.4
10	1020	67	17	144	52	350	[illegible]	358	029	410	440	-27.6	008.7
11	1033	67	15	144	34	350	[illegible]	181	212	490	440	-27.4	012.3
12	1043	66	10	146	11	350	[illegible]	178	208	490	430	-28.4	013.5
13	1053	65	08	147	27	350	[illegible]	170	199	490	430	-29.3	014.9
14	1103	65	09	147	29	350	[illegible]	001	030	400	435	-29.0	017.8
15	1113	66	11	146	06	350	[illegible]	359	030	410	405	-27.4	022.0
16	1123	67	14	144	34	350	[illegible]	359	030	415	440	-25.8	026.1
17	1132	67	22	144	29	350	—	262	292	495	470	-25.3	028.6
18	1138	67	24	145	17	350	—	230	260	400	[illegible]	-25.1	028.7
19	1145	67	11	147	16	350	—	[illegible]	[illegible]	[illegible]	[illegible]	-25.9	029.2
20	1230	64	40	147	06	LAND							

THIS PAGE IS BEST QUALITY PRACTICABLE
FROM COPY FURNISHED TO DDC

THIS PAGE IS BEST QUALITY PRACTICABLE
FROM COPY FURNISHED TO DDC

MISSION: ICE CAP 76-10 — EIL/EIL — DATE: 8 MARCH 1976

TIME (Z)	LATITUDE N (°)	(')	LONGITUDE W (°)	(')	ALT. 100 FT. (FL.)	O.A.T. TRUE (°C)	HEADING MAG (°)	HEADING TRUE (°)	SPEED TR.AIR (KTS)	SPEED GRD (KTS)	SOLAR ANGLE ELEV. (°)	SOLAR ANGLE AZIM. (°)
0630	64	40	147	06	T/O	-	-	-	-	-	-19.7	303.1
0654	64	47	147	45	350	-	360	029	420	440	-21.4	308.5
0656	65	02	147	24	350	-30.5	360	029	420	440	-21.6	309.4
0706	66	10	146	00	350	-40	354	025	425	440	-22.0	313.8
0716	67	18	144	29	350	-40.5	357	029	430	440	-22.3	318.3
0726	68	16	142	55	350	-44.5	358	030	435	450	-22.5	322.7
0736	68	16	142	55	350	—	164	196	480	450	-23.1	325.4
0741	67	47	143	07	350	—	099	142	390	385	-23.7	326.3
0750	67	22	143	10	350	-43.9	263	296	402	385	-24.5	328.6
0758	67	50	144	18	350	—	014	047	430	440	-24.3	329.7
0813	69	27	141	19	350	—	357	032	435	430	-23.9	337.3
0818	69	36	140	08	350	—	184	218	475	440	-24.1	339.9
0821	69	10	141	10	350	-48.0	186	210	475	440	-24.4	339.5
0830	68	17	143	00	350	-45	188	211	465	430	-25.3	339.8
0838	68	22	143	21	350	-48.0	001	032	500	490	-25.4	341.6
0850	69	36	142	57	350	-	349	023	432	430	-24.6	345.5
0853	69	51	143	26	350	-	239	272	390	370	-24.2	345.8
0905	69	56	143	24	350	-	089	124	450	440	-24.5	349.1
0915	69	26	141	25	350	-50.5	187	210	470	440	-25.2	354.1
0926	68	19	143	10	350	-45.5	189	211	470	450	-26.4	355.1
0936	67	15	144	36	350	-43	181	212	465	440	-27.5	356.3
0946	66	10	146	16	350	-42.5	181	211	470	440	-28.6	357.2
0956	65	10	146	00	350	-39.5	118	146	470	450	-29.6	000.3
1037	64	40	147	06	LAND							

MISSION: ICE CAP 76-[illegible] — EIL/EIL — DATE: 13 MARCH

TIME (Z)	LATITUDE N (°)	(')	LONGITUDE W (°)	(')	ALT. 100 FT. (FL.)	O.A.T. TRUE (°C)	HEADING MAG (°)	HEADING TRUE (°)	SPEED TR.AIR (KTS)	SPEED GRD (KTS)	SOLAR ANGLE ELEV. (°)	SOLAR ANGLE AZIM. (°)
2026	64	40	147	06	T/O	-	—	—	—	—	20.6	155.4
2038	64	36	149	06	240	—	230	258	400	350	20.9	156.5
2043	64	10	148	16	310	—	118	146	450	450	21.6	158.7
2050	63	29	147	05	310	-43.5	42/227	70/255	450	450/375	22.7	161.7
2053	63	28	147	32	310	-43.5	227	255	450	375	22.8	162.0
2106	63	00	150	25	310	-41.5	225	251	450	400	23.3	162.4
2117	63	00	150	00	310	-42.0	086	113	465	490	23.6	165.7
2128	62	31	147	30	310	-45.5	085	113	445	485	24.6	171.5
2135	PILOT		VISUAL		FLIGHT	-	—	-	—	—	-	-
2228	62	42	147	02	330	-45.0	250	277	465	410	24.4	188.5
2240	62	50	147	24	330	-44.0	248	274	420	370	24.1	191.4
2255	VISUAL	AROUND	MOUNTAIN			-	-	-	-	-	-	-
2335	63	28	149	26	350	-42.5	360	027	440	470	21.9	203.8
2400	64	40	147	06	LAND						19.1	212.6

MISSION: ICE CAP 76-12 — EIL/HIK — DATE: 15 MARCH 1976

TIME (Z)	LATITUDE N (°)	(')	LONGITUDE W (°)	(')	ALT. 100 FT. (FL.)	O.A.T. TRUE (°C)	HEADING MAG (°)	HEADING TRUE (°)	SPEED TR.AIR (KTS)	SPEED GRD (KTS)	SOLAR ANGLE ELEV. (°)	SOLAR ANGLE AZIM. (°)
1235	64	40	147	06	T/O	-	-	-	-	-	-21.2	42.8
1250	64	02	148	41	280	-	006	034	450	510	-21.0	45.2
1304	65	07	147	31	280	-48	186	214	455	395	-18.8	48.7
1316	64	02	148	50	280	-46.5	170	196	458	395	-18.9	51.7
1336	61	34	149	58	310	-46	186	210	450	390	-18.7	56.7
1357	59	43	151	27	310	-46.5	154	178	480	410/390	-18.3	60.2
1417	58	13	150	36	310	-40	175	198	502	400	-16.3	66.1
1430	56	07	151	20	310	-48	171	193	501	418	-15.8	68.9
1500	52	45	152	56	310	-42.5	169	189	460	405	-13.6	74.8
1530	49	10	154	31	350	-34	167	185	425	400	-10.7	80.4
1600	45	44	155	05	350	-52	170	187	460	440	-6.5	86.1
1630	42	05	155	43	350	-36	176	192	460	470	-1.6	91.1
1700	38	10	156	30	350	-49	177	193	470	500	+3.7	95.4
1730	34	15	157	10	350	-56	184	199	445	485	9.7	99.0
1750	32	55	157	50	350	-53	178	191	445	405	13.4	101.2
1800	30	56	157	52	350	-51	170	183	440	425	15.9	102.2
1807	20	00	157	45	350	—	159	171	440	420	17.8	103.0
1815	28	10	157	58	350	-46	143	155	450	428	19.7	103.3
1832	26	00	157	00	350	-49	156	168	440	425	24.7	105.3
1855	24	03	156	19	350	-46	173	185	445	380	30.9	108.0
1950	21	20	157	55	LAND	[illegible]	[illegible]	—	—	—	42.2	113.6

MISSION: ICE CAP 76-13 — HIK/HIK — DATE: 21 MARCH 1976

TIME (Z)	LATITUDE N (°)	(')	LONGITUDE W (°)	(')	ALT. 100 FT. (FL.)	O.A.T. TRUE (°C)	HEADING MAG (°)	HEADING TRUE (°)	SPEED TR.AIR (KTS)	SPEED GRD (KTS)	SOLAR ANGLE ELEV. (°)	SOLAR ANGLE AZIM. (°)
0635	21	20	157	55	T/O		—	—	—	—	-26.7	281.7
0706	20	22	160	51	370	-37.0	246/343	257/354	460	325	-31.3	283.5
0720	19	57	162	02	390	-34.5	241	252	395	260	33.5	284.3
0735	19	37	163	20	370	-35.5	237	248	420	300	-35.8	285.3
0755	19	00	165	00	370	-36.5	237	248	420	310	-39.1	286.7
0815	18	15	166	35	370	-50	231	243	420	300	-42.4	288.0
0830	17	37	167	52	370	-51	233	244	485	370	44.8	288.9
0846	16	46	169	32	370/410	-48	231/332	242/343	465/460	370/430	47.2	289.6
0905	19	03	169	40	410	-59	332	343	460	460	-50.3	295.2
0921	21	00	170	00	410		334/067	343/078	460	460/500	-57.5	300.7
0955	22	00	165	07	410	-55	071	082	450	510	-61.5	319.3
1010	22	08	162	55	410	-59.5	071	082	460	530	-64.6	330.6
1021	22	24	161	15	410		—	-	-	-	-66.0	340.5
1055	21	20	157	55	LAND							

MISSION: ICE-CAP 76-14 — HIK/EIL — DATE: 22 MARCH 1976

TIME (Z)	LATITUDE N (°)	(')	LONGITUDE W (°)	(')	ALT. 100 FT. (FL.)	O.A.T. TRUE (°C)	HEADING MAG (°)	HEADING TRUE (°)	SPEED TR.AIR (KTS)	SPEED GRD (KTS)	SOLAR ANGLE ELEV. (°)	SOLAR ANGLE AZIM. (°)
1830	21	20	157	55	T/O		—	—	—	—	+26.1	99.9
1906	24	03	156	19	280	-30.5	305/333	017/345	420	400/395	35.0	106.9
1930	26	35	156	54	280	-33.5	334	347	420	400	38.8	113.2
1950	28	54	157	20	310	-39.5	331	345	420	390	41.1	117.5
2001	30	02	157	42	310	-41.8	354	008	420	390	42.8	120.6
2020	32	12	157	24	310	-41.8	350	004	420	385	45.1	127.2
2050	35	24	156	48	350	-43.5	351	006	420	390	47.5	139.0
2120	38	52	156	10	390	-60.0	349	005	420	390	48.6	152.1
2146	40	50	155	45	390	-62.8	347	004	420	400	48.9	163.1
2200	42	24	155	25	390	-54	344	002	420	410	48.1	165.2
2230	45	45	154	48	390	-51.5	343	002	460	450	45.2	181.3
2310	50	34	152	30	390	-38.5	335	357	450	420	39.1	197.2
2340	54	15	152	05	390	-36.0	349	012	475	460	34.0	205.8
0007	57	24	150	38	390	-37.0	324	348	450	430	28.9	214.1
0026	59	43	151	27	390	-40.8	356	021	450	430	25.9	217.5
0044	61	34	149	58	390	-40.5	347	013	440	430	22.6	223.1
0105	64	03	148	47	390	-41.5	359	027	450	440	18.8	229.0
0115	65	09	147	30	390	-43	358	027	450	440	16.8	232.5
0125	64	14	145	53	390	-46.0	085	116	450	440	15.9	236.8
0130	-		-		-	-	-	-	-	420	-	-
0220	64	40	147	06	LAND							

MISSION: ICE CAP 76-15 — EIL/EIL — DATE: 23 MARCH 1976

TIME (Z)	LATITUDE N (°)	(')	LONGITUDE W (°)	(')	ALT. 100 FT. (FL.)	O.A.T. TRUE (°C)	HEADING MAG (°)	HEADING TRUE (°)	SPEED TR.AIR (KTS)	SPEED GRD (KTS)	SOLAR ANGLE ELEV. (°)	SOLAR ANGLE AZIM. (°)
2035	64	40	147	06	T/O	-					25.0	157.6
2055	63	46	151	53	350	[illegible]	221	246	470	452	25.9	157.8
2110	62	57	155	37	—	ORBIT	MAG	ATH			26.6	157.6
2135	62	48	154	01	350		276	102	470	470	27.9	166.3
2147	62	47	150	33	350		160	185	470	460	28.4	173.6
2157	61	30	150	30	350						29.5	176.5
2216	61	50	148	35	—	ORBIT	POINT				29.4	184.2
2233	62	43	148	26	350		350	018	495	485	28.3	189.1
2251	64	40	147	06	350		203	230	470	450	25.9	195.4
2320	63	07	150	29	360	ORBIT	POINT				26.9	199.9
2333	62	40	150	35	360		008	036	475	460	26.8	203.5
0020	64	10	147	06	LAND						21.6	219.2

THIS PAGE IS BEST QUALITY PRACTICABLE
FROM COPY FURNISHED TO DDC

53120

MISSION: ICE CAP 76-16 — EIL/UIL — DATE: 26 MARCH 1976

	TIME	LATITUDE N.		LONGITUDE W.		ALT. 100 FT.	OAT TRUE	HEADING MAG	HEADING TRUE	SPEED TR.AIR	SPEED GRD	SOLAR ANGLE ELEV.	SOLAR ANGLE AZIM.
	Z	°	'	°	'	FL.	°C	°	°	KTS	KTS	°	°
	0630	64	40	147	06	510	–	–	–	–	–	-13.4	306.9
2	0648	64	05	149	48		–	182	209	420	400	-14.8	309.5
3	0659	62	58	150	00	350	-16 -37 -37.5	181	206	450	420	16.0	310.7
4	0709	61	51	151	08	350	-13 -35 -37.0	181	206	470	440	17.2	311.9
5	0719	61	51	151	08	350	-17 -36 -36.5	359	024	430	440	18.1	314.4
6	0726	62	42	150	10	350	—	359	024	430	440	18.3	317.2
7	0730	62	31	150	00	350	-18 -36 -37.0	181	206	450	420	18.8	318.4
8	0738	61	48	150	35	350	—	181	206	450	420	-19.8	319.6
9	0740	61	52	151	11	350	-16 -37 -36.0	359	024	430	445	-19.7	319.6
10	0750	62	58	150	00	350	-19 -37 -36.5	360	027	420	440	-19.9	323.5
11	0800	64	00	148	45	350	-19 -38 -37.5	360	028	420	440	-20.0	327.6
12	0810	65	06	147	27	350	-20 -39 -38.5	359	028	420	430	-19.9	331.8
13	0820	66	12	146	02	350	-20 -40 -40.5	359	030	440	455	-19.6	336.0
14	0830	67	15	144	25	350	-21 -41 -41.5	358	030	440	450	-19.2	340.5
15	0840	68	18	142	57	350	-22 -41 -42	357	031	430	440	-18.7	344.8
16	0844	–	–	–	–	350	–	REVERSE TRACK SOUTH BOUND				–	–
17	0848	68	40	142	24	350	–	179	213	460	440	18.5	347.4
18	0851	68	18	142	54	350	-22 -43 -45.5	181	213	470	440	-18.9	347.7
19	0901	67	18	144	30	350	-18 -42 -44	181	212	470	440	-20.0	348.6
20	0905	66	51	145	10	350	–	CHASING ARCS				-20.4	348.8
21	0915	66	40	147	50	350	-20 -41 -39.9	225	255	425	400	-20.6	348.7
22	0927	66	28	151	10	350	-21 -40 -39.0	200	227	410	385	-20.6	348.3
23	0935	65	50	152	20	350	-21 -40 -38.5	180	206	405	390	-21.4	349.1
24	0940	65	21	152	35	350	-11 -39 -39.5	100	126	405	400	-22.0	350.3
25	0950	64	42	150	20	350	-20 -38 -37.5	109	135	405	405	-22.9	355.2
26	0958	63	58	148	55	350	-16 -37 -38.0	112/182	139/209	470/455	440/415	-23.7	359.1
27	1008	63	02	149	50	350	-15 -20 -37.5	185	210	455	430	-24.6	000.7
28	1013	–	–	–	–	350	–	WEST TO	CHASE	AURORA	–	–	–
29	1018	62	48	151	20	350	-19 -37 -37.6	287	313	430	410	-24.8	001.8
30	1025	63	20	152	25	350	—	270	295	410	390	-24.3	002.6
31	1034	63	54	154	30	350	-19 -38 -36.9	270	295	410	390	-23.7	002.8
32	1044	63	47	152	38	350	-21 -39 -39.0	075	100	410	425	-23.7	007.4
33	1052	63	41	150	33	350	-20 -39 -38.5	050	076	420	425	-23.5	012.0
34	1058	63	50	148	58	350	-20 -39 -38.5	050/185	076/211	420/430	415/400	-23.0	015.1
35	1108	62	59	149	45	350	-15 -37 -37.5	186	212	455	430	-23.6	017.2
	1119	61	54	151	18	350	-15 -37 -37.5	186 CHASE	212 AURORA	455	430	-24.4	018.7
	1127	61	04	151	20	350	-15 -38 -39	215	240	480	430	-24.9	020.9
	1135	61	09	152	55	350	—	275	299	450	430	-24.8	021.3
37	1141	61	45	153	04	350	-15 -36 -38.0	005	030	465	470	-24.0	022.7
40	1153	62	52	150	55	350	-15 -36 -34.0	020	046	420	430	-21.9	027.9
41	1202	63	43	149	05	350	-19 -37 -40	013	040	405	420	-20.3	032.0
42	1245	64	40	147	06	LAND							

MISSION: ICE CAP 76-17 — EIL/PSM — DATE: 28 MARCH 1976

TIME	LATITUDE N.		LONGITUDE W.		ALT. 100 FT.	OAT TRUE	HEADING MAG	HEADING TRUE	SPEED TR.AIR	SPEED GRD	SOLAR ANGLE ELEV.	SOLAR ANGLE AZIM.
Z	°	'	°	'	FL.	°C	°	°	KTS	KTS	°	°
0556	64	40	147	06	510	–	–	–	–	–	-9.8	299.3
0615	63	40	143	45	290	[illegible]	075	106	450	455	-13.3	306.9
0645	62	48	135	52	290	[illegible]	080	112	458	450	-18.8	321.9
0715	62	44	128	09	290	[illegible]	080	114	450	450	-22.4	337.7
0730	61	50	124	21	290	[illegible]	088	121	450	450	-24.3	345.7
0800	59	58	117	46	290	[illegible]	107	130	450	440	-26.9	001.2
0830	57	42	112	10	330	[illegible]	112	136	465	460	-24.2	016.1
0845	56	18	109	48	330	[illegible]	086	108	460	450	-28.3	023.1
0900	55	36	106	37	330	[illegible]	094	110	462	460	-27.2	030.8
0930	54	22	100	21	330	[illegible]	097	108	465	470	-23.3	045.4
1000	53	22	93	52	330	[illegible]	103	104	470	485	-17.4	058.9
1030	52	36	87	12	330	[illegible]	107	100	450	500	-10.0	071.3
1100	51	43	80	50	330	[illegible]	102	086	460	490	-1.9	082.5
1127	52	03	75	00	330	[illegible]	190	172	460	410	+5.9	092.4
1147	49	57	74	18	330	[illegible]	181	163	455	370	+9.6	096.6
1315	43	05	70	49	LAND	[illegible]	[illegible]	–	–	–	–	–

DISTRIBUTION LIST

DEPARTMENT OF DEFENSE

Director
Defense Advanced Rsch. Proj. Agency
ATTN: LTC W. A. Whitaker
ATTN: Strategic Technology Office
ATTN: Nuclear Monitoring Research

Defense Documentation Center
Cameron Station
12 cy ATTN: TC

Director Defense Nuclear Agency
ATTN: TISI Archives
ATTN: RAAE, MAJ John Clark
ATTN: RAEV, Harold C. Fitz, Jr.
ATTN: DDST
ATTN: RAAE, MAJ James W. Mayo
3 cy ATTN: TITL, Tech. Lib.
2 cy ATTN: RAAE, Charles A. Blank

Commander
Field Command
Defense Nuclear Agency
ATTN: FCPR

Chief
Livermore Divison, Fld. Command DNA
Lawrence Livermore Laboratory
ATTN: FCPRL

Under Secy. of Def. for Rsch. & Engrg.
ATTN: S&SS(OS)

DEPARTMENT OF THE ARMY

Commander/Director
Atmospheric Sciences Laboratory
U.S. Army Electronics Command
ATTN: DELAS-AE-M, F. E. Niles
ATTN: H. Ballard
ATTN: DRSEL-BL-SY-S, D. Snider
ATTN: R. Rosen

Commander
Harry Diamond Laboratories
2 cy ATTN: DELHD-NP, F. N. Wimenitz

Commander
U.S. Army Nuclear Agency
ATTN: MONA-WE, J. Berberet

Director
BMD Advanced Tech. Center
ATTN: ATC-O, W. Davies
ATTN: ATC-T, Melvin T. Capps

Dep. Chief of Staff for Rsch. Dev. & Acq.
ATTN: NCB Division
ATTN: DAMA-CSZ-C
ATTN: Dama-WSZ-C

Chief of Engineers
ATTN: Fernand DePersin

DEPARTMENT OF THE ARMY (Continued)

Dep. Chief of Staff for Ops. & Plans
ATTN: DAMO-DDL, COL D. W. Einsel
ATTN: Div. of Chem. & Nuc. Ops.

Director
U.S. Army Ballistic Research Labs.
ATTN: Tech. Lib., E. Baicy
ATTN: John Mester
ATTN: J. Heimerl
ATTN: M. Kregl

Commander
U.S. Army Electronics Command
ATTN: DRSEL-PL-ENV, Hans A. Bomke
ATTN: DRSEL
ATTN: Stanley Kronenberg
ATTN: DRSEL-RD-P
ATTN: DRSEL-TL-IR, E. T. Hunter
ATTN: Inst. for Exploratory Rsch.
ATTN: Weapons Effects Section

Commander
U.S. Army Foreign Science & Tech. Ctr.
ATTN: Robert Jones

Commander
U.S. Army Material Dev. & Rdns. Cmd.
ATTN: DRXCD-TL
ATTN: DRCCDC, J. A. Bender

Commander
U.S. Army Missile Command
ATTN: DRSMI-ABL
ATTN: Chief, Doc. Section
ATTN: DRSMI-XS, Chief Scientist

Chief
U.S. Army Research Office
ATTN: CRDARD-CCS, Hermann Robl
ATTN: CRDARD-P, Robert Mace

DEPARTMENT OF THE NAVY

Chief of Naval Research
ATTN: Code 421, B. R. Junker
ATTN: Code 461, Jacob Warner
ATTN: Code 461, R. G. Joiner

Commander
Naval Ocean Systems Center
ATTN: Code 2200 1, Verne E. Hildebrand
ATTN: Code 2200, Ilan Rothmuller
ATTN: Code 2200, Jurgan Richter
ATTN: Code 2200, William F. Moler
ATTN: Code 2200, Richard Pappert
ATTN: Tech. Lib. for T. J. Keary
ATTN: Code 2200, Herbert Hughes

Superintendent (Code 1424)
Naval Postgraduate School
ATTN: Code 2124, Tech. Reports Librarian

DEPARTMENT OF THE NAVY (Continued)

Director
Naval Research Laboratory
ATTN: Douglas P. McNutt
ATTN: Code 7701, Jack D. Brown
ATTN: Code 7709, Wahab Ali
ATTN: Code 7750, Darrell F. Strobel
ATTN: Code 7700, Timothy P. Coffey
ATTN: Code 7750, Paul Juluenne
ATTN: Code 2600, Tech. Lib.
ATTN: Code 7127, Charles Y. Johnson
ATTN: Code 7120, W. Neil Johnson
ATTN: Code 7750, J. Davis
ATTN: Code 7750, Klaus Hein
ATTN: Code 7750, Joel Feddler
ATTN: Code 2027, Tech. Lib.
ATTN: Code 7750, S. L. Ossakow
ATTN: Code 7730, Edgar S. McClean

Officer-in-Charge
Naval Surface Weapons Center
ATTN: Code WA501, Navy Nuc. Prgms. Off.
ATTN: Code WX21, Tech. Lib.
ATTN: D. J. Sand
ATTN: L. Rudlin

Commanding Officer
Naval Intelligence Support Center
ATTN: Doc. Con.
ATTN: Code 40A, E. Blase

Commander
Naval Weather Service Command
ATTN: Mr. Martin

DEPARTMENT OF THE AIR FORCE

AF Geophysics Laboratory, AFSC
5 cy ATTN: OPR, Alva T. Stair
5 cy ATTN: LKB, Kenneth S. W. Champion
2 cy ATTN: OPR-1, R. Murphy
2 cy ATTN: OPR-1, J. Kennealy
5 cy ATTN: OPR, J. Ullwick

AF Weapons Laboratory, AFSC
ATTN: CA
ATTN: Col G. J. Freyer
2 cy ATTN: DYM
5 cy ATTN: DYC
5 cy ATTN: SUL
5 cy ATTN: DYT

Commander
ASD
ATTN: ASD-YH-EX, Lt Col Robert Leverette

SAMSO/SZ
ATTN: SZJ, Maj Lawrence Doan

AFTAC
5 cy ATTN: TD
2 cy ATTN: Tech. Lib.

Hq. USAF
ATTN: DLS
ATTN: DLCAW
ATTN: DTL
ATTN: DLXP
ATTN: SDR
ATTN: Tech. Lib.

DEPARTMENT OF THE AIR FORCE (Continued)

SAMSO/AW
ATTN: AW

DEPARTMENT OF ENERGY

Division of Military Application
ATTN: Doc. Con. for Major D. A. Haycock
ATTN: Doc. Con. for Colonel T. Gross
ATTN: Doc. Con. for David Slade
ATTN: Doc. Con. for Donald I. Gale
ATTN: Doc. Con. for F. S. Ross

Los Alamos Scientific Laboratory
ATTN: Doc. Con. for R. A. Jeffries
ATTN: Doc. Con. for C. R. Mehl
ATTN: Doc. Con. for G. Rood
ATTN: Doc. Con. for H. V. Sego
ATTN: Doc. Con. for D. Steinhaus
ATTN: Doc. Con. for J. Judd
ATTN: Doc. Con. for T. Bieniewski
ATTN: Doc. Con. for D. M. Rohrer
ATTN: Doc. Con. for Martin Tierney
ATTN: Doc. Con. for Marge Johnson
ATTN: Doc. Con. for John S. Malik
ATTN: Doc. Con. for William Maier
ATTN: Doc. Con. for S. Rockwood
ATTN: Doc. Con. for Donald Kerr
ATTN: Doc. Con. for W. D. Barfield
ATTN: Doc. Con. for Reference Library
ATTN: Doc. Con. for W. M. Hughes
ATTN: Doc. Con. for E. W. Jones, Jr.
ATTN: Doc. Con. for John Zinn
ATTN: Doc. Con. for E. S. Bryant

University of California
Lawrence Livermore Laboratory
ATTN: G. R. Haugen
ATTN: A. Kaufman
ATTN: D. J. Wuebbles
ATTN: J. F. Tinney
ATTN: Julius Chang
ATTN: Tech. Info. Dept.
ATTN: W. H. Duewer

Sandia Laboratories
ATTN: Doc. Con. for W. D. Brown
ATTN: Doc. Con. for Org. 9220
ATTN: Doc. Con. for Craig Hudson
ATTN: Doc. Con. for J. C. Eckardt
ATTN: Doc. Con. for C. W. Gwyn
ATTN: Doc. Con. for D. A. Dahlgren
ATTN: Doc. Con. for M. L. Kramm
ATTN: Doc. Con. for T. Wright
ATTN: Doc. Con. for Charles Williams
ATTN: Doc. Con. for Sandia Rpt. Coll.
ATTN: Doc. Con. for Doc. Con. Div.

Sandia Laboratories
Livermore Laboratory
ATTN: Doc. Con. for Thomas Cook

Department of Energy
Div. of Hqs. Services, Library Branch, G-043
ATTN: Doc. Con. for D. Kohlstad
ATTN: Doc. Con. for J. D. LaFleur
ATTN: Doc. Con. for Class. Tech. Lib.
ATTN: Doc. Con. for George Regosa
ATTN: Doc. Con. for Rpts. Section
ATTN: Doc. Con. for R. Kandel
ATTN: Doc. Con. for H. H. Kurzweg

DEPARTMENT OF ENERGY (Continued)

Argonne National Laboratory
Records Control
ATTN: Doc. Con. for A. C. Wall
ATTN: Doc. Con. for S. Gabelnick
ATTN: Doc. Con. for J. Berkowitz
ATTN: Doc. Con. for Lib. Svsc. Rpts. Sec.
ATTN: Doc. Con. for Len Liebowitz
ATTN: Doc. Con. for David W. Green
ATTN: Doc. Con for Gerald T. Reedy

OTHER GOVERNMENT AGENCY

Department of Commerce
Office of Telecommunications
Institute for Telecom Science
ATTN: William F. Utlaut

DEPARTMENT OF DEFENSE CONTRACTORS

Aero-Chem Research Laboratories, Inc.
3 cy ATTN: A. Fontijn

Aerodyne Research, Inc.
ATTN: M. Camac
ATTN: F. Bien

Aerospace Corporation
ATTN: Harris Mayer
ATTN: Thomas D. Taylor
ATTN: R. D. Rawcliffe
ATTN: R. Grove
ATTN: R. J. McNeal

University of Denver
Colorado Seminary
Denver Research Institute
ATTN: Sec. Officer for Mr. Van Zyl
ATTN: Sec. Officer for David Murcray

General Electric Company
TEMPO-Center for Advanced Studies
ATTN: Warren S. Knapp
5 cy ATTN: DASIAC, Art Feryok

General Research Corporation
ATTN: John Ise, Jr.

Geophysical Institute
University of Alaska
ATTN: T. N. Davis
3 cy ATTN: Neal Brown

Honeywell Incorporated
Radiation Center
ATTN: W. Williamson

HSS Incorporated
ATTN: A. H. Tuttle

Institute for Defense Analyses
ATTN: Hans Wolfhard
ATTN: Ernest Bauer

DEPARTMENT OF DEFENSE CONTRACTORS (Continued)

Lockheed Missiles and Space Co. Inc.
ATTN: Billy M. McCormac, Dept. 52-54
ATTN: John B. Cladis, Dept. 52-12
ATTN: J. B. Reagan, Dept. 52-12
ATTN: John Kumer
ATTN: Martin Walt, Dept. 52-10
ATTN: Richard G. Johnson, Dept. 52-12
ATTN: Robert D. Sears, Dept. 52-14
ATTN: Tom James

Mission Research Corporation
ATTN: P. Fischer
ATTN: D. Archer

Photometrics, Inc.
3 cy ATTN: I. L. Kofsky/D. P. Villanucci/G. Davidson

Physical Dynamics, Inc.
ATTN: Joseph B. Workman

Physical Sciences, Inc.
ATTN: Kurt Wray

R & D Associates
ATTN: Robert E. Lelevier
ATTN: Forrest Gilmore

R & D Associates
ATTN: Herbert J. Mitchell

Science Applications, Inc.
ATTN: Daniel A. Hamlin

Space Data Corporation
ATTN: Edward F. Allen

SRI International
ATTN: M. Baron
ATTN: Ray L. Leadabrand
ATTN: Walter G. Chesnut

SRI International
ATTN: Warren W. Berning

Technology International Corporation
ATTN: W. P. Boquist

Utah State University
ATTN: D. Burt
ATTN: Kay Baker
ATTN: C. Wyatt
ATTN: Doran Baker

Visidyne, Inc.
ATTN: L. Katz
ATTN: William Reidy
ATTN: Henry J. Smith
ATTN: Charles Humphrey
ATTN: J. W. Carpenter
ATTN: T. C. Degges